SEARCH FOR $S = +1$ EXOTIC BARYON IN $\gamma p \to K^+K^-\pi^+(n)$

By

Lei Guo

Dissertation

Submitted to the Faculty of the

Graduate School of Vanderbilt University

in partial fulfillment of the requirements

for the degree of

DOCTOR OF PHILOSOPHY

in

Physics

May, 2004

Nashville, Tennessee

Approved by

Prof. David J. Ernst

Dr. Dennis P. Weygand

Prof. Senta V. Greene

Prof. Thomas W. Kephart

Prof. Paul D. Sheldon

Prof. Sait A. Umar

Prof. Medford S. Webster

ACKNOWLEDGMENTS

I would like to thank everybody who has made it possible for me to complete this work, and supported me throughout my graduate school era. In particular, I would like to thank Dr. Dennis Weygand, who was willing to give me an opportunity and guided me to become an experimental physicist. His vision, support, and kindness has changed me profoundly in both professional and personal ways. I would also like to express my gratitude to Dr. David Ernst, my advisor, for supporting me both emotionally and academically. Without his help, it would not have been possible to stay the course of getting a physics Ph.D. I also like to thank John Cummings and Paul Eugenio, as well as Dennis, for making the partial wave analysis a possible task.

Special thanks go to my colleagues Ji Li and Mina Nozar, who shared the pain and happiness with me performing the detector calibration and data processing. Great gratitude is due to Dr. Gary Adams and Dr. Carlos Salgado for their support and advice.

I also like to thank all the members of the CLAS collaboration and the staff of the TJNAF accelerator facility. Without them, this work would not have been possible. The support and advice that I received from all my committee members are also invaluable and greatly appreciated.

Special thanks for my parents and my sister for their understanding during the last seven years I have been in the United states.

TABLE OF CONTENTS

Page

LIST OF FIGURES

LIST OF TABLES

CHAPTER I

INTRODUCTION

Physics motivation

A brief history of particle physics

Humankind has never stopped wondering what the world we live in is made of. More than 2400 years ago, the Greek philosopher Leucippus surmised the idea of the atom, an indivisible unit of matter. Later, his student Democritus expanded the concept of atoms. He maintained the impossibility of dividing things ad infinitum and proposed that atoms are the basis of all forms of matter. However, it was not until the early nineteenth century that empirical physicists making observations began to define the elementary particles which form our universe. In 1811, Amadeo Avogadro hypothesized that equal volumes of gases at the same temperature and pressure contain equal numbers of molecules. He reasoned that simple gases were composed of compound molecules of two or more atoms. Nearly a century later, J.J. Thompson discovered the electron in 1897. Soon after, Ernest Rutherford made the discovery of compact nuclei. Thus the modern science of particle physics began a new era. With the introduction of quantum mechanics and the construction of highly sophisticated high energy experimental facilities, physicists have been able to penetrate the subatomic world and describe it in the language of quarks. In the 1950's and 1960's,

with the discovery of a series of new elementary particles, the quark model (Gell-Man, Zweig, 1963) emerged to explain this new family of particles; hadrons, particles which interact through strong interactions within the quark model, are categorized into two groups: mesons and baryons. Mesons are composed of quark and antiquark pairs, while baryon states are made of three quarks. Remarkably, almost all known hadrons are well described by this model.

In 1964, physicists at the Brookhaven National Laboratory discovered the Ω^-, with strangeness$= -3$ [1], in the 80 inch hydrogen bubble chamber in the reaction of $K^- p \rightarrow \Omega^- K^+ K^0$ [1, 2, 3]. This particle matched precisely to the prediction by Gell-Mann of an isotopic singlet baryon with $J^P = \frac{3}{2}^+, S = -3$, and negative charge around 1680 MeV/c^2, using $SU(3)$ symmetry in 1962 [4]. This discovery was hailed as one of the defining points of hadronic structure. Fig. 1, the bubble chamber photograph of the first observation of the Ω^-, has become one of the most famous bubble chamber pictures of all. The quark model, although only a phenomenological model, became the pervading picture of our understanding of the subatomic world.

The constituent quark model and QCD

In 1964, the constituent quark model was proposed by Gell-Mann and Zweig to explain the spectrum of strongly interacting particles in terms of elementary constituents called quarks [5, 9, 10]. In this model, mesons are bound states of a quark and an antiquark, and baryons are bound states of three quarks. Mesons and baryons together form the family of hadrons, i.e., particles that interact through the strong

[1] The quantum number of strangeness was introduced earlier in 1950's [6, 7, 8], see the next section

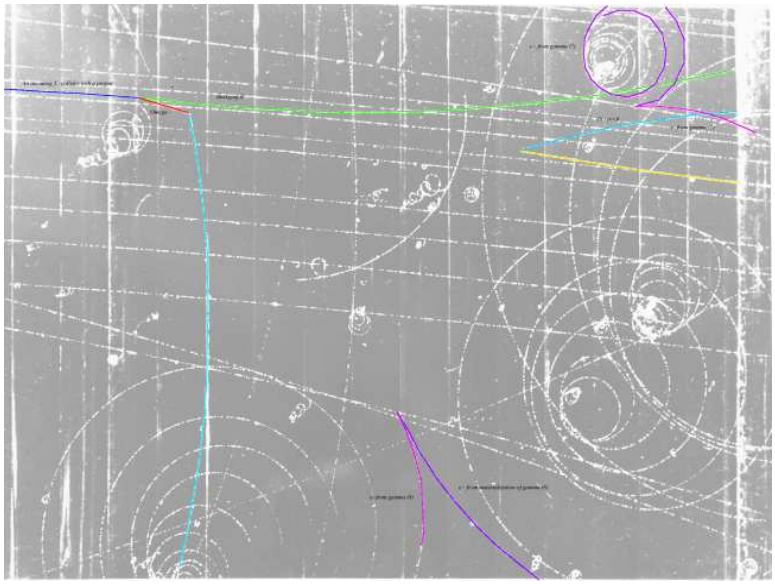

Figure 1: In the BNL 80 inch hydrogen bubble chamber, a 5.0 GeV/c K^- beam interacts with a proton: $K^-p \to \Omega^- K^+ K^0$. The red line shows the flight of Ω^-, which then decays to π^- (blue) and $\Xi^0 \to \Lambda\pi^0$, with $\Lambda \to p\ (yellow)\pi^-\ (blue)$.

force. The quantum numbers of hadrons can be obtained from their quark content, which are summarized in Table I. The most common baryons: protons (uud) and neutrons (udd), are isospin partners. The SU(2) isospin symmetry itself is believed to be a result of the closeness of the u quark and the d quark in mass. Baryon conservation, an apparent conservation law , implies that it is impossible to destroy or to create a single quark. However, we can annihilate or create quark-antiquark pairs. The discovery of strange particles and the introduction of strangeness [6, 7, 8] lead to the extension to $SU(3)$ from isospin $SU(2)$ symmetry, however, flavor $SU(3)$ symmetry is not exact, since the strange quark is much heavier than the u quark and d quark. In addition, quarks retain their identity under strong or electromagnetic transitions, while weak interactions do not prohibit transmutations such as $s \to u + d\bar{u}$. The types of the quarks are traditionally referred to as $flavors$.

The light $q\bar{q}$ meson states are classified according to the $SU(3) \otimes SU(3)$ group,

Table 1: Quantum of the six flavor of quarks, here S is the strangeness

Quark	Mass (GeV/c^2)	Spin	B	Q	I_3	S	Charm	Bottom	Top
u	0.005	$\frac{1}{2}$	$\frac{1}{3}$	$\frac{2}{3}$	$\frac{1}{2}$	0	0	0	0
d	0.01	$\frac{1}{2}$	$\frac{1}{3}$	$-\frac{1}{3}$	$-\frac{1}{2}$	0	0	0	0
c	1.5	$\frac{1}{2}$	$\frac{1}{3}$	$\frac{2}{3}$	0	0	1	0	0
s	0.2	$\frac{1}{2}$	$\frac{1}{3}$	$-\frac{1}{3}$	0	-1	0	0	0
t	180	$\frac{1}{2}$	$\frac{1}{3}$	$\frac{2}{3}$	0	0	0	0	1
b	4.7	$\frac{1}{2}$	$\frac{1}{3}$	$-\frac{1}{3}$	0	0	0	-1	0

which translates into $3 \otimes \bar{3} = 8 \oplus 1$. The nonet is decomposed into an octet and a singlet (Fig. 2). For the baryons, which are three quark states, there are 27 possible combinations: the flavor $SU(3)$ decomposition is $3 \otimes 3 \otimes 3 = (6 \otimes 3) \oplus (\bar{3} \otimes 3) = 10 \oplus 8 \oplus 8 \oplus 1$. For the baryon ground states, we need to combine the flavor $SU(3)$ decomposition with the $SU(2)$ spin decomposition. The ground states are illustrated in Fig. 3.

Although the original quark model enjoyed phenomenological success, it faced two serious problems. One is the lack of free particles with fractional charge. The other is the apparent violation of Fermi-Dirac statistics in terms of the quantum numbers of the Δ^{++}, which was first discovered in 1952 by Fermi and collaborators in $\pi^+ p$ scattering experiment [11]. The Δ^{++} has spin 3/2 and charge +2, and is interpreted as a uuu bound state with zero orbital angular momentum and all three quark spins parallel, which violates the Pauli exclusion principles.

In order to reconcile this dilemma, Han and Nambu [12], Greenberg [13], and Gell-Mann proposed that quarks carry an additional, unobserved quantum number,

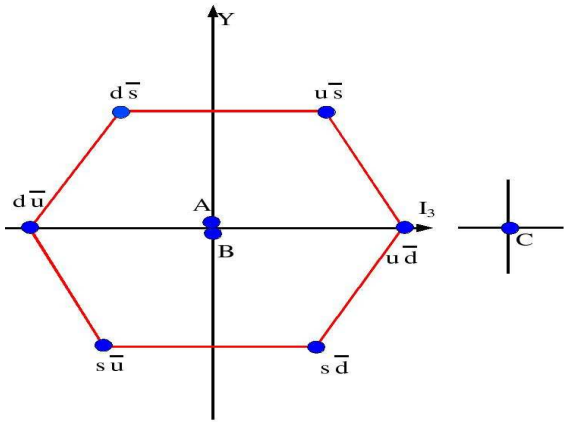

Figure 2: The meson nonet decomposition into an octet and a singlet. $A = \sqrt{\frac{1}{2}(u\bar{u} - d\bar{d})}$ is part of the isospin triplet $(d\bar{u}, A, -u\bar{d}$, $B = \sqrt{\frac{1}{6}(u\bar{u} + d\bar{d} - 2s\bar{s})}$ is an isospin singlet part of the octet. C $= \sqrt{\frac{1}{3}(u\bar{u} + d\bar{d} + s\bar{s})}$ is an $SU(3)$ singlet as well as an isospin singlet.

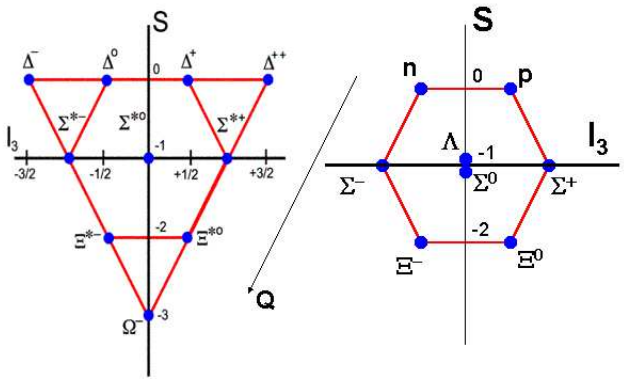

Figure 3: The conventional (qqq) baryon ground states in the quark model. Left: the baryon decuplet for $J = \frac{3}{2}$ baryons, where the Ω^- sits at the bottom corner. Right: the baryon octet for $J = \frac{1}{2}$ baryons.

called *color*. A new internal $SU(3)$ global symmetry was hence introduced. Assuming that physical hadrons are singlets under color also implies that the only possible light hadrons are the mesons, baryons, and antibaryons. This seemingly superfluous property of color puzzled physicists until color symmetry was identified with a gauge group, with the colors being the gauge quantum numbers of the quarks. This resulted in a model of the strong interactions as a system of quarks, of various flavors, each assigned to the fundamental representation of the local gauge group $SU(3)$. The quanta of the $SU(3)$ gauge field are called gluons, and the theory is known as Quantum Chromodynamics, or QCD. QCD is the physical theory describing one of the fundamental forces, the strong interaction. The final form of the theory was proposed in the early 1970s by Frank Wilczek and David Gross [14]. It uses quantum field theory to describe the interaction of quarks and gluons.

Later, even heavier quarks were discovered. In 1974, the J/ψ particle was discovered and interpreted as a $c\bar{c}$ meson state [15, 16], which signaled the existence of a new quark: the charmed quark. The bottom quark (b) was discovered in 1977 [17], with a mass of 4.7 GeV/c^2. The top quark (t) was discovered in 1995, and has an even much heavier mass of 176 GeV^2 [18, 19]. The topic of this thesis is the spectroscopy of hadrons composed of light quarks (u, d, s).

Exotic hadrons

QCD does not prohibit the existence of hadrons that lie outside of the naive quark model. While predictions of the decay rates and cross-sections based on isospin symmetry are close to experimental results in general, the quark model does not

address quark confinement within the hadrons. This should not be surprising, since confinement should arise from the existence of gluons within the hadron states. The gluons themselves are in fact expected to contribute to the properties of the hadronic particles, and provide extra degrees of freedom. Various proposed models predict possible exotic mesons and baryons that involve more complex internal structures. Those states that have quantum numbers which cannot exist within the naive quark model are called exotic states. Possible exotic mesons may be classified as glueballs (gg), hybrids ($q\bar{q}g$), four-quarks states ($q\bar{q}q\bar{q}$), and exotic baryon ($qqqq\bar{q}$) states. It is also important to note that recent measurement of nucleon structure functions from high energy lepton-nucleon experiments has demonstrated that the quark cloud ($q\bar{q}$ pairs) contributes significantly to the total momentum and spin of the nucleon. In other words, the usual baryons can be seen as a mixture of the standard (qqq) configuration, as well as ($qqqq\bar{q}$), ($qqqg$), ... Therefore, the search for exotic particles beyond the normal quark model is of fundamental importance to the understanding of quark confinement and the nature of the strong force.

Exotic and hybrid mesons

The naive quark model states that a meson is composed of a quark and an anti-quark pair, and only this pair of quarks contributes to the properties of the meson. However, the gluons, which are bonding these two quarks, can also interact with each other to form a bound state, or interact along with the quarks as a fundamental constituent of matter. Among the quantum numbers that define meson states are J^{PC}, where J is the total spin, P is the parity and C is the charge conjugation.

There are certain J^{PC} combinations that are not accessible as the conventional $q\bar{q}$ meson bound states; these mesons are called exotic mesons. To demonstrate the possible nature of exotic hybrid mesons, let us first go over how mesons are classified. Meson states are denoted by their principle quantum number: $I^G J^{PC}$, where J is the total spin, P is the parity of the state, C is the charge conjugation eigenvalue, I is the isospin, and G is the G-parity. For a conventional meson that is a bound state of a $q\bar{q}$ pair, we have the following rules:

$$P(q\bar{q}) = (-)^{L+1} \tag{1}$$

$$C(q\bar{q}) = (-)^{L+S} \tag{2}$$

$$G = C(-)^I = (-)^{L+S+I} \tag{3}$$

$$\vec{J} = \vec{L} + \vec{S} \tag{4}$$

Note that for a $q\bar{q}$ pair, S can only be 0 (antisymmetric singlet) and 1 (triplet), the only allowed J^{PC} combinations are:

$$0^{-+}, 0^{++}, 1^{--}, 1^{+-}, 1^{++}, 2^{--}, 2^{-+}, 2^{++}, 3^{--}, 3^{+-}, 3^{++}... \tag{5}$$

With the contribution from the gluons that are interacting with the quarks, as described by the flux-tube model [29], states can have exotic quantum numbers other than what are listed in Eq. 5:

$$0^{--}, 0^{+-}, 1^{-+}, 2^{+-}, 3^{-+}, ... \tag{6}$$

These meson states are therefore called exotic mesons. Several QCD-motivated phenomenological models have been proposed to incorporate explicitly the gluonic

degree of freedom into the meson $q\bar{q}g$ interaction picture [20, 21, 22, 23, 24, 25, 26, 27]. The most commonly adopted model is the gluonic flux-tube model [29].

The flux-tube model was inspired by Yoichiro Nambu's conjecture that the empirical fact that the spin of mesons was proportional to the square of their masses could rise from a relativistic string with constant mass per unit length binding the $q\bar{q}$ together. In this picture, the $q\bar{q}$ pair in a meson are bound by a gluonic color field that forms a tube due to the self interacting nature of the gluons. Quark confinement is a direct result of the infinite energy required to break the tube and separate the quark and antiquark. In this model, conventional mesons are states with the flux tube in its ground state. The excitation of the flux tube leads to the hybrid mesons. The added degree of freedom corresponding to the rotation of the tube along the $q\bar{q}$ axis is parameterized by the quantum number Λ, which can contribute to exotic J^{PC} combinations. More recently, lattice calculations have confirmed the behavior of the flux tube between the $q\bar{q}$ pair. In Fig. 4, the left plot shows the linear inter-quark potential at distance greater than 0.2 fm [28], while the right plot shows the formation of a flux tube between a quark and an antiquark assuming the distance between them is 1.2 fm [32]. Both the flux-tube model [31] and the lattice calculations [32] have predicted the lowest exotic meson mass to be around 1.9 GeV/c^2.

Existing evidence for exotic mesons

Several experiments in 1990's have reported possible evidence for exotic mesons. A 1^{-+} $\pi_1(1400)$ state (Fig. 5), with a mass of $1370 \pm 16^{+50}_{-30}$ MeV/c^2, was observed decaying to $\eta\pi^-$ at BNL [33]. Their finding is consistent with the finding made earlier

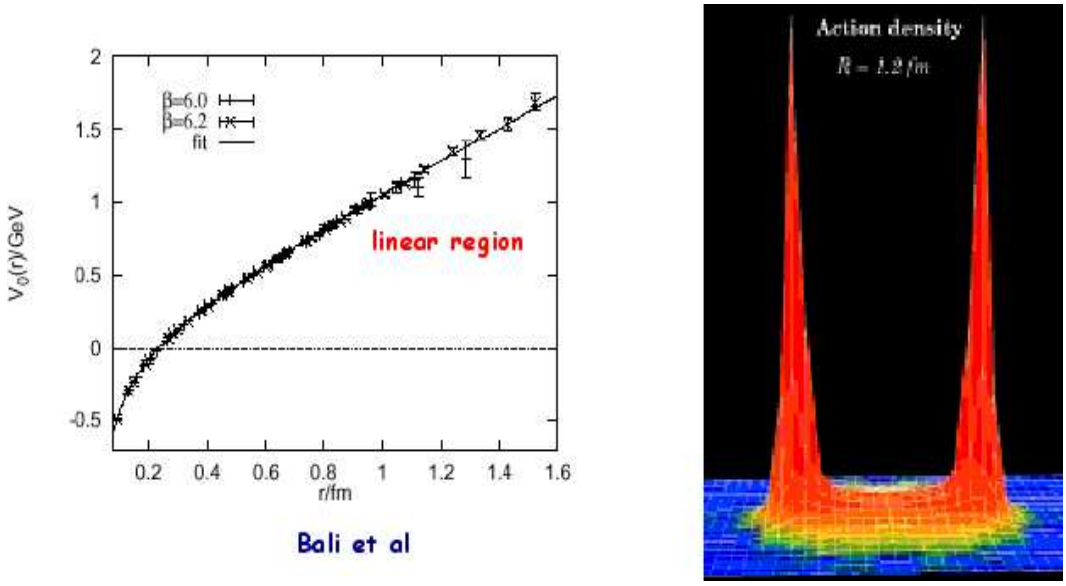

Figure 4: Left: Inter-quark potential in the quenched approximation [28]; Right:energy density in the space surrounding a $q\bar{q}$ pair [32]

by the VES Collaboration at IHEP ($\pi^- N$ interactions at 37 GeV/c). The VES group claimed a 1^{-+} exotic meson signal in the $\eta\pi^-$ state at 1316 ± 12 MeV/c^2 [34] with a width of 287 ± 25MeV/c^2, but did not attempt to identify it as a resonance. The Crystal Barrel Collaboration at CERN confirmed the $\pi(1400)$ 1^{-+} exotic $\eta\pi$ meson state with a mass of $1400 \pm 20 \pm 20$ MeV/c^2 and a width of $310 \pm 50^{+50}_{-30}$ MeV/c^2 in the $\bar{p}d$ annihilation into $\pi^-\pi^0\eta p_{spectator}$ [35]. Soon after the first exotic meson state was reported at BNL, another possible 1^{-+} state with a mass of $1593 \pm 8^{+29}_{-47}$ MeV/c^2 and a width of $168 \pm 20^{+150}_{-10}$ MeV/c^2 was observed (Fig. 6) in the reaction of $\pi^- p \to \pi^+\pi^-\pi^- p$ by the same group [36]. However, its decay to $\rho\pi$ was unexpected for a gluonic hybrid. It was followed by another observation, from the same group, of a 1^{-+} state in the $\eta'\pi$ channel with a mass of $1597 \pm 10^{+45}_{-10}$ MeV/c^2 but wider ($340 \pm 40 \pm 50$ MeV/c^2) [37]. The higher lying 1^{-+} exotic state was later confirmed by VES in a combined fit to intensities in the $\rho\pi, \eta'\pi$ and $\omega\pi\pi$ systems which resulted in a Breit-Wigner shape

with mass 1600 MeV/c^2 and width 300 MeV/c^2 [38]. In these experiments, the Partial Wave Analysis (PWA, see chapter 5) technique was used to extract the J^{PC} quantum number of the meson system.

Yet the fact that these states lie below the predicted lowest mass of 1^{-+} exotic mesons by the gluonic flux-tube model and the lattice calculations raises questions about the true nature of these meson states, although the MIT bag model does propose an exotic meson state around 1400 MeV. On the other hand, Lipkin pointed out [39] that isospin symmetry forbids the $\eta\pi$ decay of an odd parity hybrid state via an OZI-allowed diagram, while there is no selection rule that forbids the $\eta\pi$ decay of a four-quark state. That prompted some to propose that these exotic mesons may not be the expected gluonic hybrids, but indeed $q\bar{q}q\bar{q}$ states. In summary, even though the existence of these exotic meson states appears quite unambiguous, their nature remains unclear.

Exotic baryons

Although exotic mesons can be identified by searching for mesons with exotic J^{PC} quantum numbers, there is no equivalent counterpart in the case of baryons. Baryons have no C-parity, and all half-integral J with both parities can be achieved with three quarks. However, there could be exotic baryons with quantum numbers such as positive strangeness, which can not be obtained from three quarks. While the exact nature of those recently discovered exotic mesons remain somewhat ambiguous, these exotic baryons are manifestly exotic. Such exotic baryons as an $S = +1$ baryon state have been proposed in the context of the bag model [40]. The importance

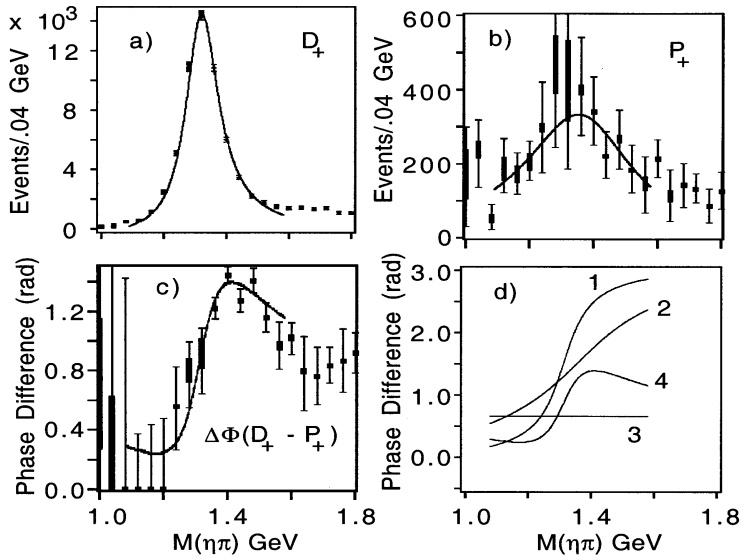

Figure 5: a)The D_+ wave intensity distribution binned in the invariant mass of $\eta\pi^-$, consistent with $a_2(1320)$ production, in the reaction of $\pi^-(18GeV/c)p \to \eta\pi^- p$. b)The 1^{-+} exotic P_+ wave intensity distribution. c) The phase difference between the D_- and P_+ waves. d)The lines correspond to (1) the fitted D_+ Breit-Wigner phase, (2) the fitted P_+ Breit-Wigner phase, (3)the fitted $D_+ - P_+$ relative production phase, and (4) the overall $D_+ - P_+$ phase difference as shown in (c), but with a different scale.

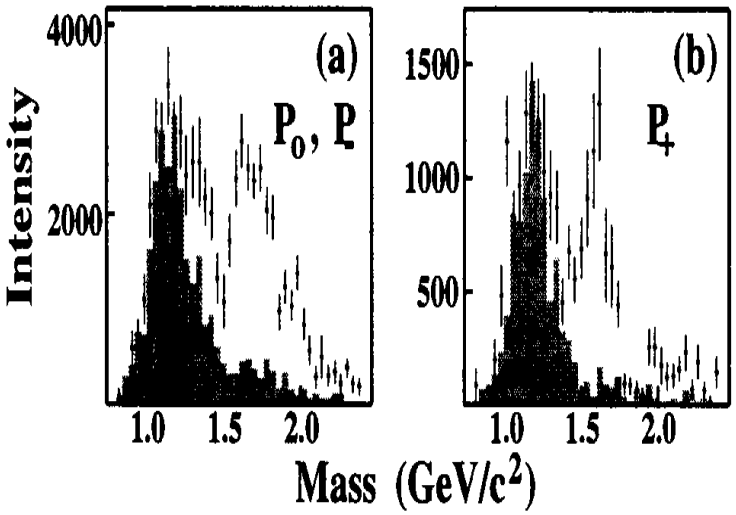

Figure 6: The 1^{-+} exotic wave intensity distribution binned in the invariant mass of $\pi^+\pi^-\pi^-$ in the reaction of $\pi^-(18GeV/c)p \to \pi^+\pi^-\pi^- p$. a) all $M^\epsilon = 0^-$ and 1^- waves combined; b) the $M^\epsilon = 0^-$ wave. The shaded histograms show estimated contributions from all non-exotic waves due to leakage.

of the experimental evidence is obvious. In the past, the search for exotic baryons focused on pentaquark states which have a minimal ($qqqq\bar{q}$) structure, where the $\bar{q}$ has a different flavor than the other quarks. Those experiments mainly involved K^+-nucleon scattering and a phase shift analysis. During those experiments, widths of the order of 100MeV were expected and the mass ranged from 1.55 to 2.65 GeV. No convincing evidence was ever found for possible exotic pentaquark states. In fact, the whole section on pentaquarks was removed from the Particle Data Group after 1986.

Chiral Soliton Model

In 1987, Praszalowicz predicted a possible $Y = 2$ isosinglet member of the $J = \frac{1}{2}$ $1\bar{0}_f$ around 1540 MeV/c^2 [41]. However, the search for pentaquarks was revitalized in 1990's when interest was triggered by a theoretical prediction by Diakonov et al. [42] of the possible existence of a narrow $S = +1$ baryon state as a member of a baryon anti-decuplet.

The chiral soliton model, proposed by Skyrme [43, 44] in the 1960's, was a different approach to understand the nucleon. He suggested that the low-energy behavior of nucleons can be viewed as a spherically symmetric soliton solution of the pion field. The minimal generalization of spherical symmetry to incorporate three isospin components of the pion field is the so-called hedgehog form,

$$\pi^a(\vec{x}) = \frac{x^a}{r} P(4) \tag{7}$$

where $P(r)$ is the spherically-symmetric profile of the soliton. This implies that a spatial rotation of the field is equivalent to that in isospin and the rotational states have isospin T equal to spin J, with the excitation energies being

$$E_{rot} = \frac{J(J+1)}{2I} \tag{8}$$

where I is the soliton moment of inertia. The rotational states are therefore $(2J+1)^2$-fold degenerate. The four nucleon states have $J = 1/2$ and the sixteen Δ-isobar states have $J = 3/2$. In this view, the baryonic nature of the nucleon is not due to quarks carrying baryon quantum number $B = 1/3$. Instead, the baryon number is interpreted as topological quantum number of the pion field [45, 46]. QCD has shed some light into why this picture may be correct: the spontaneous chiral symmetry breaking in QCD determines to a great extent the strong interaction dynamics, while Witten attributes the reason the pion field inside the nucleon can be considered as a classic one, *i.e.* as a "soliton", to the large N_c (number of colors) argumentation [45].

By introducing the rotation in the flavor $SU(3)$ space, the quantizations show that the lowest baryon state is the octet with spin 1/2, and the next is the decuplet with spin 3/2, which is the same as the constituent quark model predictions. The chiral soliton model relates the splittings inside the decuplet with those in the octet to an accuracy better than 1% [47]. In the three-flavor case the third rotational excitation is an anti-decuplet with spin 1/2, which was probably first pointed by the authors at the ITEP Winter School in 1984 [48]. As it is demonstrated in Fig. 7, pentaquark states come out naturally as the rotational excitations of the soliton rigid core (qqq) surrounded by meson fields ($q\bar{q}$) in the framework of the chiral soliton model.

Reference [42] also made a definite prediction for the masses and widths of a decuplet of pentaquark states (the so-called anti-decuplet, Fig. 8). By identifying the rather well established nucleon resonance $N(1710, \frac{1}{2}^+)$ as one of the members of the

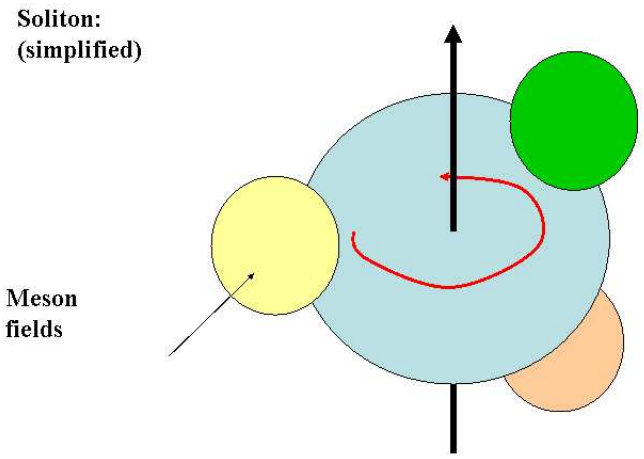

Figure 7: A simplistic picture of the chiral soliton model within which the baryon anti-decuplet is predicted. The baryons are represented by a (qqq rigid core surrounded by a ($q\bar{q}$ meson field

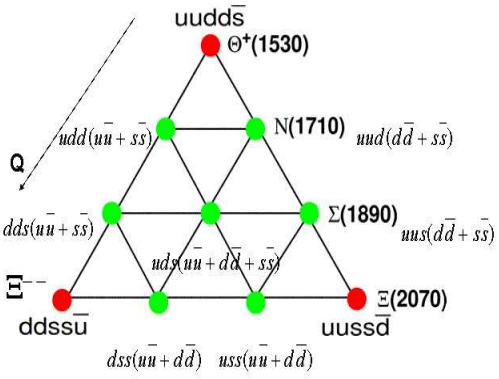

Figure 8: The baryon antidecuplet predicted by Diakonov et al. [42], using the chiral soliton model. The three corners are states that are manifestly exotic which are not accessible by conventional (qqq) baryons. The middle octet overlaps with the conventional baryons and are not exotic.

anti-decuplet, namely the one with the nucleon quantum members $N_{\bar{10}}$, the second $SU(3)$ moment of inertia I_2 can be fixed and used to determine the mass and width of the anti-decuplet members. These calculations do not rely upon a specific dynamical realization, but follow from symmetry considerations.

The most interesting aspect of this multiplet is the prediction of three states with exotic quantum numbers, i.e. quantum numbers that can not be possessed by baryons composed of only three quarks: the Θ^+ with $S = +1$, and the Ξ^{--} and Ξ^+ with $S = -2$. Such quantum numbers can only be obtained with a minimal pentaquark configuration of the type of $uudd\bar{s}$ for the Θ^+, $ddss\bar{u}$ for Ξ^{--} and $uuss\bar{d}$ for Ξ^+. Furthermore, the widths of these exotic pentaquarks were predicted by this model to be very narrow (10-15 MeV). These predictions suggest the possible observation of these exotic baryon states directly in an invariant mass spectrum, and would not need a more sophisticated but sometimes ambiguous partial wave analysis. The narrow width would also explain the lack of evidence of such exotic states from previous data, when widths of the order of 100 MeV/c^2 were expected. Of course, the choice of the anchoring member of the anti-decuplet ($N(1710, \frac{1}{2}^+)$) is open to debate, therefore the experimental evidence for the existence of manifestly exotic pentaquark states is crucial for the validity of such models.

Di-quark model

Aside from the chiral soliton model of pentaquarks, other models such as the di-quark model proposed by Jaffe and Wilczeck, have similar predictions in terms of the mass and width of the pentaquark baryon states [49]. Jaffe and Wilczeck

argue that the chiral soliton model in the three-flavor case relies heavily on chiral $SU(3) \times SU(3)$ symmetry which is badly broken in nature. Instead, they propose a picture of the $q^4\bar{q}$ system in the framework of a di-quark model, where the four quarks are bound into two spin zero, color and flavor $\bar{3}$ diquarks, which form an $SU(3)_f$ $\bar{\mathbf{6}}_f$: $[ud]^2, [ud][us]_+, [us]^2, [us][ds]_+, [ds]^2$, and $[ds][ud]_+$. When combined with the antiquark, the result is a degenerate $SU(3)_f$ $\mathbf{8}_f \oplus \bar{\mathbf{10}}_f$, whose quark content is shown in Fig. 9. The state $\Theta^+([ud]^2\bar{s})$ is identified with the $\Theta^+(1540)$ that has been observed, while the narrowness of the state is explained possibly by the relatively weak coupling of the K^+n continuum to the $[ud]^2\bar{s}$ state from which it differs in color, spin and spatial wavefunctions. The two identical $[ud]$ diquarks must have a wavefunction antisymmetric under space exchange, *i.e.* with negative space-parity. When combined with the strange antiquark to form the $\Theta^+|[ud]^2\bar{s}\rangle$, the parity is positive.

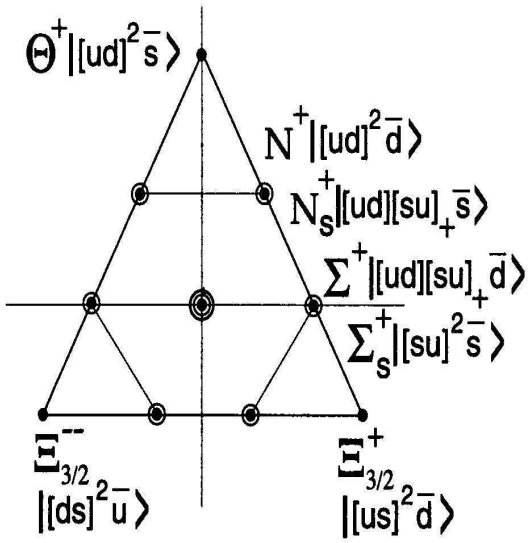

Figure 9: The quark content of representative members of the $(q^4\bar{q})\mathbf{1\bar{0}_f + 8_f}$ baryons in the di-quark model [49].

Existing evidence for pentaquark baryon states

Since the publication of the Diakonov paper in 1997, a series of new experimental searches have been conducted. A possible $S = 1$ baryon was reported in October 2002 by the LEPS Collaboration [50] in the reaction $\gamma n \to K^+K^-n$ from a ^{12}C target. A narrow baryon state of $S = +1$ was seen in the missing mass spectrum of the K^-, after removing events associated with the $\phi(1020)$ and $\Lambda(1520)$. The signal was found at 1.54 ± 0.01 GeV/c^2 with a width less than 25 MeV/c^2 and a Gaussian significance of 4.6 σ(Fig. 10). The photon energy range is 1.5 to 2.35 GeV. A Fermi momentum correction was applied due to the nature of the target. Within a year, more than a hundred papers devoted to the topic of pentaquarks were published. This possible pentaquark baryon state was originally named Z^+, and later renamed Θ^+.

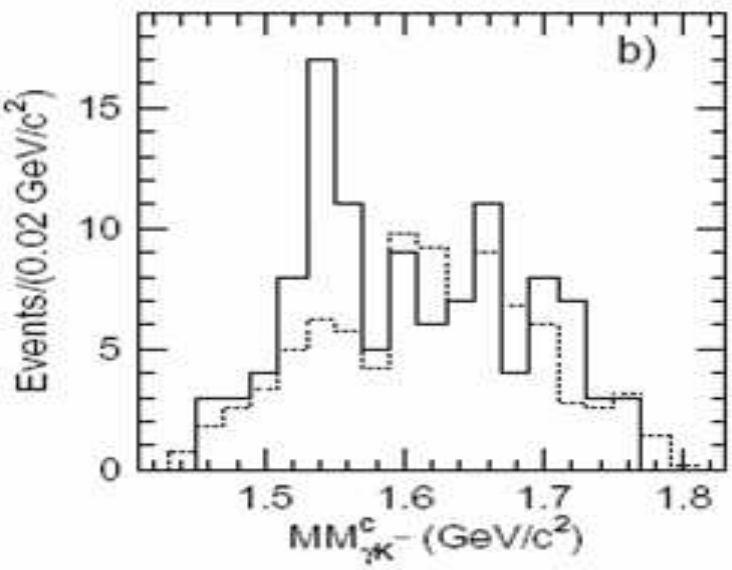

Figure 10: The $MM^c_{\gamma K^+}$ spectrum (solid histogram) in the reaction $\gamma n \to K^+K^-n$ on ^{12}C target from the LEPS collaboration. Dotted histogram is for events from the LH_2 normalized by a fit in the region above 1.59 GeV/c^2. This is the first reported evidence for a possible $S = +1$ exotic baryon consistent with the prediction of the chiral soliton model. (From reference [50].)

The result from the LEPS Collaboration was received with both enthusiasm and

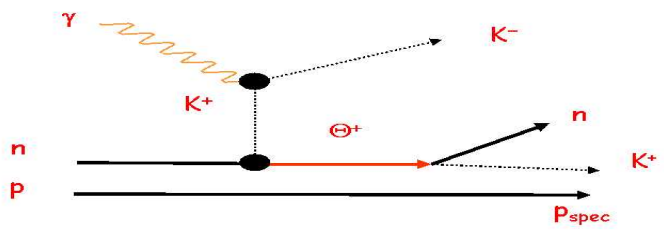

Figure 11: A possible production diagram of the Θ^+ in reaction $\gamma n \to K^+K^-n$ on ^{12}C target at the Spring-8 facility at Japan. The proton here is a spectator and is not involved in the production of Θ^+

skepticism within the hadronic physics community. Several experiments around the world have since published supportive evidence for the exotic pentaquarks. In May 2003, soon after the Japanese results, the CLAS Collaboration reported the observation of a $S = +1$ baryon state in photo-production on a deuteron target in the reaction of $\gamma d \to K^+K^-np$ [51]. The charged particles were detected while the neutron was identified using the missing mass technique. A peak in the nK^+ invariant mass spectrum was observed at 1542 ± 5 MeV, with a width smaller than 21 MeV, and a statistical significance of $5.2 \pm 0.6\ \sigma$. A possible production mechanism as suggested in the paper is shown in Fig. 13. The CLAS Collaboration also reported a possible observation of a Θ^+ that decays to nK^+ in photo-production on proton target [52]. The SAPHIR Collaboration reported a possible Θ^+ signal in the reaction $\gamma p \to nK^+K^0_s$ [53].

Based on isospin symmetry, Θ^+ should have equal branching into pK^0 and nK^+. The DIANA Collaboration at ITEP re-analyzed old K-Xenon bubble chamber data, and reported the first evidence of the Θ^+ decaying to pK^0 [54], as opposed to nK^+

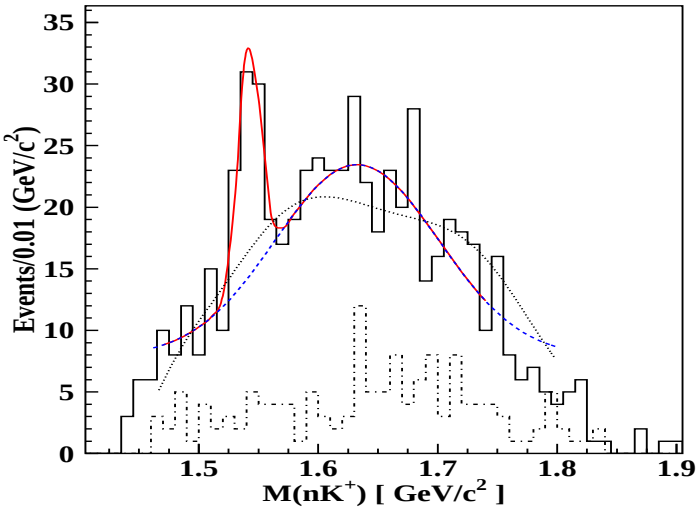

Figure 12: The nK^+ invariant mass in the reaction $\gamma n \to K^+K^-n$ on deuteron target from the CLAS collaboration [51]. The dotted curve is the shape of the simulated background. The dash-dotted histogram shows the spectrum of events associated with $\Lambda(1520)$ production. The fit (solid line) to the peak on top of the smooth background (dashed line) yields a statistical significance of 5.8 σ.

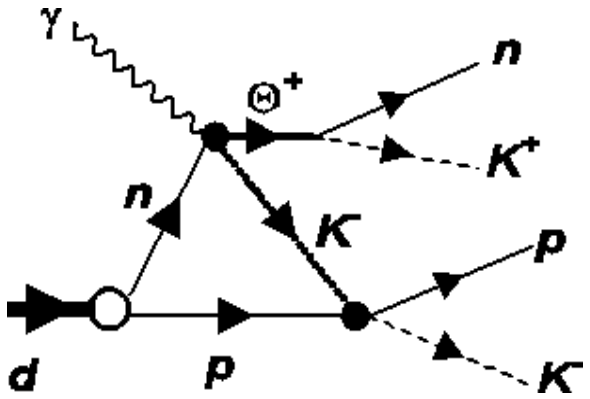

Figure 13: A possible production diagram of the Θ^+ in reaction $\gamma n \to K^+K^-n$ on target of the CLAS results. The proton here is a spectator and is not involved in the production of Θ^+. However, the diagram suggests re-scattering of K^+ off the proton which enables the proton to be detected and identify the neutron through missing mass.

seen in the first two Θ^+ signals from the LEPS and CLAS collaboration. The narrow peak has a width less than 10 MeV at 1.54 GeV with a statistical significance of 4σ (Fig. 14). Several other experiments also claimed possible observation of the Θ^+ in this channel [55, 56, 57, 58]. The mass of these states are in a range of 1525-1555 MeV/c^2.

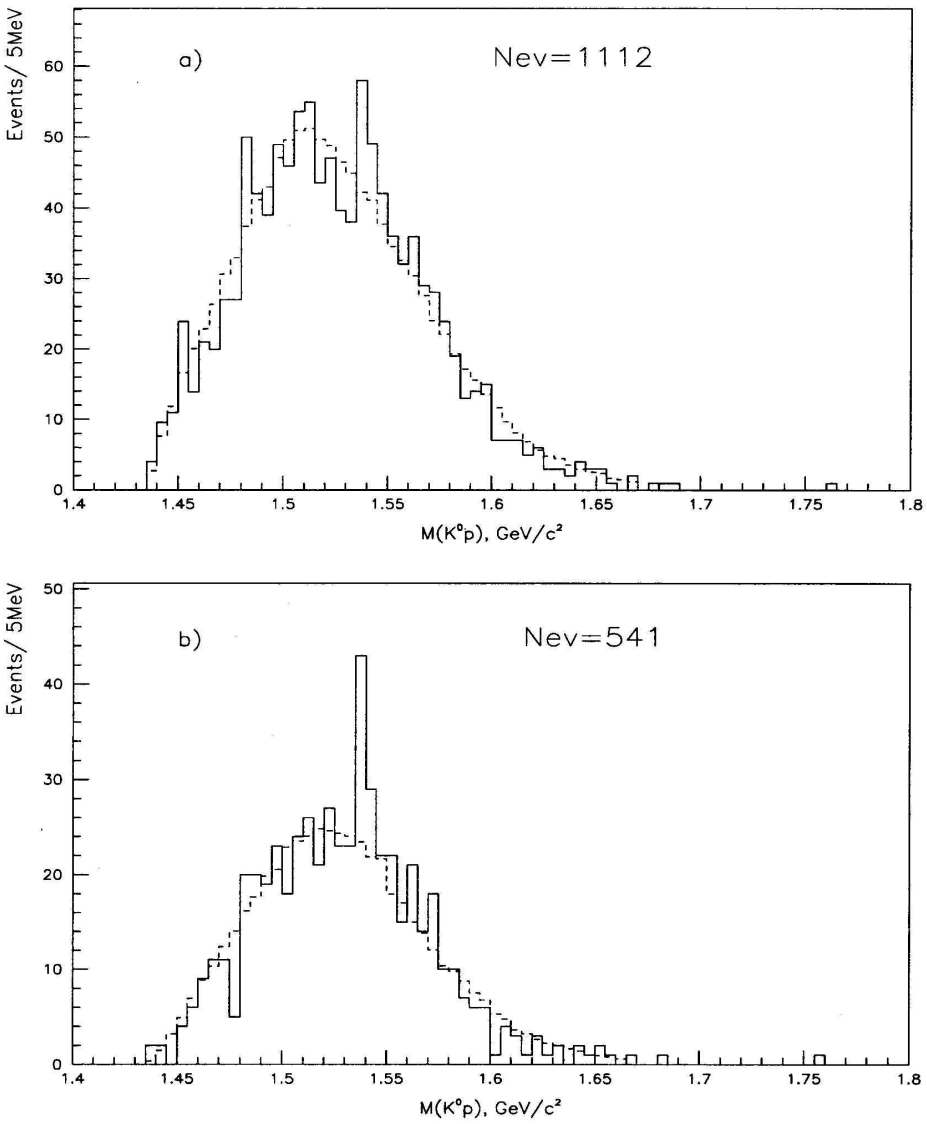

Figure 14: The invariant mass spectrum of pK^0 in the reaction $K^+Xe \to \Theta^+Xe' \to pK^0Xe'$ a) for all measured events, b)after suppressing proton and K^0 re-interactions in nuclear matter. The fit to the expected functional form is depicted by the dashed line. (From reference [54].)

The other possible pentaquark state

The chiral soliton model predicted three manifestly exotic baryon states with the Θ^+ being the lightest one, and two $S = -2$ exotic Ξ states, the Ξ^{--} and Ξ^0, within the baryon anti-decuplet. The first evidence of a possible $\Xi^{--}_{\frac{3}{2}}$ state was also reported by the NA49 collaboration [59]; a doubly negatively charged baryon with $S = -2$ was seen at 1860 MeV decaying to $\Xi^-\pi^-$. Fig. 15 shows the combined $\Xi^-\pi^-, \Xi^-\pi^+, \bar{\Xi}^+\pi^-$ and $\bar{\Xi}^+\pi^+$ invariant mass spectra, with the $\Xi^- -_{\frac{3}{2}} \rightarrow \Xi^-\pi^-$ being the exotic baryon candidate, and a possible isospin parter $\Xi^0_{\frac{3}{2}}$ decaying into $\Xi^-\pi^+$ observed at the same mass.

The evidence of the Ξ^{--} as another marker of the anti-decuplet of pentaquarks is intriguing and injected more excitement into the hadron spectroscopy community. However, the state requires corroboration, and others have challenged the analysis of the NA49 results [60]. Several new experiments at Jefferson Laboratory will certainly provide more evidence to corroborate or refute this result [61].

Did we miss the discovery of Θ^+ thirty years ago?

Partly due to the belief of the width of the pentaquark to be of the order of 100 MeV/c^2, previous searches for $S = 1$ baryon resonance did not yield any evidence for the existence of such state. However, a recent review of an old paper produced some interesting results (Fig. 16). It is totally possible that a narrow resonance in the pK^0 invariant mass spectrum was missed when people were looking for a resonance that is much wider.

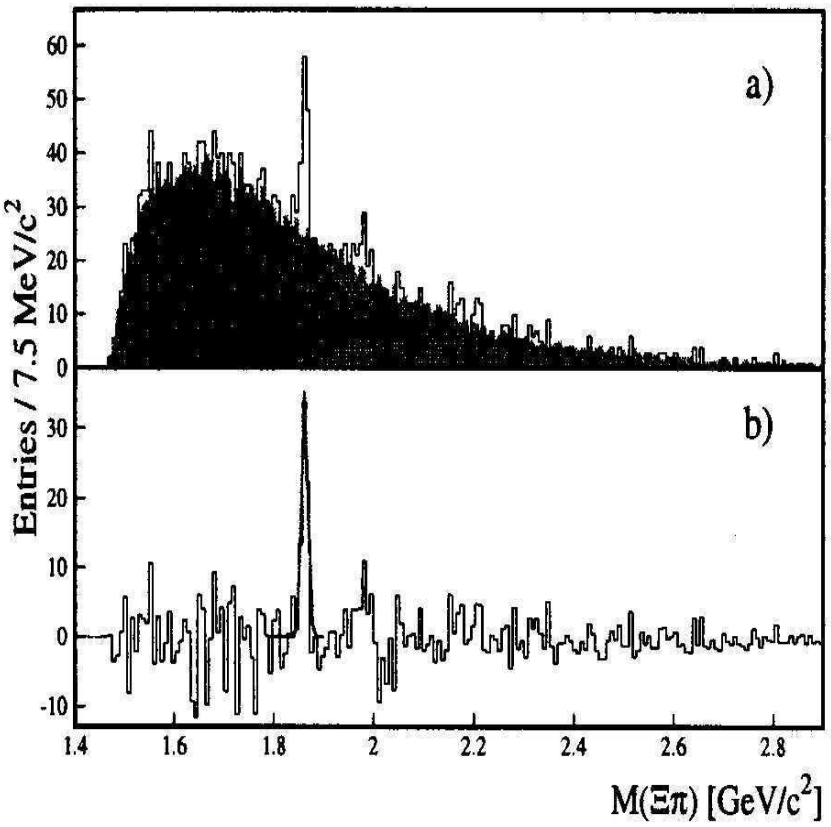

Figure 15: a) The sum of the $\Xi^-\pi^-, \Xi^-\pi^+, \bar{\Xi}^+\pi^- and \bar{\Xi}^+\pi^+$ invariant mass spectra. The shaded histogram shows background obtained from mixed-event technique. b)Background subtracted spectrum with the Gaussian fit to the peak. (From reference [59]).

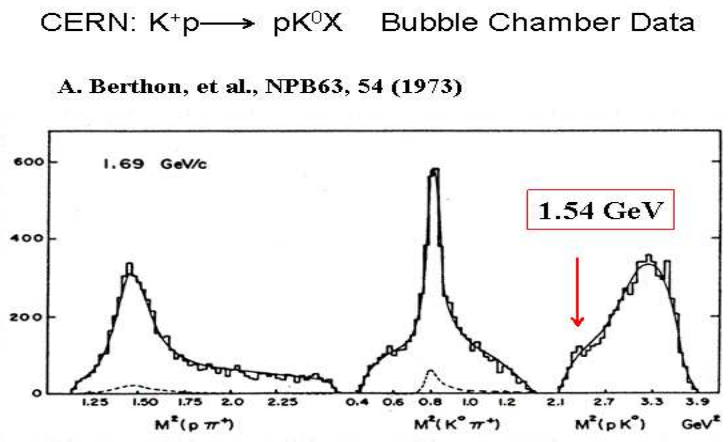

Figure 16: The results from the old CERN paper [62] showing a shoulder corresponding to mass of 1.54 GeV/c^2 in the $M^2(pK^0)$ spectrum

Θ^+ photo-production off a proton target

While the earliest possible experimental signals of the Θ^+ were identified in the photon interaction on nuclei, photo-production of the Θ^+ on a proton target is believed to have a similar cross section to that of a neutron target [63, 64, 66]. Since the first evidence of the Θ^+ baryon was reported by the LEPS Collaboration, many theoretical papers have been devoted to this topic. Various calculations of the cross section of the Θ^+ with different targets have been made [63, 64, 66]. A variety of possible production mechanisms have also been suggested. In this section, some of the predictions that have been made for Θ^+ photo-production on a proton target for different reactions will be discussed.

Θ^+ production from the reaction $\gamma p \to \pi^+ K^- \Theta^+$

If the possibility of the Θ^+ being the decay product of an intermediate resonance is exlcuded, the likely processes that can contribute to Θ^+ production in the reaction $\gamma p \to \pi^+ K^- \Theta^+$ are shown in Fig. 17. Ref [64] gives a detailed calculation of the Θ^+ cross section for both a positive and negative parity Θ^+, and the results will be summarized as follows. Assuming positive parity for the Θ^+ as predicted by the chiral soliton model [42], the amplitudes for the three diagrams are respectively:

$$M_t = i g_{\gamma K^0 K^{*0}} g_{KN\Theta} \bar{\Theta}(p_3) \gamma_5 \frac{\epsilon_{\alpha\beta\mu\nu} p_2^\alpha \epsilon_2^\beta p_4^\mu \epsilon_4^\nu}{t - m_K^2} p(p_1) \tag{9}$$

$$M_s = -e g_{K^* N\Theta} \bar{\Theta}(p_3) \epsilon_4 \cdot \gamma \frac{(p_1 + p_2) \cdot \gamma + m_N}{s - m_N^2} [1 + \frac{\kappa_p}{2m_N} p_2 \cdot \gamma] \epsilon_2 \cdot \gamma p(p_1) \tag{10}$$

$$M_u = -e g_{K^* N\Theta} \bar{\Theta}(p_3) \epsilon_2 \cdot \gamma \frac{(p_1 - p_4) \cdot \gamma + m_\Theta}{u - m_\Theta^2} \epsilon_4 \cdot \gamma p(p_1) \tag{11}$$

where $s = (p_1 - p_2)^2, t = (p_1 - p_3)^2, u = (p_1 - p_4)^2$ are the usual Mandelstam variables, with p_1, p_2, p_3, p_4 denoting the momenta of proton, photon, Θ^+, and K^{*0}, respectively. The polarization vectors of the γ and K^{*0} are given by ϵ_2, ϵ_4 respectively. The three coupling constants are obtained from different methods. $g_{\gamma K^0 K^{*0}}$ denotes the photon anomalous parity interaction with the kaons, and has the dimension of inverse of energy; its value is given by $g_{\gamma K^0 K^{*0}} = 0.388\ GeV^{-1}$ using the decay width $\Gamma_{K^{*0} \to K^0 \gamma} = 0.117$ [66]. $g_{KN\Theta}$ can be obtained from the $SU(3)$ symmetry relation $g_{KN\Theta} = 3 g_{\pi N N_{10}}$. The coupling constant $g_{\pi N N_{10}}$ between πN and the pentaquark N_{10}, can be calculated from the width of the $N(1710)$, assuming it is a mixed pentaquark baryon $(\sqrt{2} N_{10} - N_8)/\sqrt{3}$, with N_{10} being a pentaquark $(uudd\bar{u}, uuddd\bar{d})$ and N_8 being the octet pentaquark $(uuds\bar{s}, uuds\bar{s})$. The result is shown to be $g_{KN\Theta} \sim 3.0$. Similarly for $g_{K^* N\Theta}$, it can be derived from the $SU(3)$ relation $g_{K^* N\Theta} = 3 g_{\rho N N(1710)}$,

and is calculated to be $g_{K^*N\Theta} = \pm 1.8$ or $g_{K^*N\Theta} = 0$. In addition, form factors at the strong interaction vertices are needed to account for the internal structure of hadrons. Different covariant form factors for the s, t and u-channel amplitudes are given by:

$$F(x) = \frac{\Lambda^4}{\Lambda^4 + (x - m_x^2)^2} \tag{12}$$

where $x = s, t$, and u with corresponding masses $m_x = m_N, m_K$, and m_Θ of the off-shell particles at the strong interaction vertices. Λ is the cutoff parameter that represents the off-shell momentum above which hadron internal structure becomes important; the value of Λ is determined empirically. An additional contact term is needed in the interaction Lagrangian to retain gauge invariance:

$$M_c = -2eg_{K^*N\Theta}\bar{\Theta}(p_3)\epsilon_4 \cdot \gamma[\frac{\epsilon_2 \cdot p_1}{s - m_N^2}(\hat{F} - F(s)) + \frac{\epsilon_2 \cdot p_3}{u - m_\Theta^2}(\hat{F} - F(u))]p(p_1) \tag{13}$$

where $\hat{F}$ is given by $\hat{F} = F(s) + F(u) - F(s)F(u)$. Λ is determined empirically to be 0.8 GeV, similar to the soft form factor used to describe the lambda photo-proton production in Ref. [65]. The resulting differential cross section for the reaction $\gamma p \to \bar{K}^{*0}\Theta^+$ is thus:

$$\frac{d\sigma}{dt} = \frac{1}{256\pi s p_i^2}|F(t)M_t + F(s)M_s + F(u)M_u + M_c|^2 \tag{14}$$

where p_i is the magnitude of the initial three momenta in the center-of-mass frame, i.e., $p_i = (s - m_N^2)/2\sqrt{s}$. Considering the $\bar{K}^{*0}$ decaying branching ratio of π^+K^- and $\pi^0\bar{K}^0$ is 2 to 1, the differential cross section for the reaction $\gamma p \to K^-\pi^+\Theta^+$ is 2/3 of what is given by Eq. 14. This cross section only takes into account the diagrams shown in Fig. 17, and ignores the possible production of the Θ^+ through

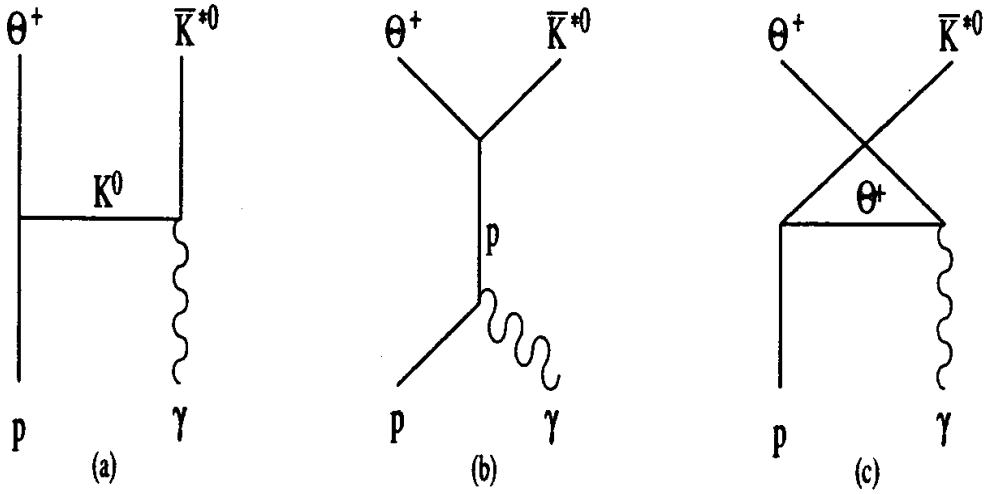

Figure 17: Diagrams for Θ^+ production in the reaction $\gamma p \to \pi^+ K^- \Theta^+$

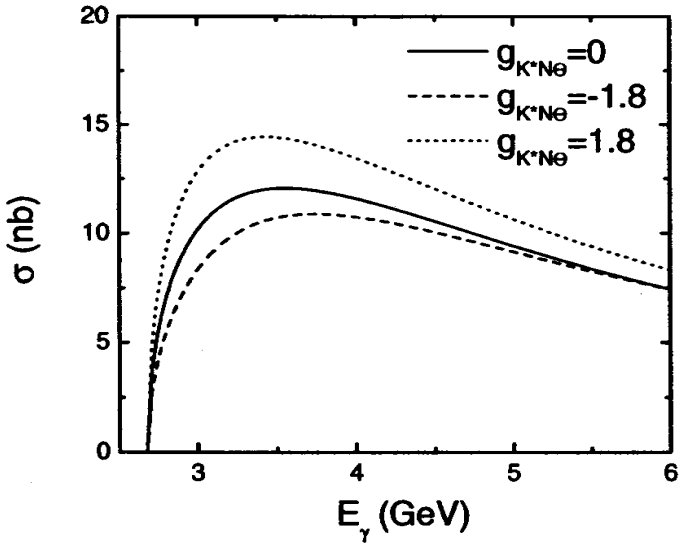

Figure 18: Assuming positive parity, the total cross section Θ^+ production in the reaction $\gamma p \to \pi^+ K^- \Theta^+$ as a function of photon energy with form factors

an intermediate nucleon resonance. The total cross section of the Θ^+ for the reaction $\gamma p \to \bar{K}^{*0}\Theta^+$ is plotted in Fig. 18.

On the other hand, lattice QCD calculations have indicated that the reported Θ^+ mass is consistent with negative parity. The total cross section of a negative parity Θ^+ is shown in Fig. 19.

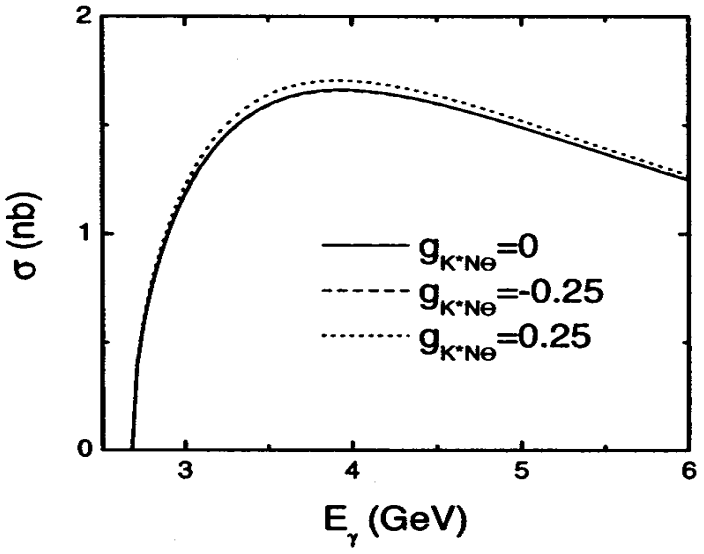

Figure 19: Assuming negative parity, the total cross section Θ^+ production in the reaction $\gamma p \to \pi^+ K^- \Theta^+$ as a function of photon energy with form factors.

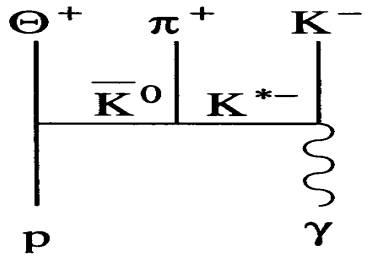

Figure 20: Diagrams for Θ^+ production in the reaction $\gamma p \to \pi^+ K^- \Theta^+$ via K^{*-} exchange

Θ^+ production from the reaction $\gamma p \to \bar{K}^0 \Theta^+$

There are also other possible production mechanisms of the Θ^+ in photon-proton reaction; Ref [63] gives a detailed calculation of the cross section. In Fig. 21, Θ^+ production from photon-proton reactions with two-body final states are illustrated. Θ^+ production for three-body final states are shown in Fig. 22. The resulting cross section are shown in Fig. 23. A notable feature of the total cross section for the Θ^+ is that when the photon energy increases, the two-body final states decrease faster than the three-body final states. The two-body final states total cross sections are expected to be much higher than the three-body contributions at lower energy.

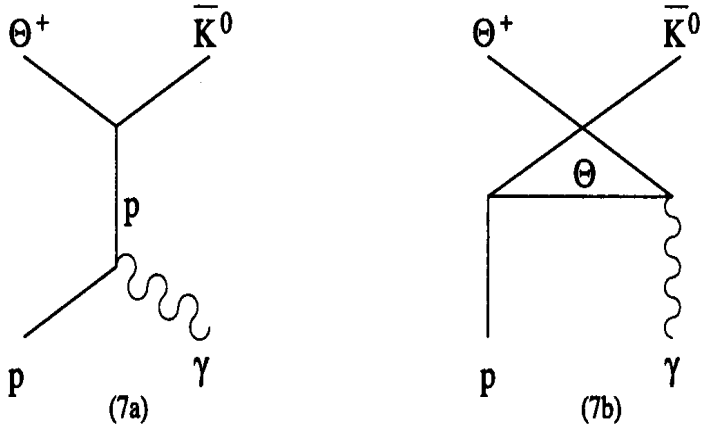

Figure 21: Possible diagrams for Θ^+ photo-production off a proton target with two-body final state

Θ^+ production through an intermediate baryon resonance

Photo-production of the Θ^+ on the nucleon is usually calculated within hadronic models, since perturbative QCD is not applicable [68, 66, 69]. From the naive quark level, each time a quark-antiquark pair is created from the vacuum there should be a penalty. For the reaction $\gamma N \to K\Theta^+$, where K can be either a ground state K or K^*,

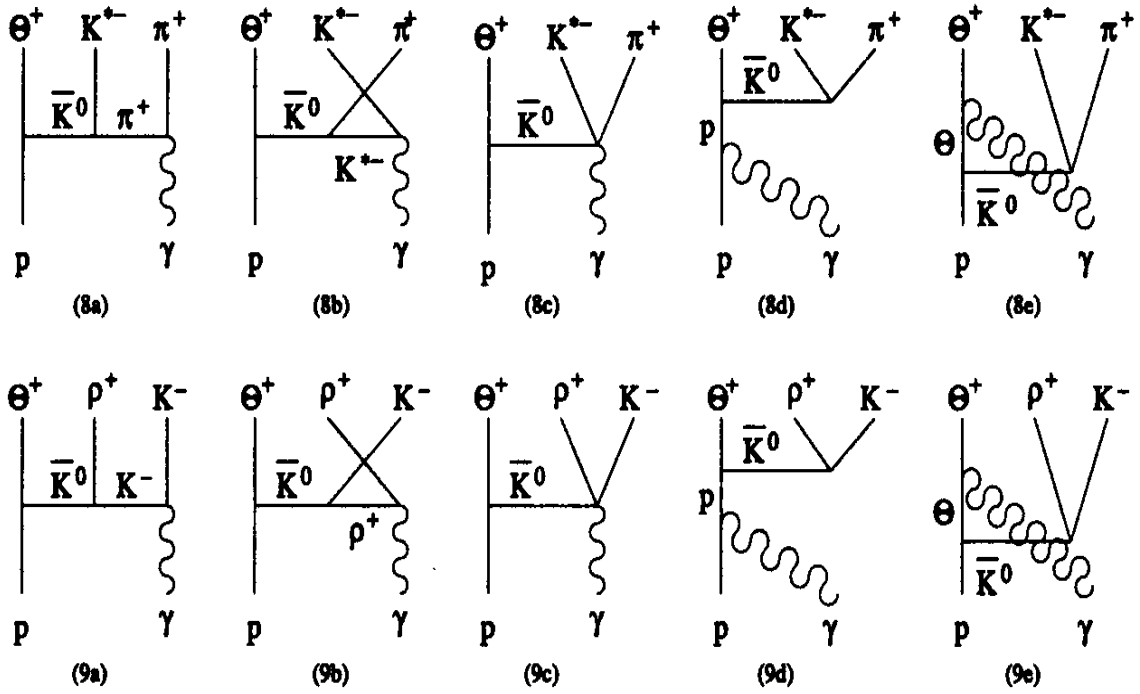

Figure 22: Possible diagrams for Θ^+ photo-production off a proton target with three-body final state

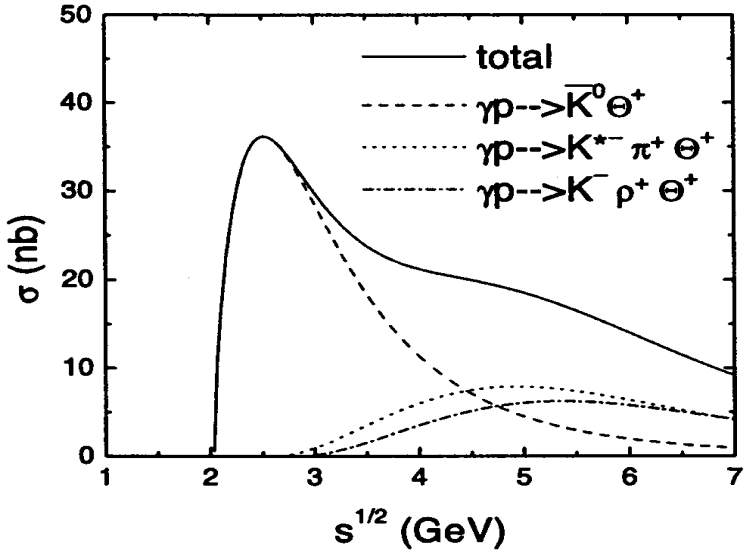

Figure 23: Cross sections for for Θ^+ photo-production off a proton target as functions of center-of-mass energy: total (solid curve), $\gamma p \to \bar{K^0}\Theta^+$ (dashed curve), $\gamma p \to K^{*-}\pi^+\Theta^+$ (dotted curve), and $\gamma p \to K^-\rho^+\Theta^+$ (dash-dotted curve).

the dominant process is expected to be $q\bar{q}$ pair creation from the photon. However, it has been pointed out that the Θ^+ could be an isotensor pentaquark. The narrow width thus can be explained by isospin violation in the decay to the kinematically allowed channels nK^+ and pK^0 [67]. In this scenario, the t-channel processes for Θ^+ production, such as the one shown the Fig. 17, would be forbidden due to isospin conservation. Thus S-channel diagrams such as the one shown in Fig. 24 should also be considered. Non-resonant $K\Theta^+$ mechanisms are therefore also competitive.

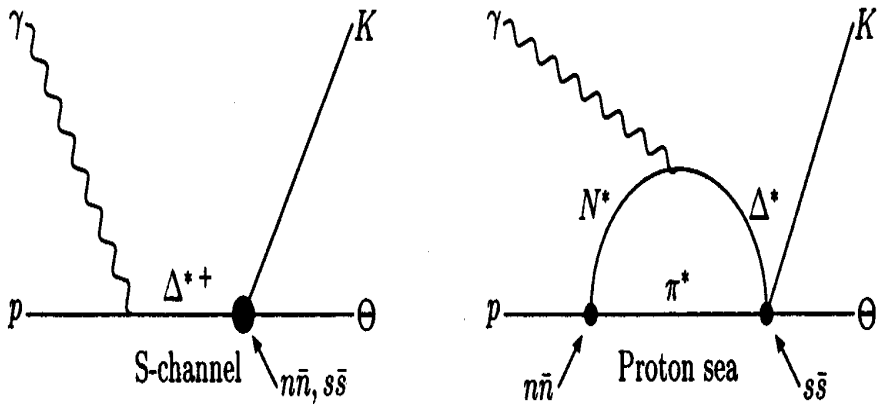

Figure 24: Possible Θ^+ production mechanisms. Left: S-channel diagram where the photon excites the proton first and two $q\bar{q}$ pairs are created later. Right: Proton sea diagram where the light $n\bar{n}$ quark pair is created first and $s\bar{s}$ is created last.

Similarly, in the case of $\gamma p \to \pi^+ K^- \Theta^+$, it is possible to produce the Θ^+ through intermediate resonances, such as $\gamma p \to \Delta^* \pi^+, \Delta^* \to \Theta^+ K^-$ (Fig. 25), while an intermediate N^* is forbidden by isospin symmetry. Such process involves two quark-antiquark pair creations from the vacuum in the decay of $\Delta^* \to \Theta^+ K^-$, if we assume the Δ^* is a three-quark state. It thus could be competitive with other non-resonant $K^* \Theta^+$ and $K^- \pi^+ \Theta^+$ mechanisms.

Similarly, it has also been suggested that the Θ^+ signal reported by the CLAS

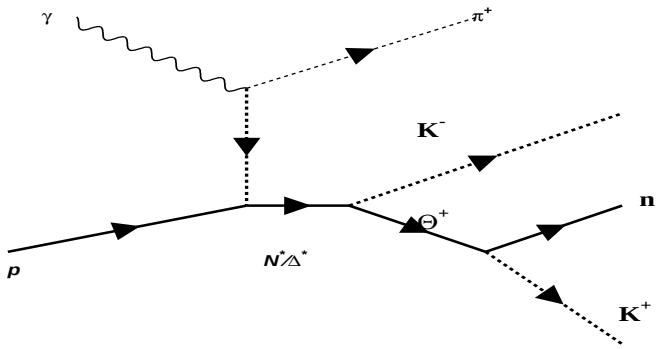

Figure 25: Possible Θ^+ production mechanism in the reaction $\gamma p \to \pi^+ K^- \Theta^+$ via intermediate nucleon

Collaboration [51] could also be a decay product of an intermediate nucleon (Fig. 26), instead of the re-scattering mechanism suggested in the paper (Fig. 13). In this thesis, the result of this analysis of the reaction $\gamma p \to \pi^+ K^- \Theta^+$ at CLAS with a photon energy range of $3.0 - 5.47$ GeV will be presented. Competing production mechanisms, such as discussed previously, will also be examined.

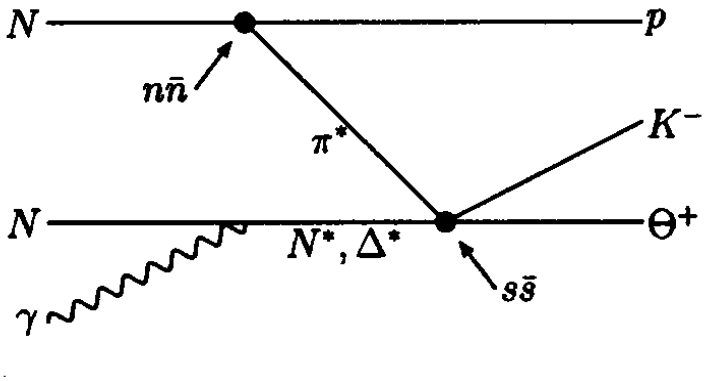

Figure 26: Possible Θ^+ photo-production mechanism off a target. N can be either neutron or proton.

CHAPTER II

EXPERIMENT APPARATUS

The data that was analyzed in this thesis came from three experiments conducted at Thomas Jefferson National Accelerator Facility (TJNAF), in Newport News, Virginia. All three experiments used a photon beam with energies ranging from 3.0 to 5.47 GeV produced through bremsstrahlung radiation of a 5.7GeV electron beam produced by CEBAF(Continuous Electron Beam Accelerator Facility). The photon beam was incident on a liquid hydrogen target at CLAS (CEBAF Large Acceptance Spectrometer) [73]. The Hall B tagging system was used to tag the photon beam [81].

The Continuous Electron Beam Accelerator Facility

The Continuous Electron Beam Accelerator Facility (CEBAF) delivers a high-intensity continuous electron beam with an energy ranging from 0.8 GeV to 6.1 GeV. Electrons are pre-accelerated to 67 MeV before being injected into the North linear accelerator (Linac). Each time the electron passes through one of the Linear Accelerators it will obtain an energy boost of 0.6 GeV. Because the beam is continuous, different electron beam energies can coexist in the same linac. The typical linac setting allows beam energies available to all the halls from 1.2 to 6.0 GeV in multiples of 1.2 GeV. At the end of the South Linear Accelerator, the electron beam can be extracted to three different experimental halls (See Fig. 27). The electrons beam circulates in bunches separated by about 2/3 ns. The beam separator/extractor extracts

the electrons from the main accelerator and delivers beams to the three halls, while these three beams each come in bunches separated by 2.004 ns.

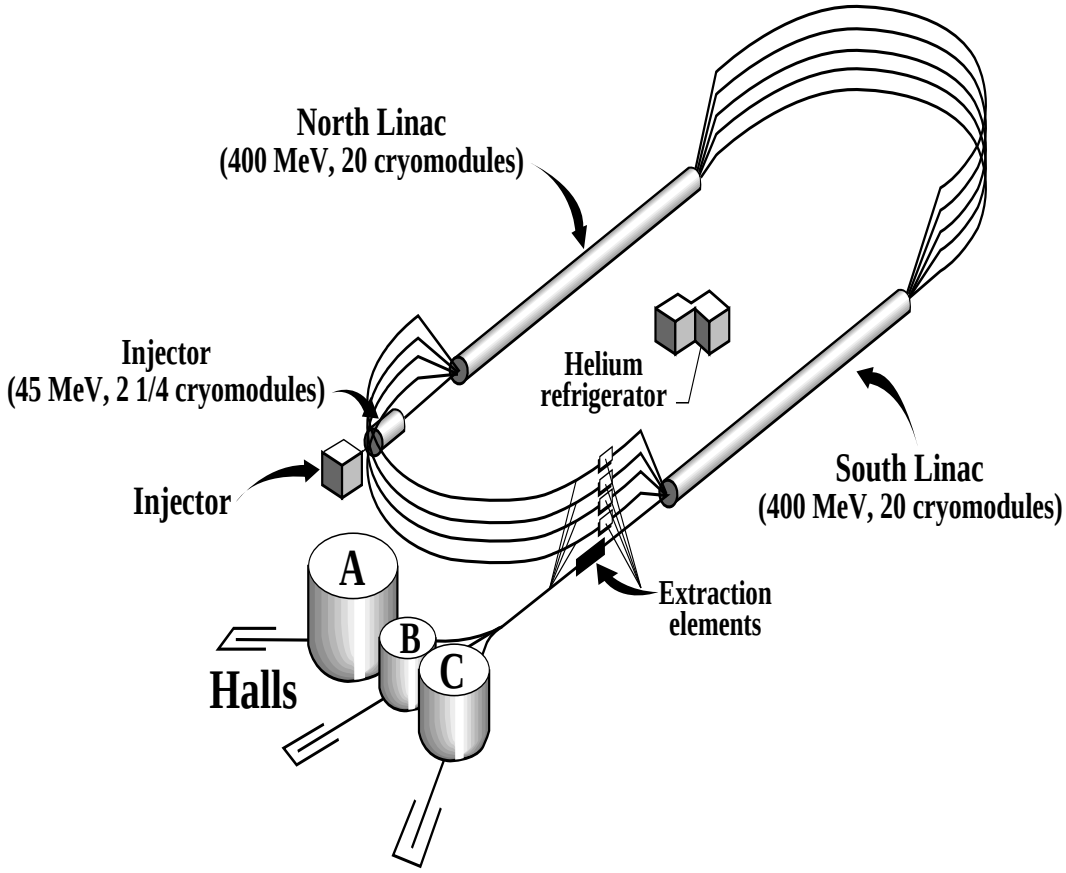

Figure 27: The main elements of the Continuous Electron Beam Accelerator Facility (CEBAF) at Jefferson Laboratory, Newport News, Virginia, USA

The Superconducting Linear Accelerators

At the injector, the electrons of 100 kV were produced by electron guns and then accelerated to 40-80 MeV before entering the linac. Each linac was designed to accelerate the electrons by 400 MeV per pass [71]. In practice, the linacs are capable of higher performance (close to 600 MeV) than the design value. The Linear accelerators are made up of a series of RF cavities powered by independent klystrons that are adjusted so that the phase and energy gradient of the cavity maximizes

performance. The RF cavities are made of niobium and cooled to about 2K using a liquid helium bath to achieve superconductivity, allowing current to flow continuously with no resistance.

The Recirculation Arcs

To achieve higher energy electron beams, a series of dipole magnets in the recirculation arcs are used. The electrons are turned 180^o to pass through the linac multiple times. Since electrons of different energies (momentum) will bend differently for the same magnetic field, the electron beam is split into as many as five separate beams of different energies before going through different dipole magnets along the arcs. At the end of the recirculation arcs, the beams of different energies are recombined before reentering the linacs. The arcs are designed to prevent the different beams from losing their synchronization upon recombinations [71].

The Experimental Halls

Currently, there are three experimental halls at CEBAF: Hall A, Hall B, and Hall C. Both Hall A and Hall C provide two-arm spectrometers capable of making high precision measurement, but limited by phase space and angular acceptance. Hall A has two identical focusing high-resolution spectrometers with a maximum momentum of 4 GeV/c. Hall C has two symmetric focusing spectrometers: one featuring acceptance of high-momentum particles, the other a short path length for the detection of decaying particles. Hall B is the home of the CLAS (CEBAF Large Acceptance

Spectrometer) detector, which is a large acceptance spectrometer of almost 4π solid-angle coverage and able to detect multiple particle final states. The CLAS detector is discussed in detail in the following section.

Hall B Detector Components

Hall B is one of the end stations as shown in Fig. 27. The CLAS detector (Fig. 28), located in hall B, can conduct both electro-production and photo-production experiments. The physics research of Hall B spans a broad range of programs: hadron spectroscopy, comprehensive study of nucleon structure, transition form factors of baryon resonances, measurements of the spin structure of nucleons and studies of nucleon correlations inside nuclei. These programs require large-acceptance particle detection and CLAS is an ideal place for such purposes. The CLAS detector is a nearly 4π toroidal spectrometer that includes an array of different detectors. It is based on a novel six-coil toroidal magnet which provides a largely azimuthal field distribution. The particle detection system consists of drift chambers for charged particle tracking, gas $\check{C}$erenkov counters for electron identification, scintillation counters for time-of-flight measurement, and electromagnetic calorimeters to detect showering particles (photons and electrons) and neutrons.

Torus Magnet

The CLAS magnetic field is generated by six superconducting coils arranged in a toroidal geometry around the beam line and thus provides the tool for momentum analysis for charged particles. Each coil has 4 layers of 54 turns of aluminum-stabilized

Figure 28: The CLAS detector is composed of a series of detectors that are designed for various purposes.

NbTi/Cu conductor. The superconductivity is achieved by cooling the coils to 4.5 K by forcing super-critical helium through cooling tubes located at the edge of the windings. The magnet is about 5 m in diameter, and 5 m in length. The layout of the coils and contours of constant absolute field strength are shown on the top plot of Fig. 29. The bottom figure shows the magnetic field vectors in a plane perpendicular to the torus axis at the target position (CLAS center). The kidney-shape of the coils results in high field integral for forward-going particles and a lower field integral for particles emitted at larger angles. This coil geometry allows a central field-free volume for the operation of a polarized target.

The maximum design current of the torus magnet is 3860 A, which provides an integral magnetic field of 2.5 Telsa×meter in the forward direction, and only 0.6 Telsa×meter at scattering angle of 90^o. In operation, however, it is limited to 87% (3375 A) of the maximum current due to mechanical concerns. For the nominal magnet polarity, negatively charged particles are bent inward towards the beam line and positive particles are bent outwards away from the beam. This results in better acceptance for positively charged particles than negatively charged ones. When desired, the torus current can be lowered to allow better acceptance of negative particles, while the momentum resolution will be reduced. The magnet polarity can also be reversed.

Drift Chambers

In CLAS, charged particles are tracked with drift chambers which are grouped into three regions [74, 75, 76, 77]. Region 1 is the closest to the target with almost zero field inside the torus core; these chambers determine the initial direction of the tracks.

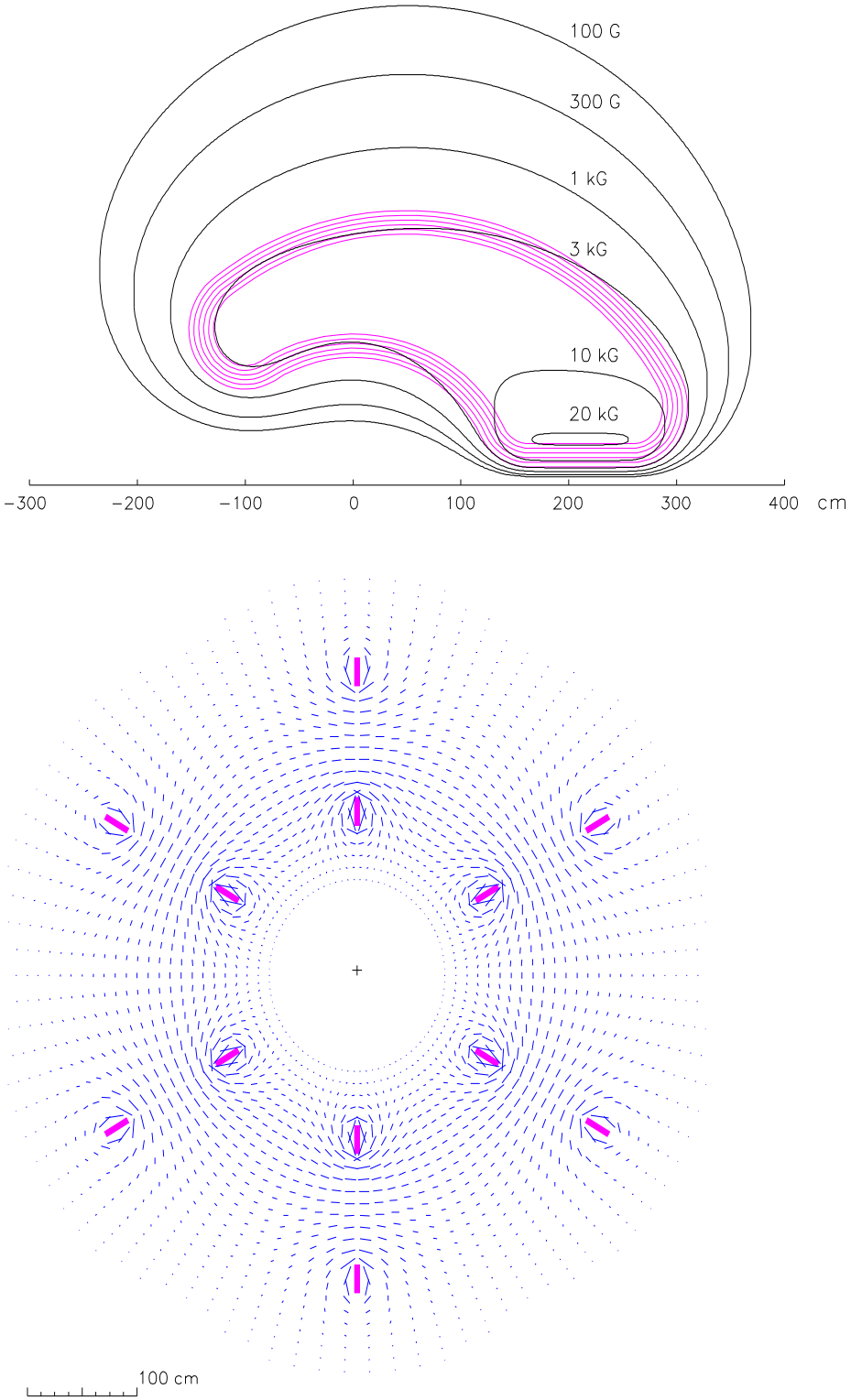

Figure 29: Top: Contours of constant absolute magnetic field for the CLAS toroid in the midplane between tow coils. Bottom: Magnetic field vectors for the CLAS toroid transverse to the beam in a plane centered on the target. The length of each line segment is proportional to the field strength at that point. The six coils are seen in cross section.

Region 2 lies between the torus coils where the toroidal magnetic field is strong, and provides a second measurement of the particle track when curvature is maximized, to achieve good energy resolution. Region 3 is outside the coils where the magnetic field is low, and determines the final direction of the charged particles which are heading toward the outer time-of-flight counters, $\check{C}$erenkov counters and the Electromagnetic Calorimeters. All three regions consist of 6 sectors corresponding to the six torus coils segmentation. Each region within one given sector contains one axial superlayer, which is perpendicular to the midplane of each sector and approximately parallel to the magnetic field, arranged in six layers (4 layers for Region 1) and one stereo superlayer with sense wires in six layers at an angle of 6 degrees with respect to the axial wires to provide the azimuthal information. Each superlayer is grouped into 6 layers in Region 2 and 3, while spatial volume limits it to 4 layers in Region 1. The wires are arranged into a hexagonal pattern, with 192 sense wires in each layer (Fig. 31) in Region 2 and 3, and 128 wires in Region 1. Each superlayer is surrounded with a row of guard wires to minimize edge effects. There are a total of 35,148 sense wires in the drift chamber system.

The drift chambers are filled with a gas mixture of 88% argon (Ar) and 12% CO_2 from considerations of system safety as well as operation lifetime. The gas mixture has a drift velocity of about 4 cm/μs. The cell size for Region 1, 2, and 3 are about 1.5, 2.7 and 4.3 cm, respectively.

The tracking resolution is a function of single-wire resolution which depends on where within a cell the track has passed. Within a given layer, it is estimated by fitting a track to all hits except those in that layer. The fit residual is the difference

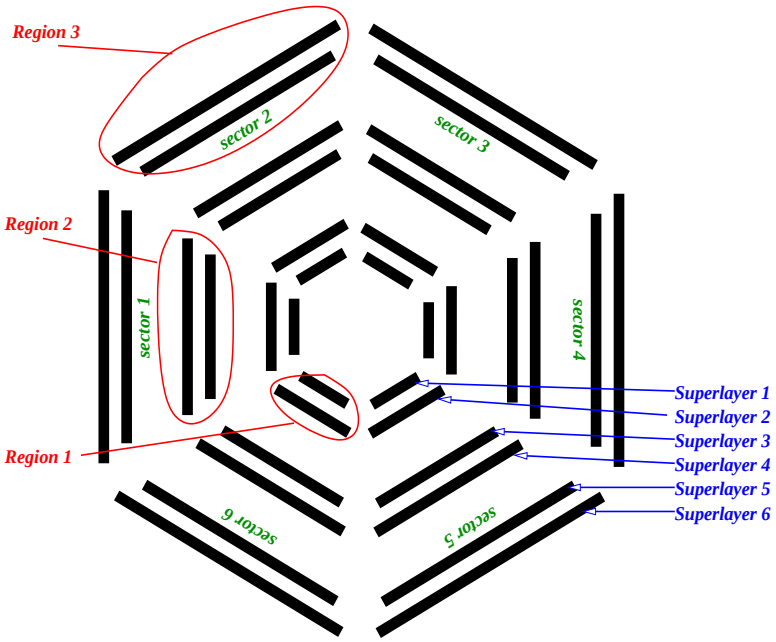

Figure 30: The CLAS Drift chambers schematic showing the names convention for regions and superlayers (from [88].

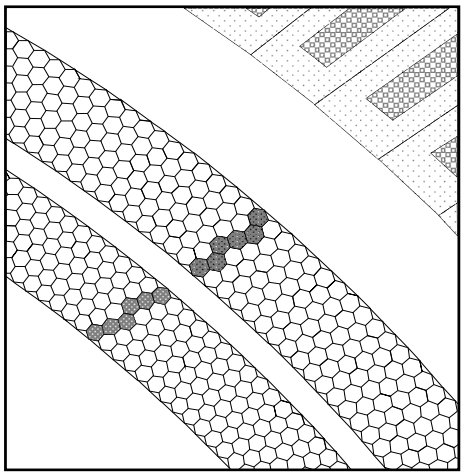

Figure 31: Representations of a portion of a Region 3 chamber showing the layout of its two superlayers. The sense wires are at the center of each hexagon and the field wires are at the vertices. The perimeters of the hexagonal cells represents no material and are only shown to outline the wire layout. The highlighted drift cells that have fired show a passing charged particle. The upper right corner of the picture shows the edge of Čerenkov counter.

between the fitted distance -of-closest-approach (DOCA) of the track and the DOCA value calculated from the drift time in the excluded layer. The whole-cell average resolution is about 310, 315, and 380μm for R1, R2, and R3, respectively. The resolution is better in the mid-portion of the cell due to the Poisson distribution of ion-pair production along the path of the primary ion near the sense wire, as well as time-walk effects and the divergence of the electric field lines near the field wire. Fig. 32 shows the rms width of the track-hit residual distribution plotted versus DOCA for Region 2.

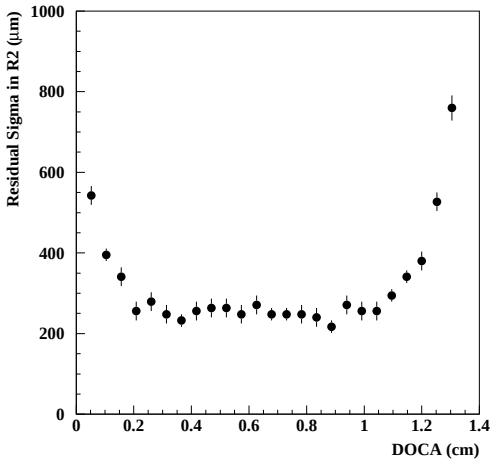

Figure 32: Track-hit residual rms width as a function for the fitted DOCA for Region 2

Čerenkov Counters

The Čerenkov Counter [78] is used for both e/π separation and triggering on electrons, based on the principle of Čerenkov Radiation: a fast particle with velocity $v > \frac{c}{n}$ where n is the gas refraction index will produce Čerenkov light in a narrow

cone in the forward direction. The light is focused by mirrors and collected by Photomultiplier Tubes (PMT). The Čerenkov Counter array is placed between the Drift Chamber Region 3 and the time-of-flight Scintillator system, about 4m from the target. Each of the six sectors was divided into 18 regions of θ, and each θ segment was divided into two modules symmetric with respect to the middle plane. This results in a total of 216 light collection modules. Each module consists of two focusing mirrors, a "winston" light collection cone, and cylindrical mirror at the base of the cone (Fig. 33). The light is collected by the PMT mounted at the Winston cone base. The PMTs and the Winston cones are placed in the regions of ϕ that are already obscured by the magnet coils in order to maximize solid-angle coverage. The CLAS Čerenkov detector covers a polar angle range of $7^o < \theta < 45^o$ in the forward direction and full azimuthal angle range.

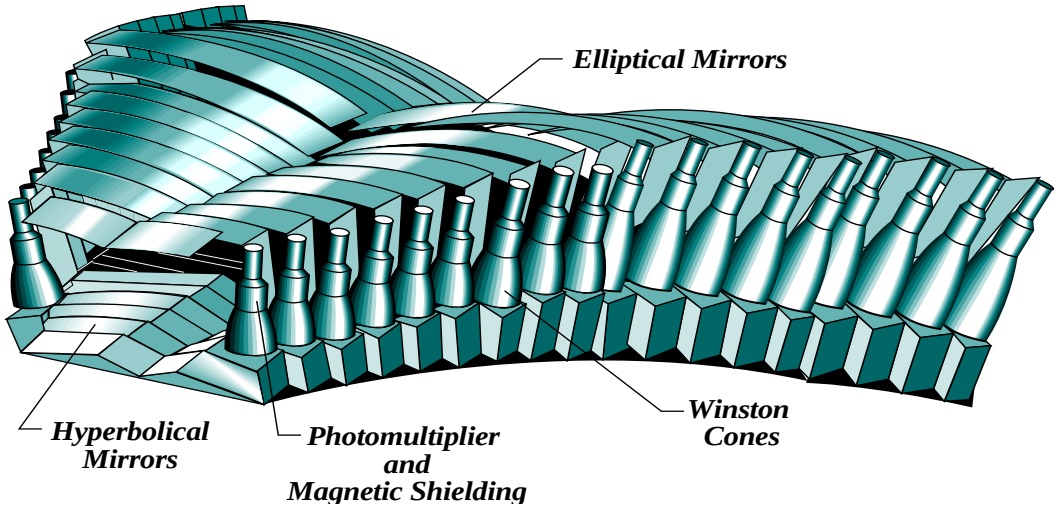

Figure 33: A schematic drawing of the array of optical modules in one of the six Čerenkov Counter sectors.

The radiator gas used in the Čerenkov detector is perfluorobutane (C_4F_10) with

an index of refraction of 1.00153. This results in a high photon yield and a pion momentum threshold of 2.5 GeV/c. Each sector holds approximately six cubic meters of gas. An in-bending electron, traversing the active volume of the detector, induces typically 4-5 photoelectrons. A typical trajectory of the light produced by an electron passing through the Čerenkov detector is illustrated in Fig. 33. In photo-production experiment, the Čerenkov Counter is usually not used for triggering.

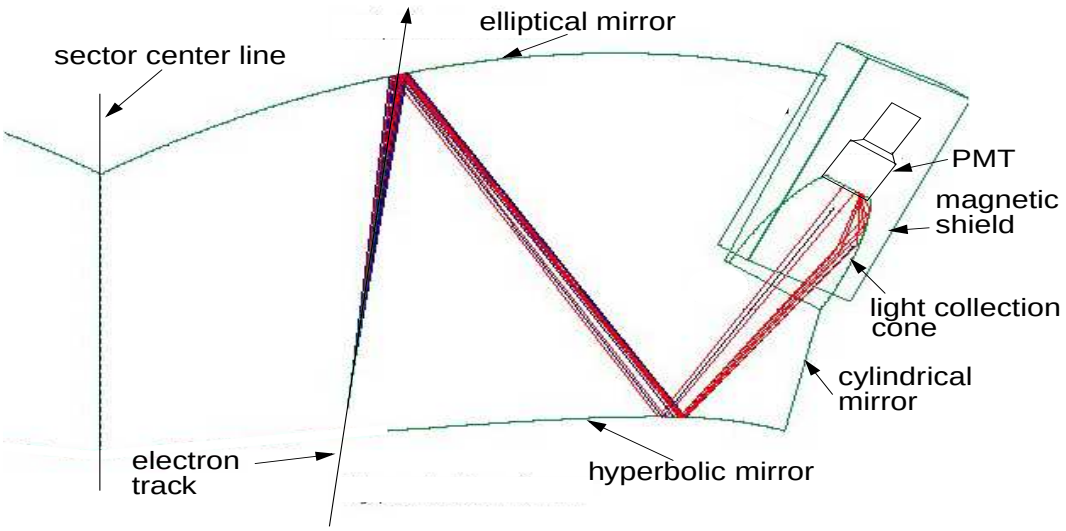

Figure 34: Optical arrangement of one of 216 optical modules of the CLAS Čerenkov detector, showing the optical and light collection components. Note that the Čerenkov PMTs lie in the ϕ region obscured by the magnet coils.

Time-of-flight system

In CLAS the time-of-flight (TOF) system [79] provides the means of charged particle identification and can be used in the triggering. It is located radially outside the Čerenkov counters but in front of the calorimeters (Fig. 28). It is essential for the time-of-flight system to achieve a good enough timing resolution to perform charged particle identification. The system was also designed to be capable of operating in a

high-rate environment. The time-of-flight system for CLAS is composed of scintillation counters that are 5.08 cm thick, 15 and 22 cm wide, and with lengths varying from 32 cm at the most forward angle to 445 cm at larger angles. Each of the six sectors has 57 scintillators with a PMT mounted at each end. The last 18 of these are paired into nine logical counters, each with an effective width of 44 cm. This grouping results in a total of 48 logical counters. For the forward-angle system, 15-cm-wide scintillators and 2-inch PMTs are used. For the large-angle system, a 22-cm width coupled to bent and twisted light guides and 3-inch PMTs was selected. All of the components of the system have been designed to optimize the timing resolution. The intrinsic timing resolution varies from about 80 ps for the short counters to 160 ps for the longer counters. Reconstruction of interaction particles for photon-runs have timing resolution up to 160ps for the shorter counters and around 200ps for longer counters.

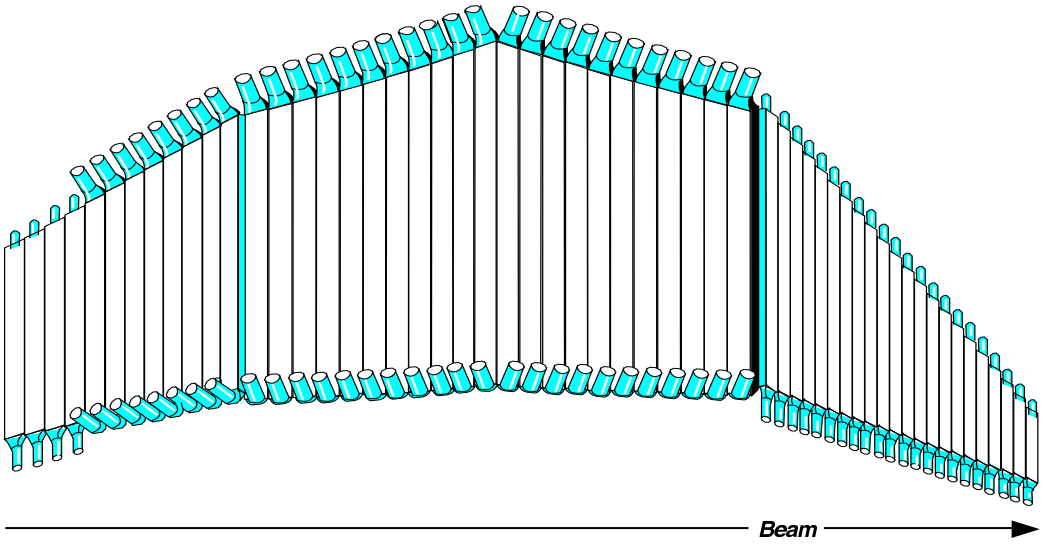

Figure 35: View of TOF counters in one sector showing the grouping into four panels.

The TOF system can also be used for energy-loss measurements and velocity

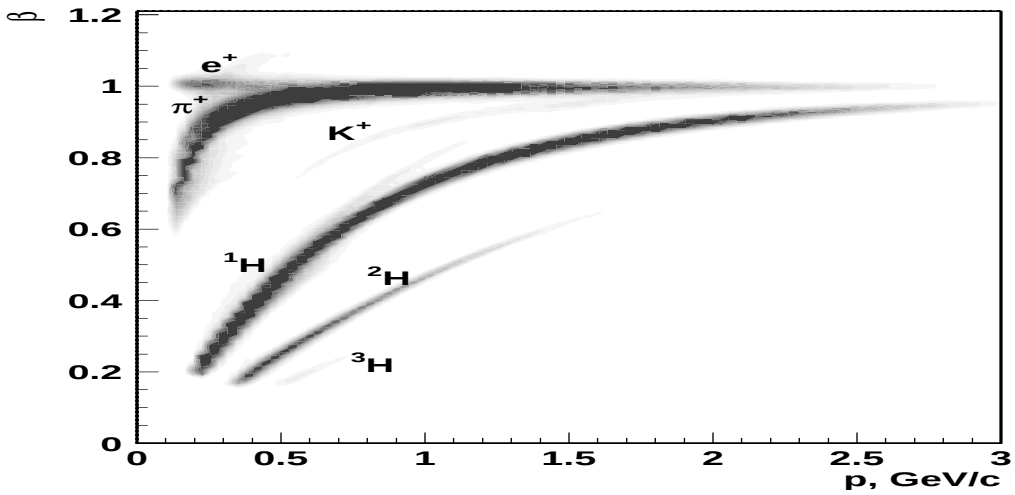

Figure 36: β vs momentum for charged hadrons. The six visible bands from top to bottom are: e^+, π^+, K^+, proton and deuteron and ^3H.

determinations (Fig. 37), and therefore provide an independent means for the identification of slow particles, which can be used for calibration purpose before time-based particle identification becomes available.

Electromagnetic Calorimeter

The Electromagnetic Calorimeter (EC) [80] is used to provide the primary electron trigger (for electrons with energies above 0.5 GeV) for CLAS as well as pion rejection, detection of photons at energies above 0.2 GeV for π^0 and η reconstruction as well as neutron detection. The detector is located just behind the TOF, about 5m from the CLAS center, and covers the θ range of 8^o to 45^o. The calorimeter is made of alternating layers of scintillator strips and lead sheets with a total thickness of 16 radiation lengths. For each EC module, the lead-scintillator sandwich is contained within a volume with the shape of a nearly equilateral triangle. There are 39 layers

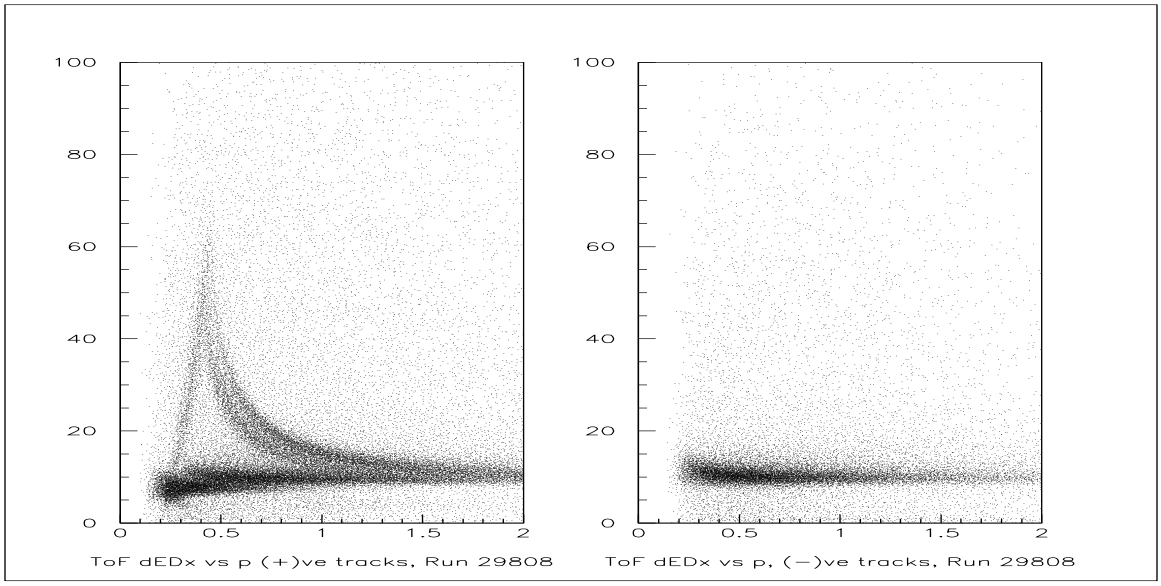

Figure 37: Energy deposited in scintillator as a function of particle momentum. Protons and pions can be distinguished.

in the sandwich, each consisting of a 10 mm thick scintillator followed by a 2.2 mm thick lead sheet. The calorimeter uses a "projective" geometry pointing to the normal target position, in which the area of each successive layer increases with the distance. For readout purposes, each layer is made of 36 strips parallel to one side of the triangle, with the orientation of the strips rotated by 120^o in each successive layer (Fig. 38). The three orientations, or views (labeled U, V, and W), each contain 13 layers, providing stereo information on the location of energy deposition. Each view is further subdivided into an inner (5 layers) and outer (8 layers) stack, to provide longitudinal sampling of the shower for improved hadron identification. There are a total of $36(\text{strips}) \times 3(\text{views}) \times 2(\text{stacks}) \times 6(\text{sectors}) = 1296$ PMTs and 8424 scintillator strips in the six EC modules.

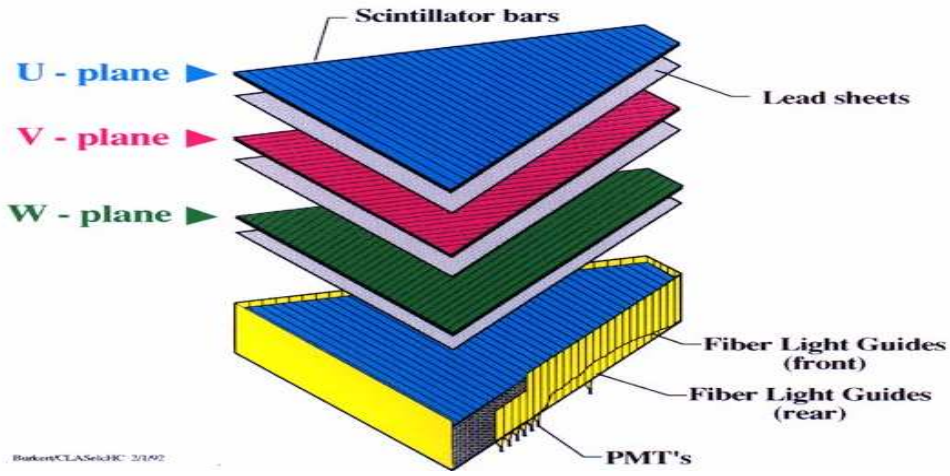

Figure 38: Exploded view of one of the six CLAS EC modules.

Start Counter

In order to identify particles using TOF, one has to determine the event start time (vertex time). For electron runs, the beam bunch (499MHz) can be determined by identifying the final-state electron (with a combination of Čerenkov and calorimeter information), and tracing the $\beta = 1$ (which is true for almost all the electrons detected in CLAS) particle back to the interaction points. For tagged photon experiments, independent information about the beam bucket is obtained through another counter: the start counter [82].

The start counter is a detector only used in photo-production experiments to determine which photon started the event. It is a small detector that surrounds the target region with 3 pairs of thin scintillators each folded half way to cover two sectors. Since the best clock we have at CEBAF is the RF time and the electrons beam buckets come in time intervals of 2.004ns, the start counter is used to select which photon caused the event. The start counters are thin enough to minimize the

multiple scattering, and large enough to cover the same solid angles in each sector as the TOF counters ($7^o < \theta < 146^o, -29^o < \phi < 29^o$). The basic layout of the start counter, seen in Fig. 39, is made up of three scintillating paddles, each covering two sectors. The particular shape of the paddle with a nose in the upstream of the target increases both the efficiency and timing resolution.

The time from the start counter is only used to determine the correct photon, which required that the software-corrected timing resolution be of the order of $\sigma \sim 350ps$. The actual start time is obtained from the RF signal once which photon caused the event is known. By including Start Courter in the trigger, the trigger rate can also be reduced in high beam intensity experiments.

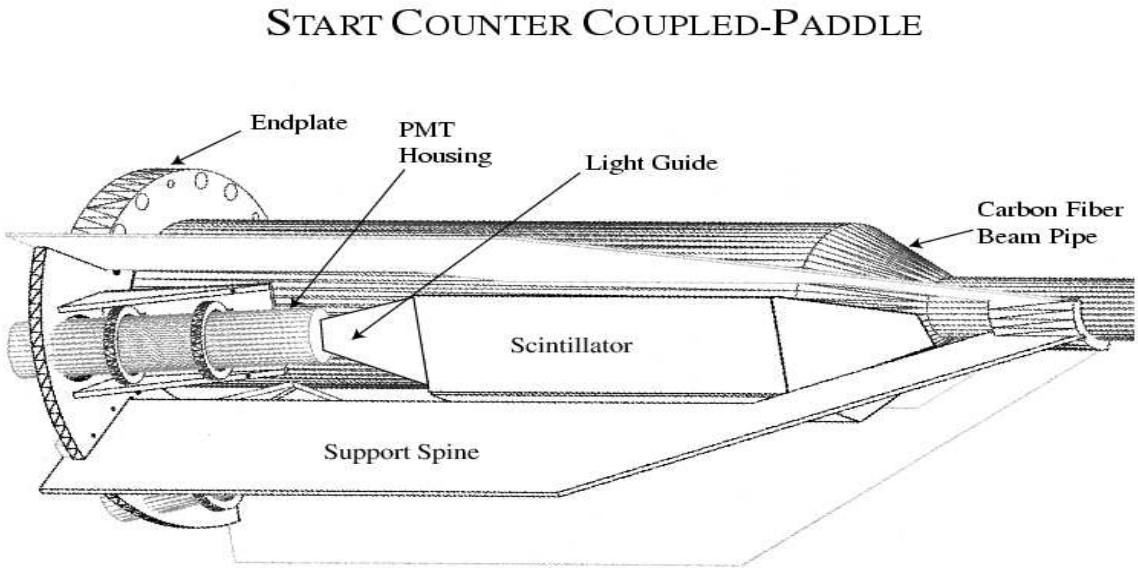

Figure 39: One Start Counter segment in place relative to the beam pipe. The target is inside the start counter.

The Tagging system in Hall B

The tagging system [81] installed in experimental Hall B at JLab produces the photon beam through bremsstrahlung radiation by passing the electron beam through a thin radiator, typically 5×10^{-5}-3×10^{-4} radiation lengths of gold plated on a thin carbon support foil. The foil is located 0.5 m in front of the tagging magnet. The system can tag photon energies over a range from 20% to 95% of the incident electron energy which can be as high as 6.1 GeV.

The produced photons continue straight ahead through the tagger magnet, toward the target, while the energy-degraded electrons from a thin bremsstrahlung radiator are bent by the tagger magnet and detected by a hodoscope containing two planar arrays of plastic scintillators. The CLAS tagging system uses a single dipole magnet to direct those electrons which do not radiate into a shielded beam dump. The first layer of the hodoscope is called E-plane, and consists of 384 partially overlapping small scintillators yielding the photon energy. Their widths (along the dispersion direction) range from 6 to 18 mm in order to subtend approximately constant momentum intervals of $3 \times 10^{-3} E_0$. Each counter optically overlaps its adjacent neighbors by one third of their respective widths, thus creating 767 separate photon energy bins that provide an energy resolution of $10^{-3} E_0$. The second layer, called T-plane, lies 20 cm downstream of the E-plane and includes 61 larger scintillators. The T-plane provides the timing resolution necessary to form a coincidence with the corresponding physical events triggered by the tagged photon. The rms timing resolution of these counters is 110 ps. Fig. 40 shows the layout of the Hall B photon-tagging system.

The fraction of photons that have been tagged and actually hit the CLAS target

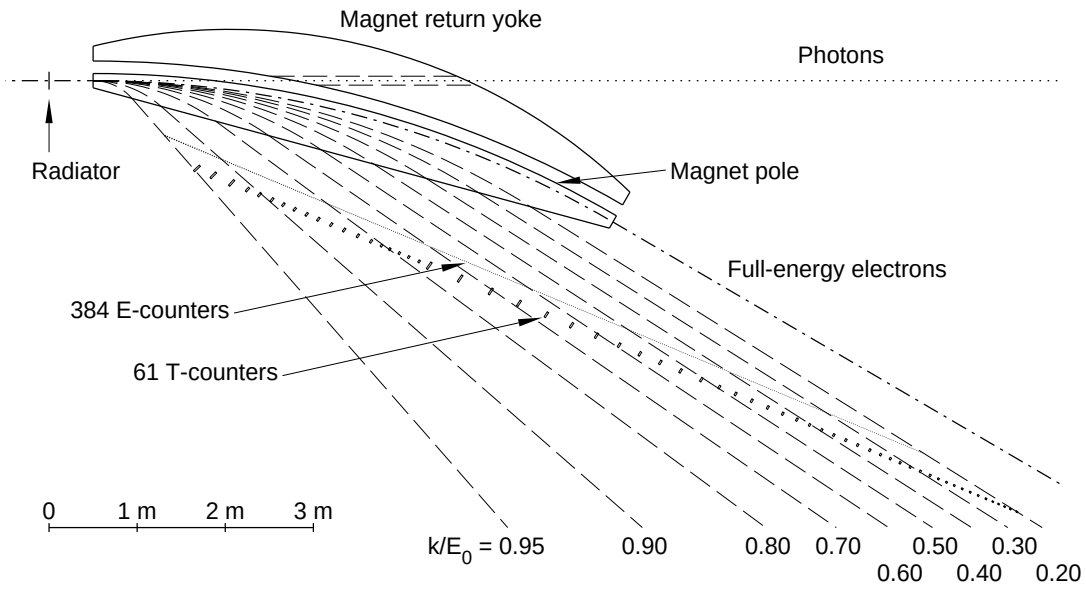

TAGELEV.PLT
D. Sober 23-Feb-99

Figure 40: Hall B photon-tagging system.

is called the tagging ratio. Typically for photon energies over most of the upper operational range, the tagging ratio is about 78%. The tagging system is designed to run at a photon flux as high as 5×10^6 photons/sec. The photon beam position and size are monitored by a fixed array of crossed scintillator fibers located 20 m behind the CLAS target.

The signal registering a photon event is a set of times from both the E-counters and the T-counters measured with FASTBUS TDCs. The T-counter output signals are fed into the Master OR (MOR) logic, which is a simple cascade of outputs of the AND gates into fast OR gates, after passing through the E-T coincidence logic module.

Trigger Setup

In photon experiments at CLAS, the level-1 (L1) trigger is produced by a coincidence of the photon trigger [83] from the tagging system and the CLAS trigger [84, 85]. The photon trigger contains signals from the MOR logic unit and the start counter (ST). The CLAS trigger is a logic combination of signals from the CLAS detectors including time-of-flight (TOF) counters and the electromagnetic calorimeter (EC).

In experiment E01_017, the CLAS trigger is two charged tracks registered by the TOF system. As for the photon trigger, the events are triggered on the first twelve T-counters in the MOR, since we are interested in the higher end of the photon energy range, and two-out-of-three ST sectors.

CHAPTER III

DETECTOR CALIBRATION AND PARTICLE IDENTIFICATION

Running conditions

The data analyzed in this thesis includes data from three different data runs. Of the three runs, *Run a* and *Run b* had identical geometrical acceptance and trigger requirements, while *Run c* had slightly different running conditions. *Runs a, b* and *c* had a tagged photon beam in the energy range of 3.2–3.95 GeV, 3–5.25 GeV, and 4.8–5.47 GeV, respectively. *Run c* (Experiment E01_017) was completed during the period from August 17th, 2001 to September 11th, 2001. Table 2 is the summary of the running conditions.

Table 2: Running conditions for g6a, g6b, and g6c

conditions	g6a	g6b	g6c
Electron beam energy(GeV)	4.0	5.6	5.744
Electron beam current(nA)	45	40-45	40/50
Converter radiation length	10^{-4}	10^{-4}	3×10^{-4}
tagged photon energy range(GeV)	3.2-3.95	3.0-5.25	4.8-5.47
Tagged photon flux	2×10^6	2×10^6	5×10^6
Target offset	0	0	-1m
Start counter	0	0	-0.85m
Torus magnet current	3375A	3375A	1938A
Sensitivity (pb^{-1})	2.0	2.0	2.7
Trigger	MOR(1-24)& ST(2/3)& 2 opposite tracks	same as g6a	MOR(1-12)& ST(2/3)& 2 tracks

Detector Calibration

Before the raw data is ready to be analyzed, the detectors need to be calibrated. There are three crucial calibration procedures involved with photon experiments: the Tagger Calibration [86, 87], the Drift Chamber calibration [88], and the time-of-flight Calibration [89]. The three are intertwined, therefore the entire procedure is iterated. The quality of the calibration met the standards as required [86, 87, 88, 89]. This a project for the entire collaboration, and my role focused on the calibration of the time-of-flight system.

Tagger Calibration

In photon experiments, the time of the beam photon is measured by the tagging system and then corrected for the phase difference between the tagger and the RF signal, which is the most accurate timing measurement in CLAS. The calibration procedures include: determination of the RF time, tagger TDC calibration, the TDC slope calibration, and the alignment of tagger time and RF time. The alignment between the tagger and CLAS is completed during the TOF calibrations. Fig. 41 shows that all T-counters are aligned with the RF time, noting that the experiment triggered on only the first 12 T-counters. Fig. 42 is the overall time difference distribution between the tagger time and the RF time. A Gaussian fit yields a resolution of 115 ps.

Time-of-flight Calibration

For each TDC, the raw data T is converted into a time, t, using:

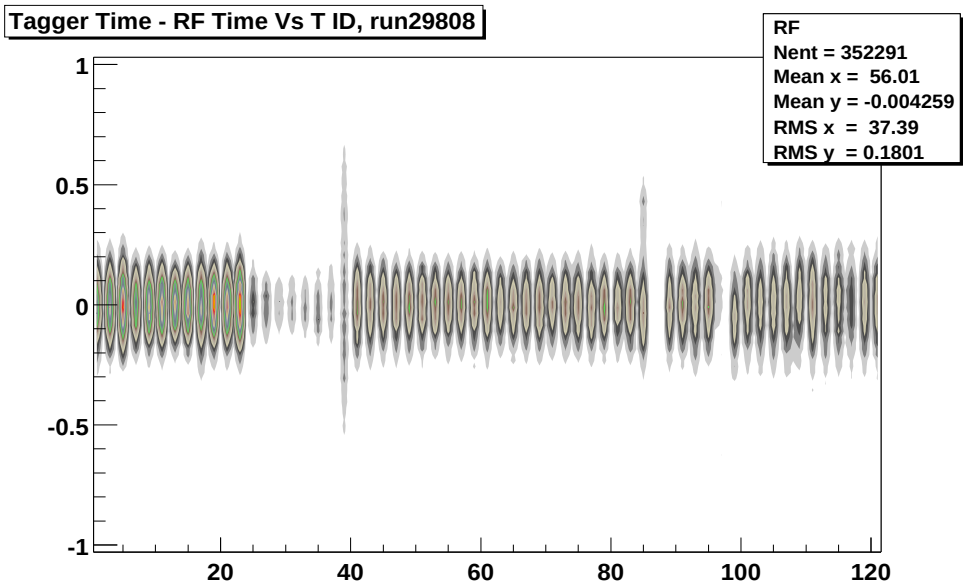

Figure 41: The $T_{TAGGER} - T_{RF}$ vs T counter id.

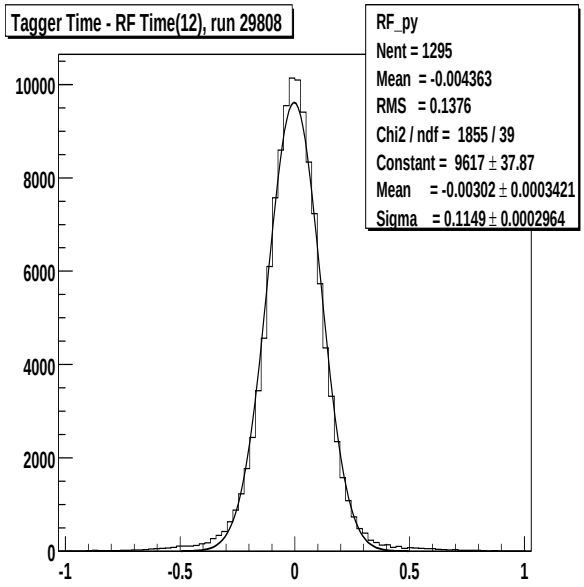

Figure 42: The projection on the y-axis of Fig. 41. The distribution is centered, and fitted with a Gaussian function. The fitting parameter σ shows the resolution of the tagger is 115 ps.

$$t = c_0 + c_1 T + c_2 T^2 + t_w \tag{15}$$

where c_0 is an overall offset, c_1 and c_2 are constants, and t_w is the time walk correction due to the pulse height. After these constants are obtained from calibration, the left and right PMTs need to be aligned. The averaged time of the two PMTs gives the time for that paddle:

$$T = \frac{T_L + T_R}{2} \tag{16}$$

In the case of only one TDC present, say the left, the time is calculated as

$$T = T_L - \frac{y}{v_L} \tag{17}$$

where y is the distance along the paddle to the PMT from the point where the particle entered the scintillator as determined from tracking.

Once the energy loss is calibrated, particles can be roughly identified from the energy loss as a function of particle momentum (Fig. 37), where the pions form the horizontal band. The energy loss of protons increases linearly at low momentum until they begin penetrating the scintillators, at which point the energy loss follows the Bethe-Bloch formula. Pions are minimal ionizing particles (MIP). For the most part, the momentum range and the energy deposition remain roughly constant. This can be used as an independent particle identification method before the timing is calibrated. Using the measured momentum, β, of the pions identified with this method can then be computed and used to align the TOF paddles with the tagger. The right plot in Fig. 43 shows the difference between the pion vertex time, which is calculated from

the time recorded by the TOF scintillator and extrapolated back to the event vertex using a β value obtained as discussed above, and the event vertex time as recorded by the tagger for all 288 TOF paddles. The overall resolution is about 210 ps. The start counter was also aligned with the TOF by shifting the time delay between the two detectors and comparing the vertex time difference between the vertex time recorded by each of the two (Fig. 43, left). The achieved resolution of start counter is about 490 ps, which is good enough to be used for the selection of photons that come every 2 ns.

Fig. 44 shows the scatter plot of vertex time differences vs the TOF paddle id for sector 4, of which all 48 paddles are aligned with the tagger, while paddles with id above 40, corresponding to large angle TOF counters, cannot be calibrated because of the acceptance. In experiment E01_017, the target was pulled upstream 1m resulting in the loss of tracking information, particularly in DC region 1, which is needed for the TOF calibration. However, the event would not be able to be reconstructed anyway without region 1 tracking information.

After all three detectors: start counter, tagger and time-of-flight system, are aligned in timing (Fig. 43), the mass of charged particles can be calculated from their time of flight (Fig. 45). The timing resolution achieved is about 160 ps for forward paddles and up to 250 ps for large angle paddles.

Drift chamber Calibration

To improve the track reconstruction, the drift chamber calibration is performed in iterations of running the reconstruction program followed by refitting the detector

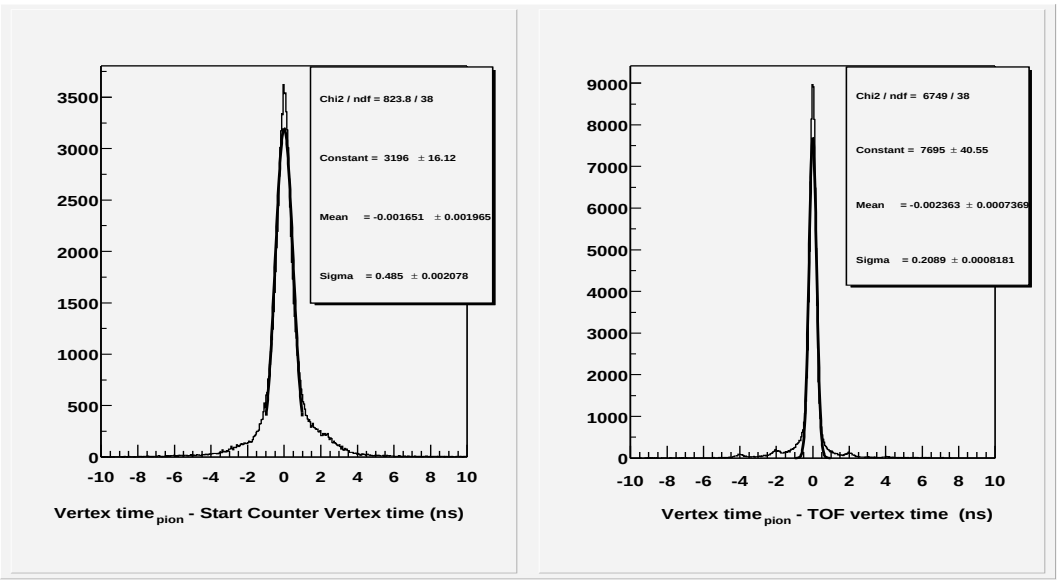

Figure 43: The quality of the Time-of-Flight calibration for experiment E01_017. Left: The timing difference between the pion vertex time calculated from the Time-of-Flight and the Start Counter for all paddles. Left: The timing difference between the pion vertex time calculated from the Time-of-Flight and the tagger, which has already been aligned with the RF time for all paddles.

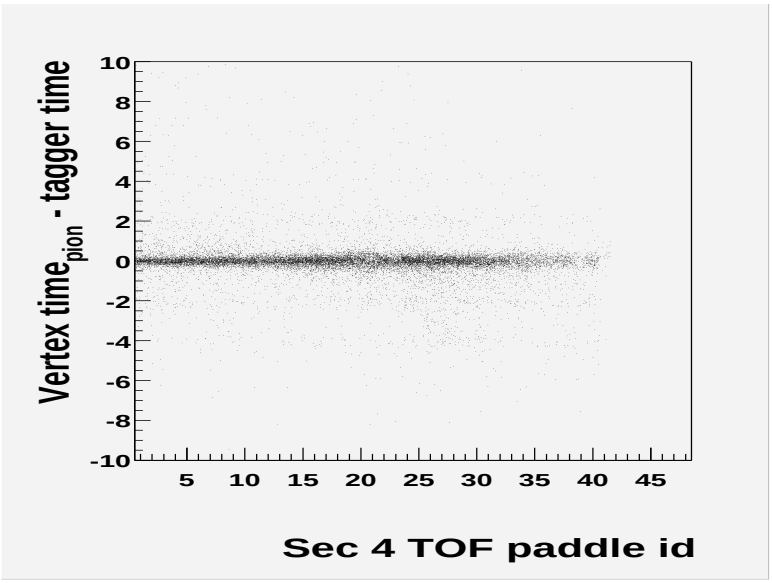

Figure 44: Vertex time difference vs TOF paddle id for sector 4. The depletion for paddles with id higher than 40 is due to the acceptance.

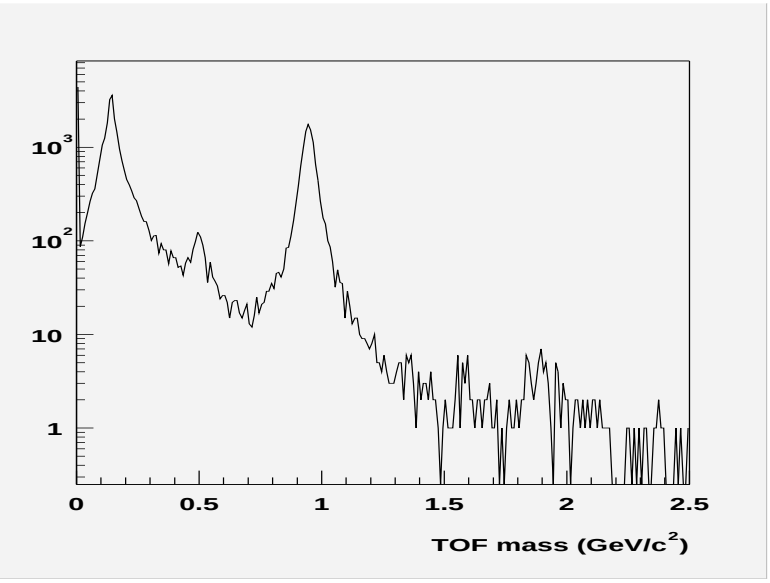

Figure 45: Time-of-flight mass for charged particles. The three main peaks are pion, kaon and proton.

calibration constants. The track reconstruction is completed in two stages. In the first stage, individual tracks are fit to the hit wire positions. The hists inside the superlayer are combined into track segments, which are then linked together to form tracks across all three drift chamber regions. Due to the relatively small size of the drift cells and large number of wire layers, the track momenta can be reconstructed with $3 - 5\%$ resoluction [76]. In the second stage, the time-of-flight information is used to correct the drift times, which are then converted to drift distances to correct the hit positions and determine the final track parameters.

As discussed in Chapter 2, the drift chambers at CLAS are composed of 6 sectors, each of which has an identical set of chambers. They are grouped into 3 regions, each containing 2 superlayers. Each superlayer contains 6 layers of sense wires (with the exception of superlayer 1 only having 4 layers). When a charged particle goes through the drift chambers, all 34 layers are hit. Each track has about 30 hits due

to the inefficiency or holes in the chambers' fiducial volume. Each hit detected in the chamber is used to determine the particle's track via a least squares fit done inside the CLAS reconstruction program. Two terms are used to describe the distance of a charged particle track from a sense wire:

DOCA - (Distance Of Closest Approach): The distance from the sense wire to the track as determined by tracking.

DIST - The predicted distance from the sense wire to the track. This is calculated from the drift time as well as some other parameters. The drift time is calculated from the wire's TDC values accounting for fixed cable delays and event-dependent delays such as flight time.

The term *residual* is used as the primary means of measuring the resolution of the drift chambers: $RESI = |DOCA| - |DIST|$.

A method called residual fitter was used to calibrate the drift chambers. It completes the calibration by minimizing the χ^2 as defined in Eq. 18.

$$\chi^2 = \sum_i^N \left(\frac{\overline{DOCA(t)} - [DIST(t, \vec{p}_f, \vec{\alpha}_{avg}) + (\overline{DIST(t, \vec{p}_m, \vec{\alpha})} - DIST(t, \vec{p}_m, \vec{\alpha}_{avg}))]}{ERR(t)}\right)^2 \tag{18}$$

where: $\vec{p}_f$ are the parameters varied in the fit, $\vec{p}_m$ are the previous parameters, $\vec{\alpha} = \beta, \vec{B}$, and $locangle$, and $\vec{\alpha}_{avg} = \beta_{avg}, \vec{B}_{avg}$, and $locangle_{avg}$. The two $DIST$ terms in the round brackets of the above equation is a correction to the first $DIST$ term. This accounts for the difference between evaluating a function at the averages of its input distributions and averaging over the distribution of a function. Generally, $\overline{DIST(t, \vec{p}_m, \vec{\alpha})} \neq DIST(t, \vec{p}_m, \vec{\alpha}_{avg})$.

The quality of the calibration is checked by the number of hits per track, and the average tracking χ^2 as defined in Eq. 18. Fig. 46 shows the fitted residuals vs drift time distribution. The residual is centered around zero across the whole range of drift times. On average 30.33 hits per track were achieved, and the average χ^2 value is 1.49, well below the required value of 3.0.

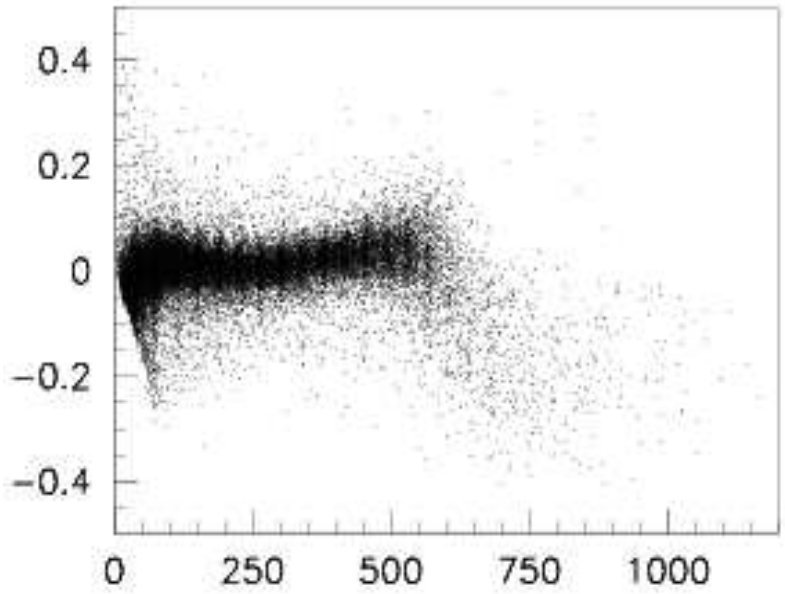

Figure 46: A sample distribution of the DC residuals (cm) vs drift time (ns).

Particle identification

Charged Particle identification

Once the detectors are calibrated, the particles can be identified from their timing. In CLAS, charged particles such as pions, protons and kaons are identified by the time-of-flight mass, which relied heavily on a precise measurement of drift chamber momentum and flight time from the target to the TOF counters. Fig. 47 is a plot of the relation between β and momentum (P) for all charged particles, which qualitatively

illustrates the PID in CLAS. Pions, protons and kaons form separate bands defined by:

$$p = \gamma\beta m \tag{19}$$

where

$$\beta = \frac{l}{c\Delta t} \tag{20}$$

where l is the path length from the event vertex to the TOF scintillator hit position, and Δt is the time of flight. Eq. 21 also gives the TOF mass which is used to identify different charged particles:

$$m = \sqrt{1-\beta^2}\frac{p}{\beta} \tag{21}$$

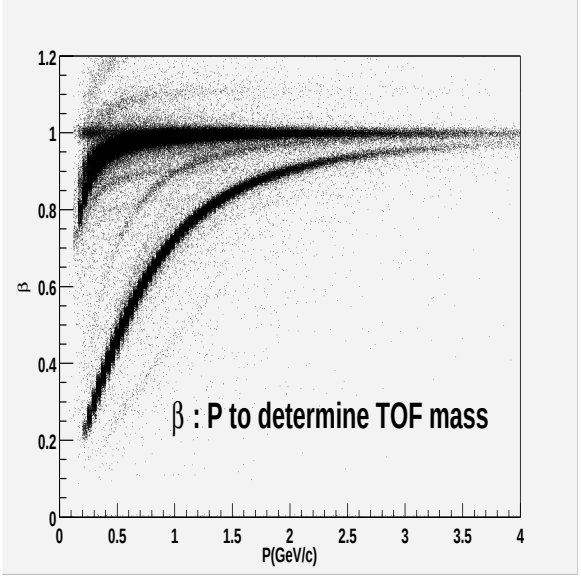

Figure 47: $\beta : P$ for all charged particles detected by CLAS for a typical high intensity photon experiment. The crossing bands correspond to particles that are identified with the wrong photons which were of multiple time bucket away from the correct photons.

Charged particles are then identified in the event reconstruction stage by:

1. pions: m<0.3 GeV/c^2,

2. kaons: 0.35< m < 0.65 GeV/c^2,

3. protons: 0.8< m < 1.2 GeV/c^2,

4. deuterons: 1.75< m < 2.2 GeV/c^2,

However, such standard PID procedure does not address the two following problems, particularly for kaon identification. First, the TOF resolution deteriorates when the momentum of the particles increases. This means a simple universal mass cut of 0.35GeV $< m <$ 0.65GeV for of kaons of all momentum is not enough. Above 2 GeV, kaons and pions become more or less inseparable. Second, the contamination from particles with wrong RF time buckets. As mentioned before, when running at a photon flux as high as 5×10^6/sec as in *Run c*, there is a high probability that there are more than one photon that has time close to the event start time (12% of the time, there are two photons from one beam bucket). During the calibration runs, when the beam current is only 5 na, the possibility of choosing the wrong photon is rather low. However, when the beam current increases, out of time photons lead to a bigger contamination. In Fig. 47 it can seen that pions with +- 2M ns (M=1, 2, 3...) wrong time bucket fall to the side bands and intersect with the kaon bands. It is important to note that such out of time photons are a particular concern for kaon identification because many more pions are being produced than kaons. Protons also have side bands, which however are less visible. To clean up this background, one needs select the good events by requiring the vertex time according to the photon selected for this event to fall within 1 ns around the vertex time obtained by the

starter counter.

Electron and neutral particle identification

In CLAS, neutral particles include photons and neutrons. Neutrals are called neutrons if the β of such a particle is below 0.9. The β cut of 0.9 is applied for neutron-γ separation. For neutrons, the momentum is obtained from the timing result. However, the neutron momentum has a large uncertainty and therefore it is usually better to reconstruct the neutron four vector through missing mass technique if all the other final state particles are charged. The electrons are identified from the Čerenkov Counter and the EC. They consist of small backgrounds in this analysis, therefore need not be elaborated on.

CHAPTER IV

DATA ANALYSIS

Overview

In this chapter, the analysis of the reaction of $\gamma p \to \pi^+ K^- K^+ n$ will be presented. The data analyzed here are from three data sets:*Run a, b* and *Run c*. Of the three runs, *Run a* and *Run b* had identical geometrical acceptance and trigger requirements, with *Run c* having slightly different conditions. *Runs a, b* and *c* had a tagged photon beam in the energy range of 3.2–3.95 GeV, 3–5.25 GeV, and 4.8–5.47 GeV, respectively. *Runs a* and *b* had the hydrogen target in the standard position at the CLAS center, but in *Run c* the target was moved upstream by 1 meter to improve the acceptance in the forward direction, especially for the negative charged particles. The estimated integrated luminosity for the combined data set of *Runs a* and *b* is 2 events/pb, and *Run c* is 2.7 events/pb. The analysis of the data set of the *Run c* (Experiment E01_017) will be reviewed in detail, and later it will be combined with the other two data sets at lower energy to obtain final results. The analysis of *Run c* was carried out by me as well as the partial wave analysis (PWA) of the three-body meson system in the same final state.

Event selection

In the final state $nK^+K^-\pi^+$, all three charged particles were detected by CLAS, and the neutron is reconstructed from missing mass. Fig. 48 shows the missing mass

spectrum off of $K^+K^-\pi^+$. The missing mass peaks at 0.938 GeV with a σ of 22 MeV and is sitting on a background that is estimated to be around 21%. (Depending on the neutron cut: the background is 25% if this cut is loosened to 3σ). Most of the background is believed to be coming from pions that are misidentified as kaons as well as other reactions that include more final state particles. In CLAS, charged particles are identified using the time-of-flight mass. Fig. 51 shows the β vs momentum scatter plot for this final state. The kaon band is well separated from the pion band. The vertex time difference for pions as calulated from the TOF and the TAGGER, shown in Fig. 52, shows peaks that are 2 ns apart. The highest peak centered around zero is from the events that have correct photon times, while the other peaks at $2M$ ns, with $M = \pm 1, \pm 2, ...$, are from events that have the wrong photon time buckets that come every 2.004 ns. A cut on the vertex time difference between the start counter record (sc_vtime) and the tagger vertex time(sc_vtime) to be within 1 ns is imposed to insure that good photons are identified with the event. In addition to the timing requirement, the cut on the missing mass to be around neutron mass also provides addditional kinematic constraint which leads to good kaon identification. The usual crossing bands into kaons ,which is common when an out-of-time photon is chosen, are not visible. In fact, even the β vs Momentum scatter plot (Fig. 53) for the neutron side bands (illustrated in Fig. 49) does not show many events that have incorrect photons.

To test whether the kaons are really kaons instead of misidentified pions, the missing mass of the three detected charged particles can be calculated by assigning a pion mass to the two kaons, while retaining the measured momentum. As shown in

Fig. 50, the hypothetical missing mass off $\pi^+\pi^+\pi^-$ vs the missing mass off $K^+\pi^+K^-$ illustrates the possible background from the reaction $\gamma p \to \pi^+\pi^-\pi^+ n$ would not be present once the missing neutron events are selected due to the phase space constraint. The background under the neutron peak is most likely due to reactions such as $\gamma p \to \pi^+ K^- K^+ \pi^0 n$ or $\gamma p \to \pi^+\pi^-\pi^+\pi^0 n$. It is also worth pointing out that in CLAS, kaon identification is good up to 2 GeV, and it becomes impossible to separate kaons from pions when the momentum is above 2 GeV. Since there are two kaons in the final state, typically at least one kaon would have low momentum which leads to good particle identification and the other kaon would have a better chance of good particle identification due to strangeness conservation. Events that are associated with the $\phi(1020)$ production are removed by requiring the invariant mass of K^+K^- system to be higher than 1.06 GeV/c^2 (Fig. 55). Because of the acceptance, this is not a large background. In *Run c*, the target was moved upstream. The $\phi(1020)$, which is produced in association with Δ's or N^*'s with low momentum transfer, retains most of the beam momentum, about 5 GeV. Therefore it goes straight through the beam line where the acceptance is very low. In addition, energy loss in the target and start counter region were taken into account. A beam energy shift of +0.086% was also applied to correct the neutron missing mass peak to its nominal position.

In Table 3, the general cuts used at the event selection stage are listed. The first three cuts are applied to insure that the reaction took place in the hydrogen target. Fig. 54 shows the reconstructed vertex position after the target cut. The missing mass constraint (around the neutron) effectively eliminates the background from pions misidentified as kaons.

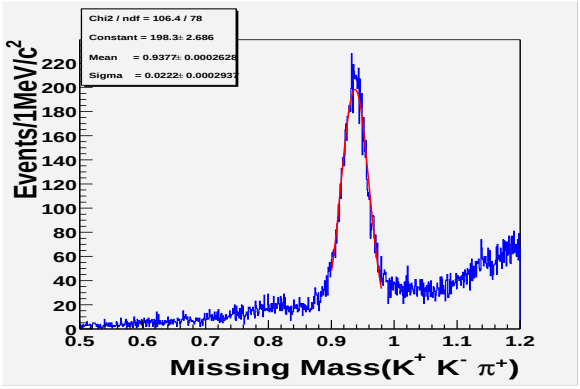

Figure 48: Missing mass off of $K^+K^-\pi^+$

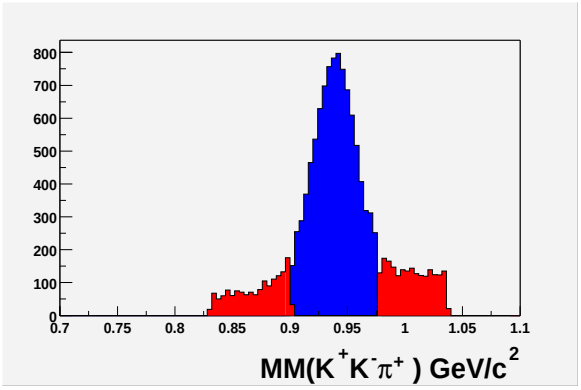

Figure 49: Missing mass off of $K^+K^-\pi^+$. The blue shaded region shows the cut for event selection (2σ around the peak), the red side bands are for background study (2-5 σ)

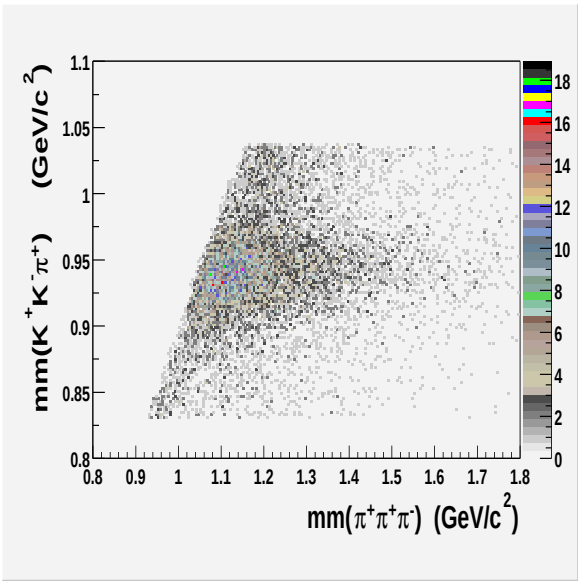

Figure 50: Missing mass squared off of $\pi^+\pi^-\pi^+$ (by assigning the detected kaons with pion PDG mass while retaining the measured momentum) vs Missing mass squared off of $K^+K^-\pi^+$.

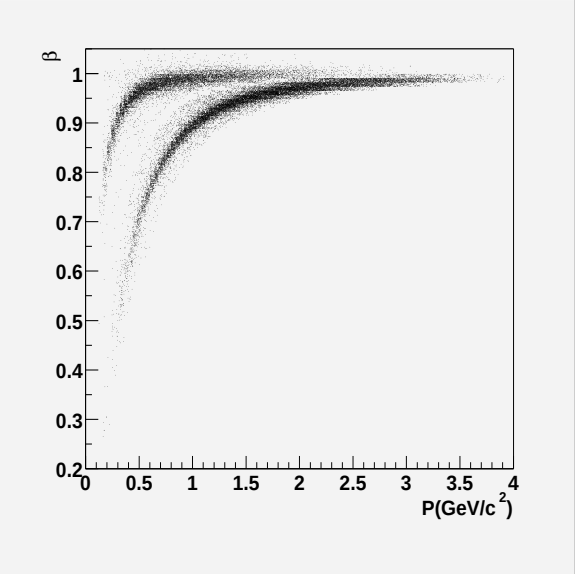

Figure 51: $\beta : p$ for all three charged particles: $K^+K^-\pi^+$, while selecting the neutron events.

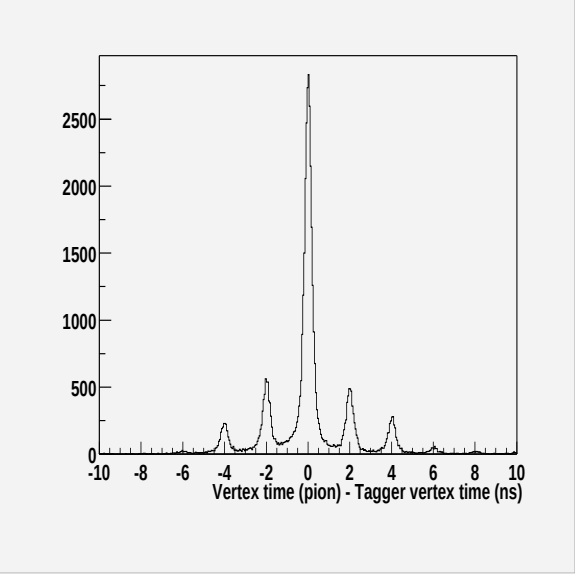

Figure 52: Vertex time difference between start counter vertex time and tagger vertex time for 40 na data showing wrong photons causing peaks at $2.004 \times M$ ns, $M = \pm 1, \pm 2, ...$

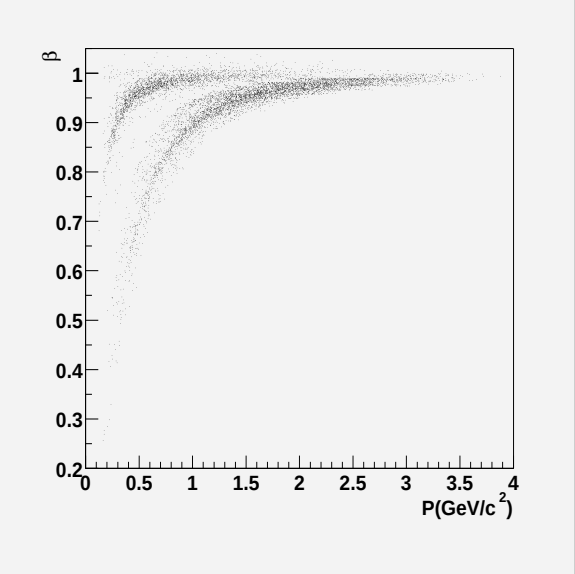

Figure 53: $\beta : p$ for all three charged particles:$K^+K^-\pi^+$, selecting events that fall to the side bands around the neutron in Fig. 48.

Table 3: Event selection for $\gamma p \rightarrow nK^+K^-\pi^+$ reaction. For the Θ^+ analysis, no $|t'(\gamma \rightarrow K^+K^-\pi^+)|$ cut or π^+ lab angle was imposed, and the data set of 9519 events was analyzed

Selection Criteria	**Cuts applied**	Events Survived
Photon energy	$E_\gamma > 4.8$**GeV**	
Vertex Position	$(V_x^2 + V_y^2) < 4cm^2$ V_z within target length	
Vertex time	$\lvert sc\_vtime - st\_vtime\rvert < 1ns$	57,739
$MM^2(K^+K^-\pi^+)$	$\lvert MM(K^+K^-\pi^+) - 0.9389\rvert \leq 3 \times \sigma$	11,466
$MM^2(K^+K^-\pi^+)$	$\lvert MM(K^+K^-\pi^+) - 0.9389\rvert \leq 2 \times \sigma$	10,018
$M(K^+K^-)$	≥ 1.06 GeV/c^2	9,519

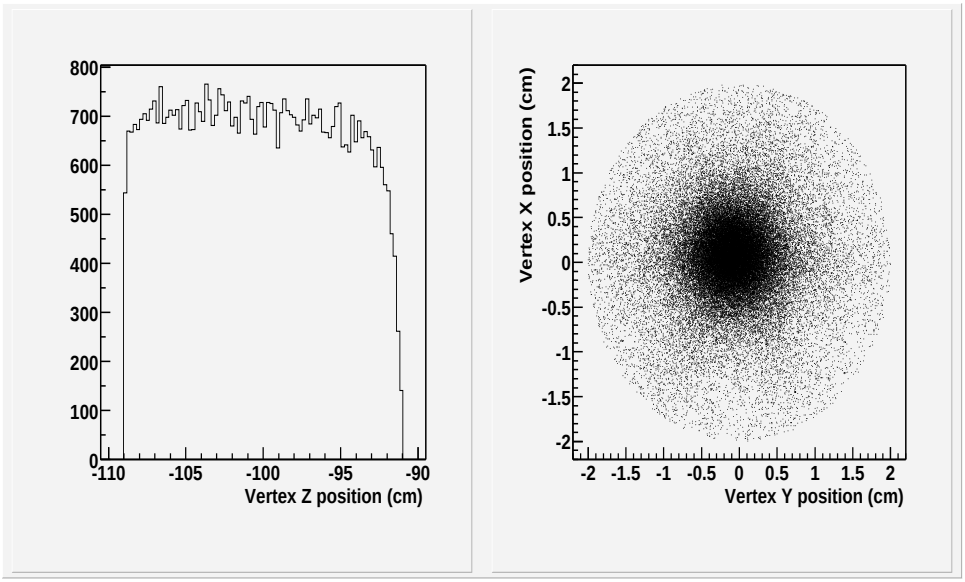

Figure 54: The reconstructed vertex position. The edges illustrate the cuts applied for vertex position.

Background processes for Θ^+ production

The reaction $\gamma p \rightarrow nK^+K^-\pi^+$ is dominated by t-channel meson production (Fig. 56*a*)), with considerable background from baryons such as the $\Delta(1232)$ (Fig. 56*b*)). To extract any possible Θ^+ signal, the 3-body meson background and the $\Delta(1232)/N^*$ background need to be maximumly reduced. Background from hyperons which decay to $n\bar{K}^{*0}$ is considered to be small largely due to the energy of this experiment.

Three-body meson background

As stated previously, the reaction $\gamma p \rightarrow nK^+K^-\pi^+$ has a dominant 3-body mesonic background resulting from mesons being produced through t-channel process at the meson vertex (Fig. 56*a*)) and then sequentially decaying to $K^+\bar{K}^{*0}$ or

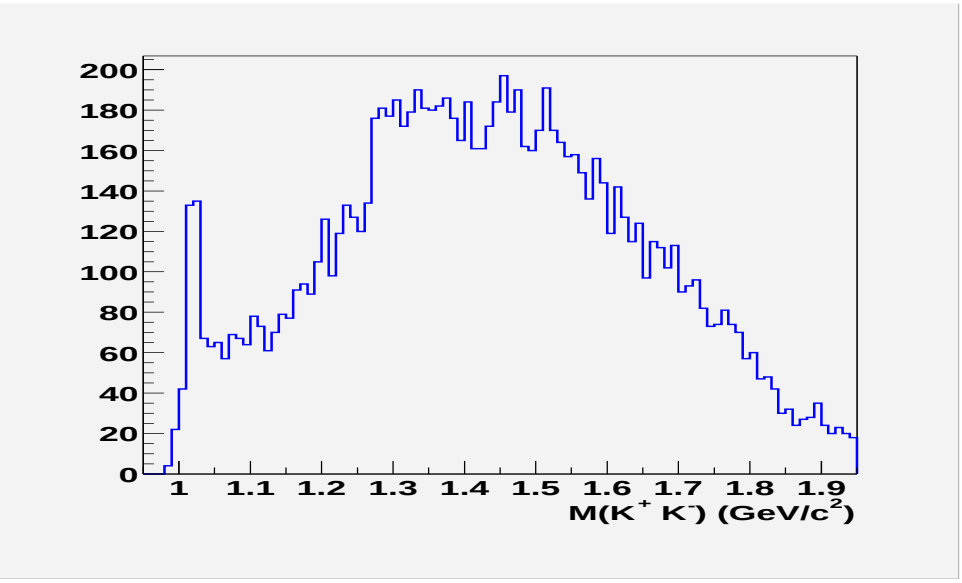

Figure 55: Invariant mass spectrum of (K^+K^-) system showing the $\phi(1020)$ signal.

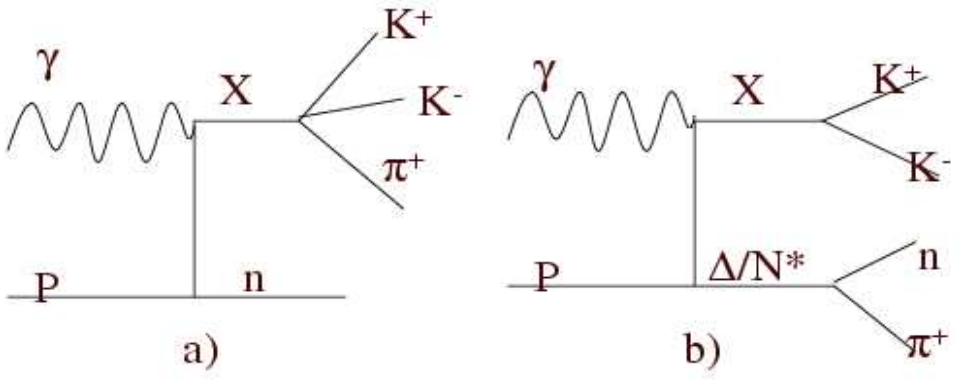

Figure 56: Feynman diagrams for the background in Θ^+ photo-production through $\gamma p \to nK^+K^-\pi^+$ reaction off a proton target. a) a meson X^+ being produced at top vertex with sequential decay to either $K^+\bar{K}^{*0}$ or $(K^+K^-)\pi^+$, b) a Δ or N^* being produced at the baryon vertex decaying to $n\pi^+$.

$(K^-K^+)\pi^+$. The invariant mass spectrum of $K^-\pi^+$ has a prominent signal of $\bar{K}^{*0}$ (Fig. 57) which peaks at 895.5 MeV/c^2 (PDG value for $\bar{K}^{*0}$ is 896.1 MeV), while most of the $\bar{K}^{*0}$ are presumably coming from a meson decay. Possible mesons that can decay to $(K\bar{K}\pi)^+$ are listed in Table 4.

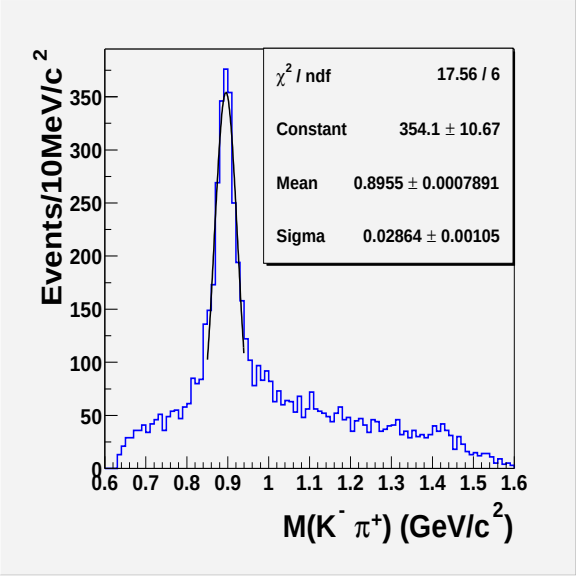

Figure 57: Invariant mass spectrum of $K^-\pi^+$ system, with no $|t'(\gamma \to K^+K^-\pi^+)|$ cut

Table 4: Possible Decay Modes for $X^+ \to (K\bar{K}\pi^+)$, where **L** is the orbital angular momentum of the decay

I^G	J^{PC}	X^+	**Decay Mode**	**L of decay**
1^+	1^{--}	$\rho(1700)$	$K^*(892)K$	1
1^-	2^{-+}	$\pi(1670)$	$K^*(892)K$	1
1^-	2^{-+}	$\pi(1670)$	$f_2(1270)\pi$	2
1^-	0^{-+}	$\pi(1800)$	$K^*(892)K$	1
1^-	0^{-+}	$\pi_2(1800)$	$K^*(892)\bar{K}$	1
1^-	0^{-+}	$\pi_2(1800)$	$f_0(980)\pi$	0
1^+	3^{--}	$\rho(1690)$	$a_2(1320)\pi$	2
1^+	3^{--}	$\rho(1690)$	$K^*(892)K$	3

To search for the Θ^+, the biggest challenge is to suppress the meson background that dominates the data. The scatter plot (Fig. 58, left) of $M(K^-\pi^+)$ vs $M(K^+K^-\pi^+)$

shows that meson production and a $(K^-\pi^+)$ effective mass around the $\bar{K}^{*0}(892)$ region are correlated. The lower peak around 1.7 GeV/c^2 should be due to the production of $\pi_2(1670), \rho_3(1690)$, or $\rho(1700)$, while the higher peak around 1.9 GeV/c^2 corresponds possibly to the $\pi_2(1800)$, or $\pi(1800)$ production. This background can be suppressed by using a kinematic constraint. As shown nn Fig. 59, the mesons that decay to $K^+K^-\pi^+$ are mostly correlated to K^+ going forward in the center-of-mass system. Also shown in Fig. 60, it is possible to suppress the 3-body mesonic background by removing K^+'s which are forward in the center-of-mass (CM) frame [1].

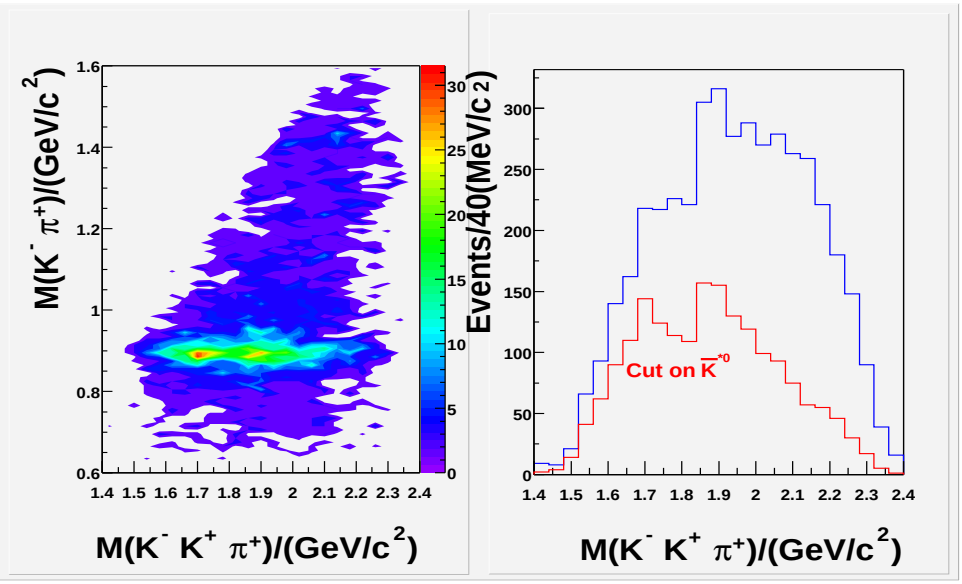

Figure 58: Left: Scatter plot of $M(K^-\pi^+)$ vs $M(K^+K^-\pi^+)$, both plots has a cut on $|t'| \leq 0.6$ $(\text{GeV}/c^2)^2$. Right: $K^+K^-\pi^+$ Mass spectra with $\bar{K}^{*0}(892)$ cut (Red, using $|M(K^-\pi^+) - 0.895| < 2 * 0.031$ GeV/c^2) and without (Blue)

Other baryon background

In the reaction $\gamma p \to \pi^+K^-K^+n$, a baryon resonance such as the $\Delta(1232)$ or other N^*'s can be produced in pairs with a meson system decaying into K^+K^- (Fig. 56*b*).

[1] The center-of-mass frame is defined as the rest frame of the beam-target system. The z axis is defined by the photon beam direction.

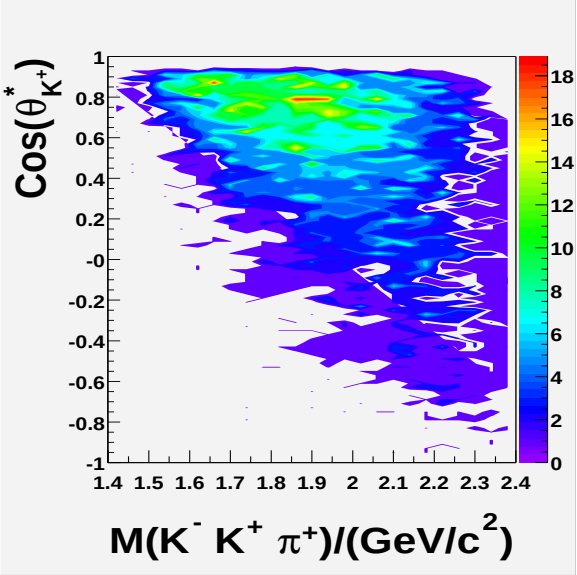

Figure 59: Scatter plot of $cos(\theta^*_{K^+})$ vs $M(K^+K^-\pi^+)$, selecting $|t'| \leq 0.6$ (GeV/c^2)^2 events.

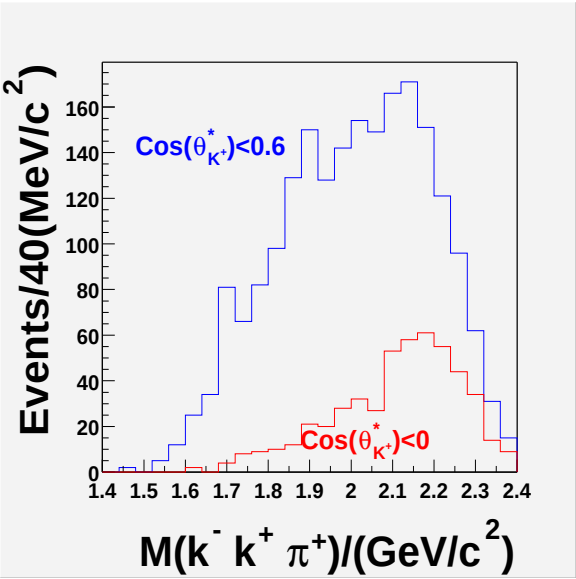

Figure 60: Blue: $(K^+K^-\pi^+)$ invariant mass spectrum, selecting backward going K^+ in the CM system with $cos(\theta^*_{K^+}) < 0.6$. Red: $(K^+K^-\pi^+)$ invariant mass spectrum, selecting backward going K^+ in the CM system with $cos(\theta^*_{K^+}) < 0$. Both required $|t'| \leq 0.6$ (GeV/c^2)^2 events (see chapter 5 for the definition of t').

In such processes, the π^+, a decay product of the baryon resonance, is expected to have a large possibility to have enough momentum kick to go backward in the CM system. This is confirmed by Fig. 61, which shows a clear $\Delta(1232)$ peak in the $n\pi^+$ invariant mass spectrum when the π^+'s going in the backward direction in the CM system ($cos(\theta^*_{\pi^+}) < 0$) are selected. Other possible baryon resonances ,such as the $N^*(1650)$, are also visible. There is no easy way to clearly eliminate such backgrounds. However, as will be discussed in the following section, it can be greatly reduced when a π^+ forward in the CM system is required when the possibility of producing Θ^+ as a decay product of a heavier nucleon is probed.

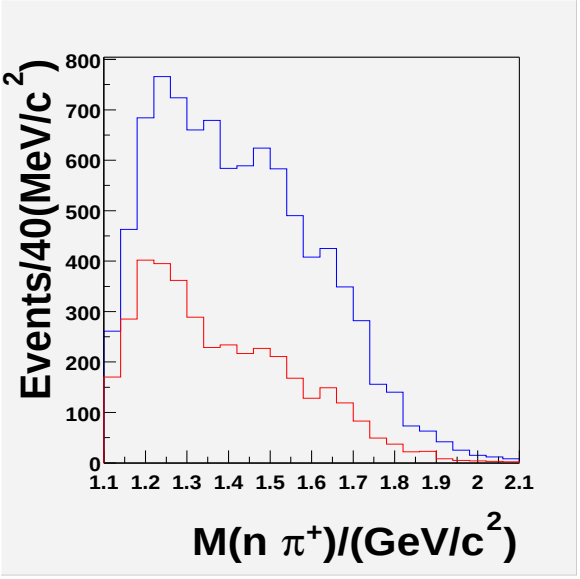

Figure 61: Blue: ($n\pi^+$) invariant mass spectrum, without cuts on π^+ angle. Red: ($n\pi^+$) invariant mass spectrum, selecting backward going π^+ in the CM system with $cos(\theta^*_{\pi^+}) < 0$.

Probing different Θ^+ production mechanisms

As previously discussed in Chapter 1, there are a number of ways to produce the Θ^+ off of a proton target in photon experiments. In particular, the reaction

of $\gamma p \to \pi^+ K^- K^+ n$ can contribute to Θ^+ production in two ways, as discussed in Chapter 1.

Producing the Θ^+ in correlation with $\bar{K}^{*0}$

It has been argued that the Θ^+ can be produced off a proton target in a photon experiment in association with a $\bar{K}^{*0}$ (Fig. 17) [64]. One can check this by selecting $\bar{K}^{*0}$ events and looking at the nK^+ invariant mass spectrum as shown in the left plot of Fig. 62. There is no clear signal at all. The right plot in Fig. 62 is the nK^+ invariant mass spectrum for non-$\bar{K}^{*0}$ events. Of course, as seen in Fig. 58, the $\bar{K}^{*0}$ is presumably associated with 3-body meson production. This background can be reduced by selecting the K^+ backward in the CM frame. The result is show in Fig. 63. There is no clear signal of possible Θ^+ production in the region where the state has been reported [50, 51, 55, 54] when $\bar{K}^{*0}$ is required.

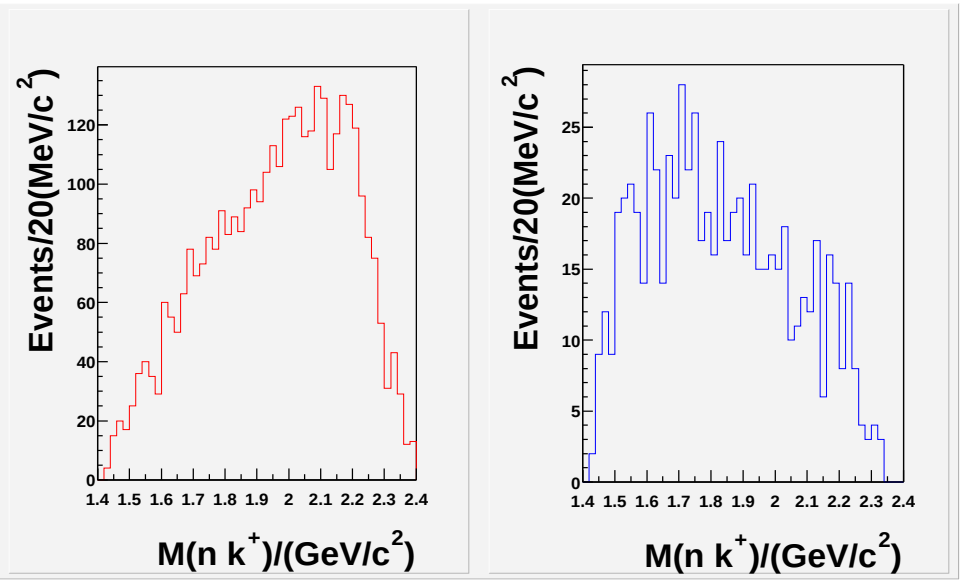

Figure 62: Left: (nK^+) invariant mass spectrum, selecting $\bar{K}^{*0}$ events (0.837GeV/c^2 < $((K^-\pi^+))$ <0.957GeV/c^2). Red: (nK^+) invariant mass spectrum, selecting non-$\bar{K}^{*0}$ events.

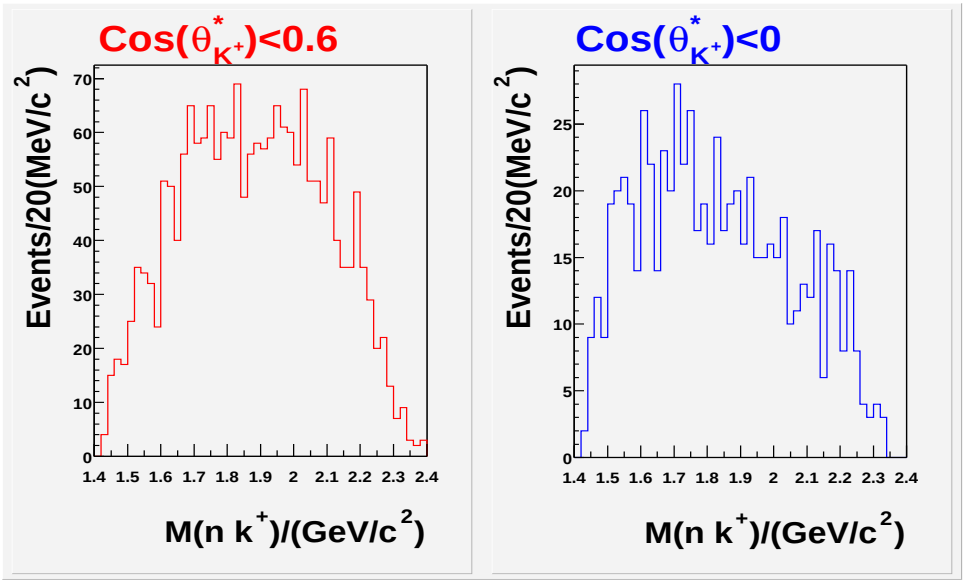

Figure 63: Left: (nK^+) invariant mass spectrum, selecting backward going K^+ in the CM system with $cos(\theta^*_{K^+}) < 0.6$. Right: (nK^+) invariant mass spectrum, selecting backward going K^+ in the CM system with $cos(\theta^*_{K^+}) < 0$. Both selected events around the $\bar{K}^{*0}$ peak.

Producing Θ^+ through an intermediate resonance

The other possible way to produce the Θ^+ is through an intermediate resonance as discussed in Chapter 1 and Ref. [70]. As shown in the Feynman diagram (Fig. 25), it is possible to produce a Θ^+ through the decay of an intermediate resonance such as the Δ or an N^* into a Θ^+ and a K^-, with a π^+ at the meson vertex. The signature of such a process would be low momentum transfer between the beam and the pion, which will presumably travel forward near the beam direction. This process is investigated by selecting pions forward in the CM system, requiring $cos(\theta^*_{\pi^+}) > 0.8$, which corresponds to low momentum transferr from the beam to the pion (roughly $|t'(\gamma \to \pi^+)| < 0.3$ GeV^2/c^4). In Fig. 64, a narrow signal in the mass region around 1.55 GeV/c^2 is evident in both plots which require also a K^+ backward in the CM system.

While removing events with a kaon forward in the CM system can suppress the

3-body meson background, the additional background from Δ and N^* produced in association with the production of mesons decaying to K^+K^- is reduced when a constraint on the π^+ angle in the CM system is applied. This can be seen in Fig.65. The signal for $\Delta(1232)$ and other possible N^* resonances almost completely disappears once a forward going π^+ is required. This should be no surprise since a π^+ coming from a $\Delta(1232)$ or N^*'s decays most likely in the backward direction in the CM system.

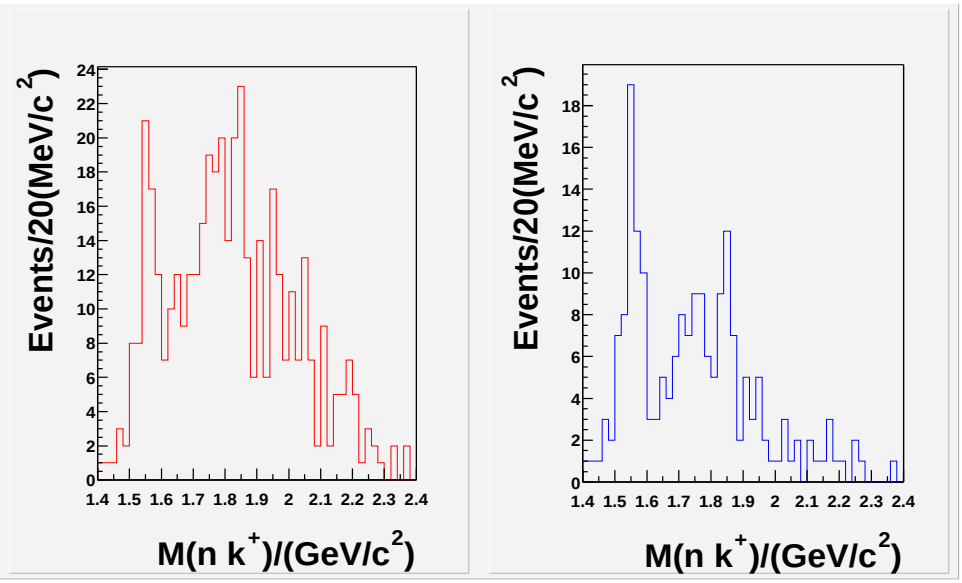

Figure 64: Left: (nK^+) invariant mass spectrum, selecting backward going K^+ in the CM system with $cos(\theta^*_{K+}) < 0.6$. Right: (nK^+) invariant mass spectrum, selecting backward going K^+ in the CM system with $cos(\theta^*_{K+}) < 0$. Both have events with forward going π^+ in the CM system: $cos(\theta^*_{\pi+}) > 0.8$

The fact that the angular cuts applied enhanced the Θ^+ signal suggests the possible production of an N^* or Δ^* that decays to a Θ^+ and a K^-. This can be readily checked by looking at the invariant mass spectrum of the nK^+K^- for the events near the possible narrow resonance seen in Fig. 64. A mass enhancement around 2.4 GeV/c^2 in the nK^+K^- invariant mass spectrum (Fig. 66) can be observed when the

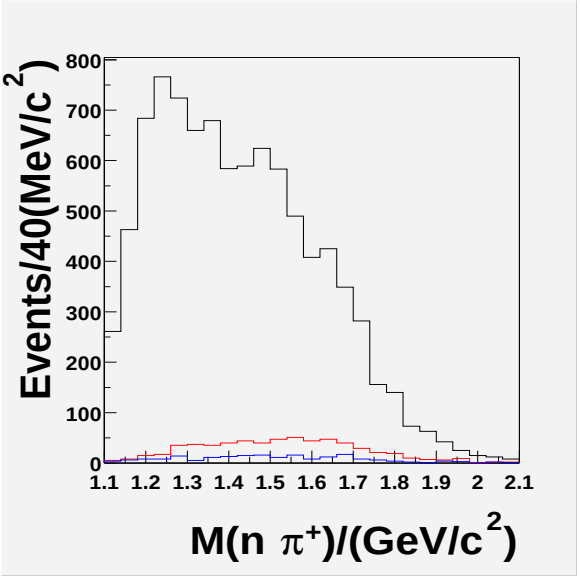

Figure 65: Black: $(n\pi^+)$ invariant mass spectrum, without cuts on π^+ angle or K^+ angle. Red: $(n\pi^+)$ invariant mass spectrum, selecting forward going π^+ in the CM system with $cos(\theta^*_{\pi^+}) > 0.8$. Blue:$(n\pi^+)$ invariant mass spectrum, selecting forward going π^+ in the CM system with $cos(\theta^*_{\pi^+}) > 0.8$ and $cos(\theta^*_{K^+}) < 0$

possible Θ^+ events($1.52 < M(nK^+) < 1.6$ GeV/c^2) are selected. However, the signal is small and a definite statement cannot be made. The relation between the possible Θ^+ signal with a possible heavy nucleon can be checked by cutting around 2.4 GeV/c^2 and plotting the corresponding nK^+ invariant mass spectrum. The results as shown in Fig. 67 is suggestive of such a correlation. However, a definite conclusion is prevented by the limit of statistics.

The peak around 1.55 GeV/c^2 is robust when the cuts are varied. For example, after relaxing the π^+ CM system angle cut from $cos\theta^*_{\pi^+} > 0.8$ to $cos\theta^*_{\pi^+} > 0.5$, or replacing it with a $|t'(\gamma \to \pi^+)| < 1$GeV/c^2 cut, the peak remains. Furthermore, when the method of calculating the nK^+ invariant mass is changed from using the missing mass of the $K^-\pi^+$ system to using the constrained neutron four vector with its mass set to the nominal value of 0.9396 GeV/c^2 and its three momentum measured

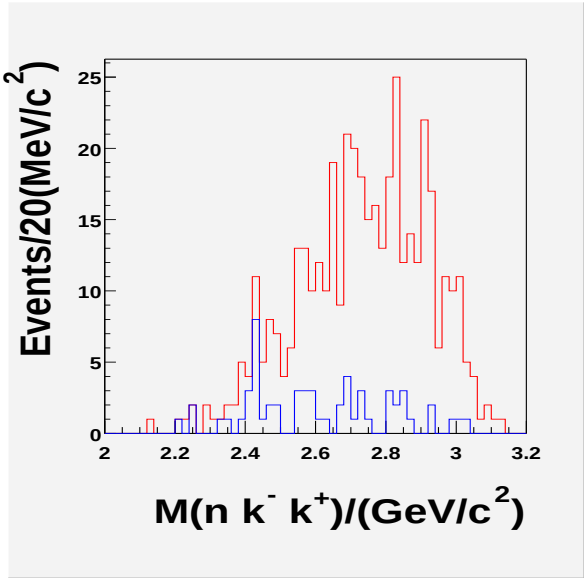

Figure 66: Red: (nK^+K^-) invariant mass spectrum, cutting on π^+ angle or K^+ angle with $cos(\theta^*_{\pi^+}) > 0.8$ and $cos(\theta^*_{K^+}) < 0.6$and . Blue: (nK^+K^-) invariant mass spectrum selecting the Θ^+ region with $1.52 < M(nK^+) < 1.6$ GeV/c^2

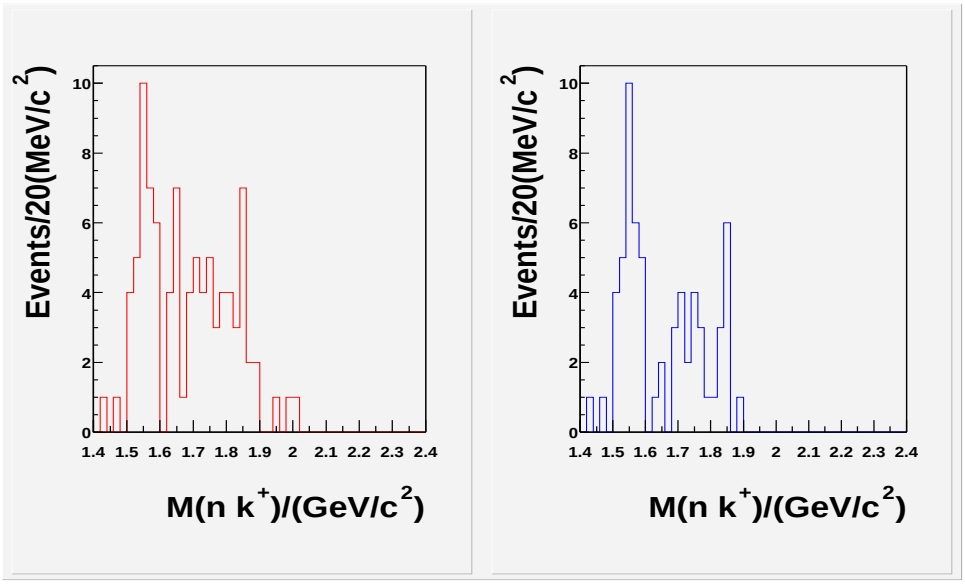

Figure 67: (nK^+) invariant mass spectra selecting $2.3 < M(nK^+K^-) < 2.6$GeV/c^2. Left Red:Selecting events with $cos(\theta^*_{\pi^+}) > 0.8$ and $cos(\theta^*_{K^+}) < 0.6$. Right Blue: Selecting events with $cos(\theta^*_{\pi^+}) > 0.8$ and $cos(\theta^*_{K^+}) < 0$.

from the missing momentum, the peak also did not disappear. However, the peak did become slightly wider (Fig. 69), which could be a result of the shifted neutron mass for those events that passed the kinematic constraint. In Fig. 48, the fitted missing mass peak is within 1 MeV to the nominal value of neutron mass in PDG(0.9396 GeV/c^2). However, the peak shifts about 4 MeV/c^2 higher (Fig. 70) for those events that survive the angular cuts used to extract the Θ^+ signal. For this reason, the neutron mass is not used to constrain the neutron four vector to calculate the invariant mass of the nK^+ system. Instead, the missing mass technique is used, i.e., the invariant mass of the nK^+ system is equal to the missing mass off the $K^-\pi^+$ system in the reaction of $\gamma p \to K^-\pi^+ X$.

Side band study

The side band events, shown in Fig. 49 with the missing mass of the $K^+K^-\pi^+$ system between 2 to 5 σ (σ = 19 MeV/c^2 is obtained from the Gaussian fit), are selected to study the corresponding nK^+ invariant mass distribution. The results are shown in Fig. 71 and can be compared with Fig. 64. There is no narrow resonance signal that can be seen in the nK^+ invariant mass spectra when same angular cuts are applied to these neutron side band events. The distribution for these events peak around 1.8 GeV/c^2, which is similar to what was observed in Fig. 64 away from the possible peak. As shown in the right plot of Fig. 72, the nK^+ invariant mass distribution peak around 1.55 GeV/c^2 becomes more prominent after the side band events are subtracted.

The background from pions misidentified as kaons can be further examined by

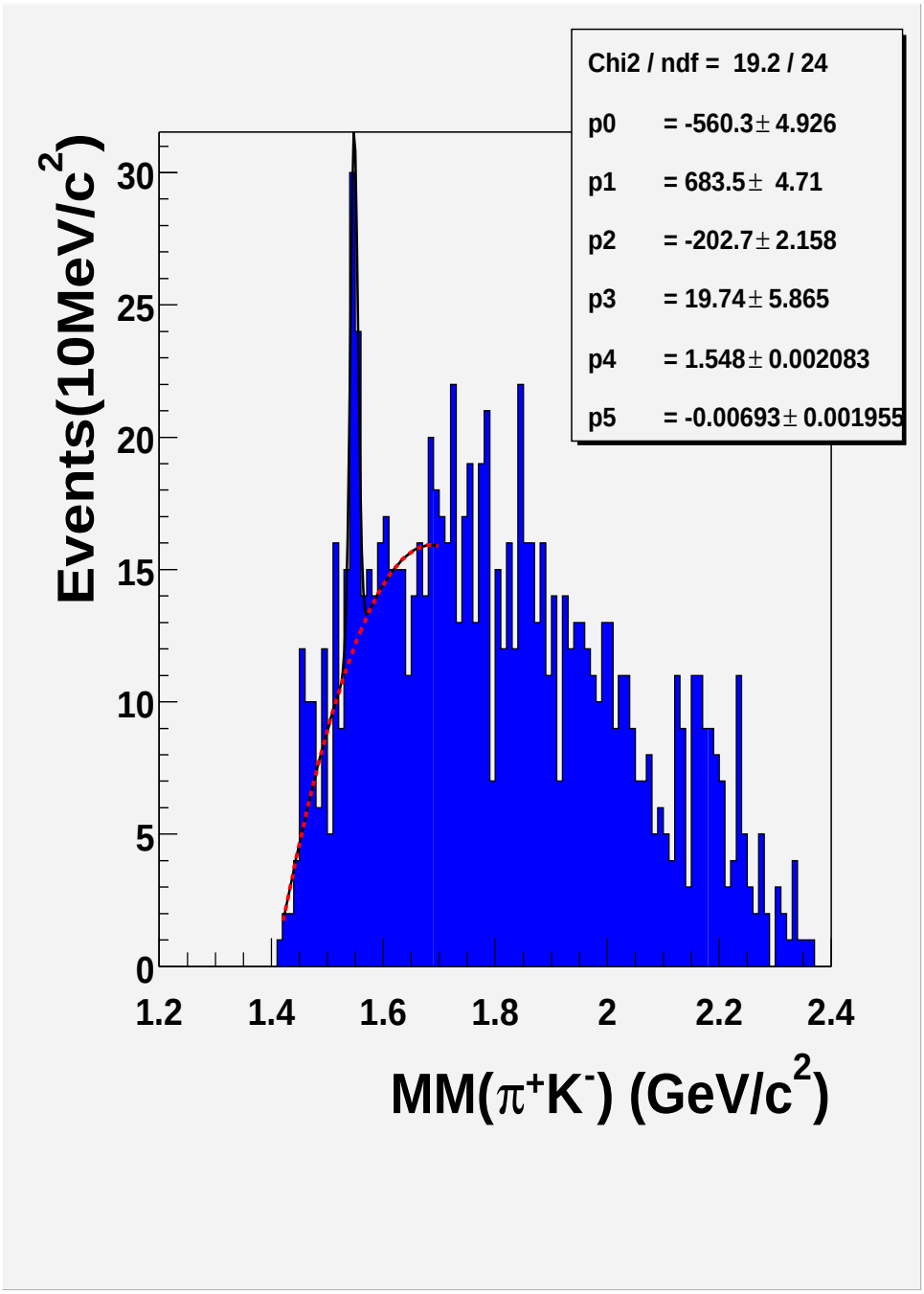

Figure 68: The nK^+ invariant mass spectrum calculated using the missing mass of the $K^-\pi^+$ system.Left panels have angular cut of $cos\theta^*_{K^+} < -0.08$ and $|t'(\gamma \to \pi^+)| < 1\mathrm{GeV/c^2}$ cut. The histogram was fitted using a function of a sum of Gaussian function and a second order polynomial. It gives a peak at 1.548 $\mathrm{GeV/c^2}$ with $\sigma = 6.9$ $\mathrm{MeV/c^2}$.

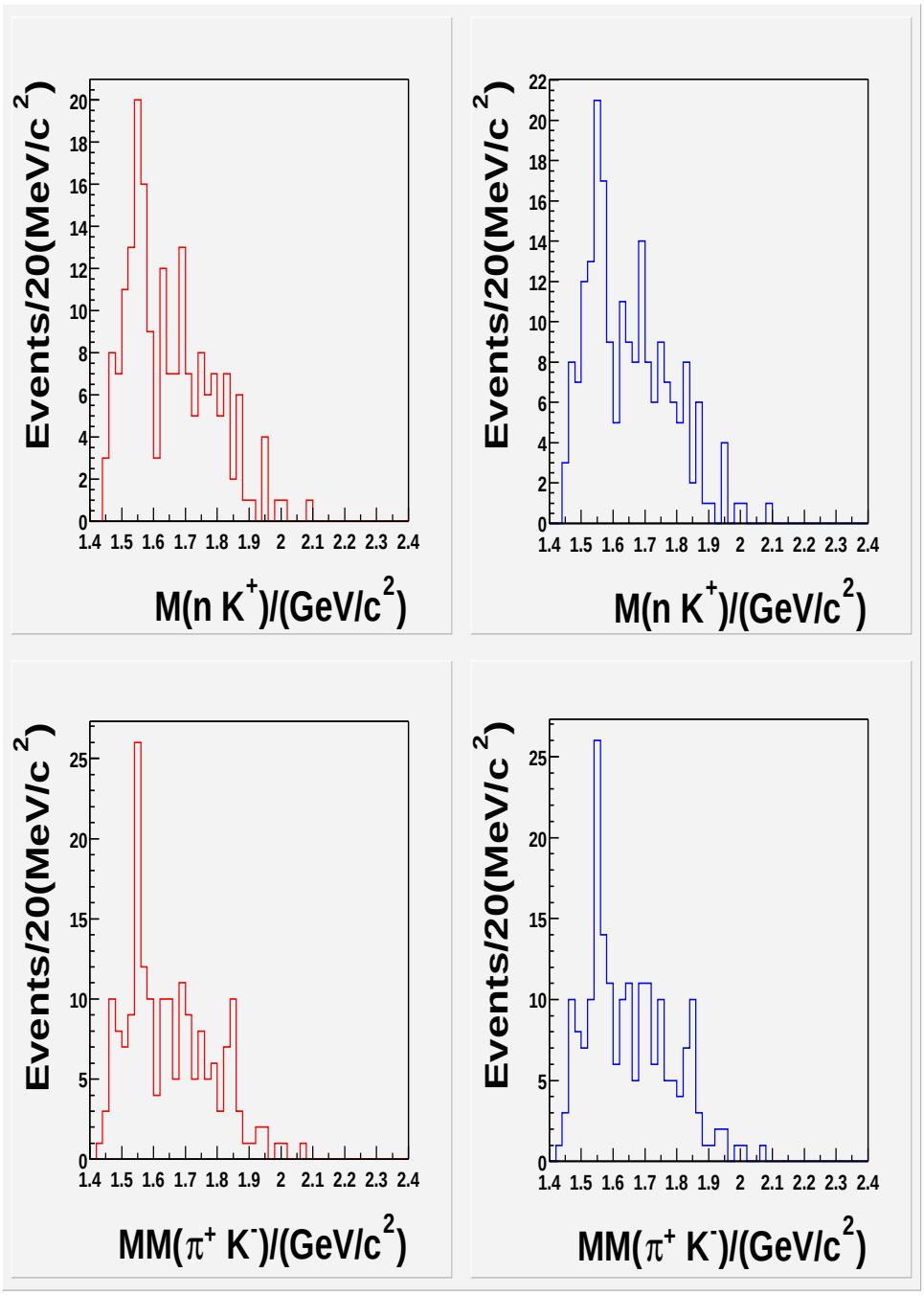

Figure 69: Top Left (Red) histograms are the nK^+ invariant mass spectra calculated using the constrained neutron 4 vector, while bottom panels are the the nK^+ invariant mass spectra calculated using missing mass of the $K^-\pi^+$ system.Left panels have angular cuts of $cos\theta^*_{\pi^+} > 0.5$ and $cos\theta^*_{K^+} < 0$, while right panels replace the π^+ CM system angle cut with $|t'(\gamma \to \pi^+)| < 1\text{GeV/c}^2$ cut. All four panels require the nK^+K^- invariant mass fall into the 2.3-2.6 GeV/c^2 region.

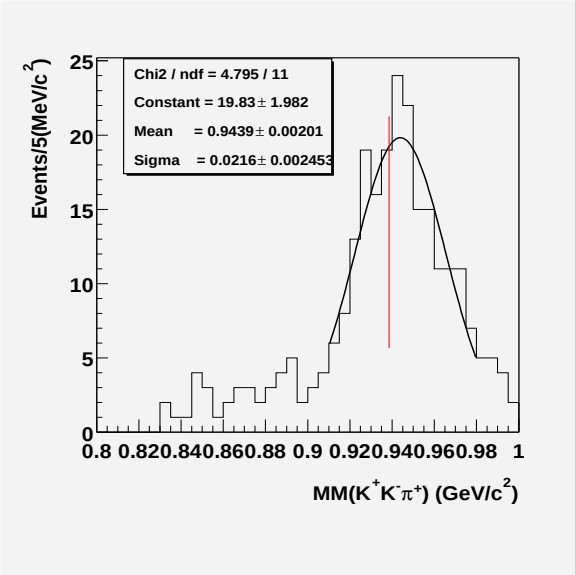

Figure 70: The missing mass off $(K^+K^-\pi^+)$ system in the reaction of $gammap \rightarrow K^+K^-\pi^+X$ for events that have $cos\theta^*_{\pi^+} > 0.5$ and $cos\theta^*_{K^+} < 0$ which were used to extract the Θ^+ signal. The red line shows the PDG position of the neutron mass. The Gaussian fit peak position is 0.9439 GeV/c^2, about 4 MeV shifted toward to the higher end.

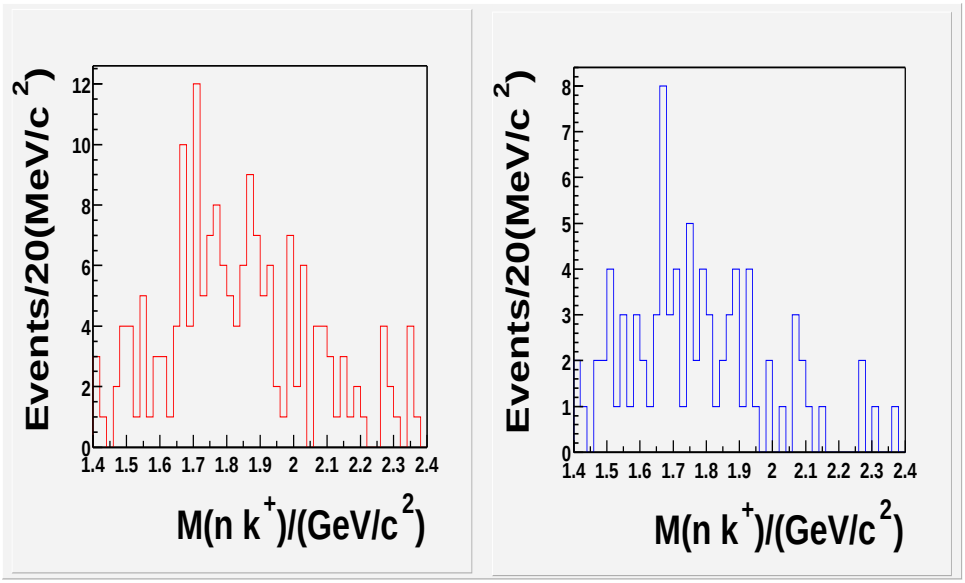

Figure 71: Left: (nK^+) invariant mass spectrum for the side band events shown in the red band of Fig. 49 that are between 2 to 5 σ from the neutron peak, selecting backward going K^+ in the CM system with $cos(\theta^*_{K^+}) < 0.6$. Right: (nK^+) invariant mass spectrum, selecting backward going K^+ in the CM system with $cos(\theta^*_{K^+}) < 0$. Both selected events around the $\bar{K}^{*0}$ peak. Both select events with forward going π^+ in the CM system: $cos(\theta^*_{\pi^+}) > 0.8$

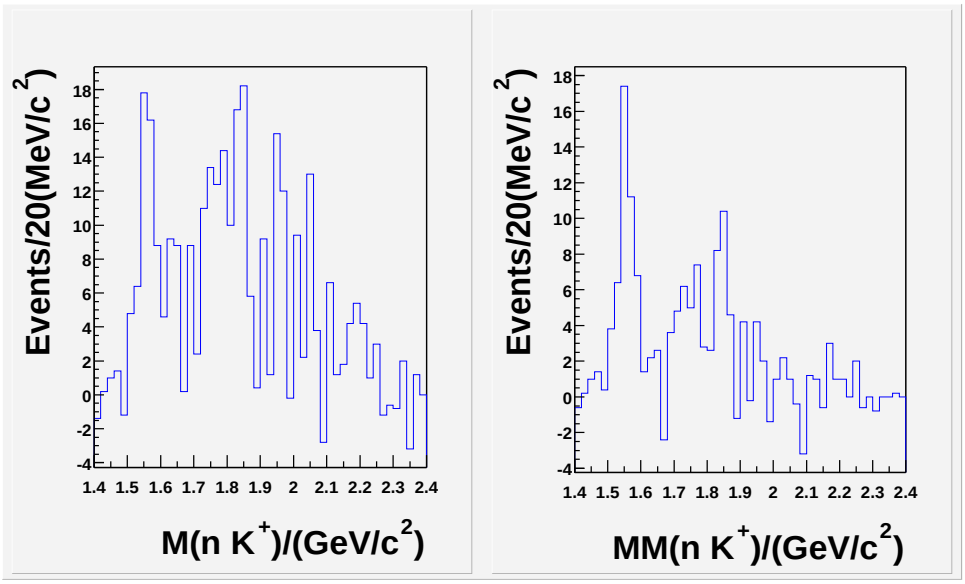

Figure 72: Left: (nK^+) invariant mass spectrum after side band subtraction, selecting backward going K^+ in the CM system with $cos(\theta^*_{K^+}) < 0.6$. Right: (nK^+) invariant mass spectrum, selecting backward going K^+ in the CM system with $cos(\theta^*_{K^+}) < 0$. Both selected events around the $\bar{K}^{*0}$ peak. Both select events with forward going π^+ in the CM system: $cos(\theta^*_{\pi^+}) > 0.8$

constraining the K^+ to be a π^+ using the detected 3-momentum, and calculate the invariant mass spectrum of the neutron and this pion. The result is shown in Fig. 73. The invariant mass of neutron and this hypothetical pion peaks around 1.4 GeV, which should be a pure result of kinematics. The CM angle cut on this particle does not change the mass spectrum. (Note that $\Sigma(1385)$ decays to $\Sigma(1189)\pi$, not $n\pi^+$.)

Combining with the other two data sets

The condictions of *Run a*, *b*, and *c* are close enough that to increase statistics the data can be safely added together. Here the combined analysis of all three data sets, covering a photon beam energy range of 3-5.47 GeV, will be presented. Just as in *Run c*, the neutron is identified using the missing mass technique in the reaction $\gamma p \to \pi^+ K^- K^+ X$. Since the torus magnetic current was reduced to half maximum in *Run c*, the momentum resolution is in turn degraded. As seen in Table 5 and Fig. 74,

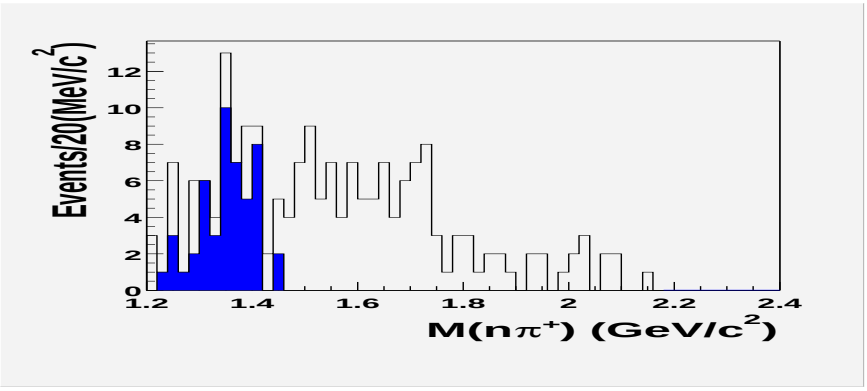

Figure 73: $(n\pi^+)$ invariant mass spectrum for those events that pass the angular cuts:$cos(\theta^*_{K^+}) < 0$ and $cos(\theta^*_{\pi^+}) > 0.8$, the π^+ four vector is obtained by using the measured K^+ three momentum and compute the energy using $E^2 = m^2_{\pi^+} + P^2_{K^+}$. The blue shaded histogram are for those events under the possible Θ^+ peak around 1.55 GeV/c^2($1.52 < M(nK^+) < 1.6$GeV/c^2.

both *Run a* and *b* have a neutron mass resolution around 10 MeV/c^2 while *Run c* has a resolution of about 20 MeV/c^2; therefore, an individual neutron selection criteria was applied for each running period as the events with $|mm(K^+K^-\pi^+) - M_n| < 2\sigma$ are selected. The value of σ for the neutron missing mass peak is listed in Table 5.

Table 5: Neutron missing mass in the reaction $\gamma p \to \pi^+ K^- K^+ X$

Run period	Neutron mass	Resolution (σ)	$M_{missing} - M_n$
g6a	942.3 MeV	9.6 MeV	2.7 MeV
g6b	942.7 MeV	11.4 MeV	3.1 MeV
g6c	938.9 MeV	19.0 MeV	-0.7 MeV

Angular cuts

The same angular cuts in the center of mass system as used in the analysis of the *Run c* data set were applied to the other two data sets to extract the signal and suppress the background. The limits of the angular cuts are varied to see their effect on the nK^+ invariant mass distribution . Fig. 75 shows the dependence on the π^+ CM

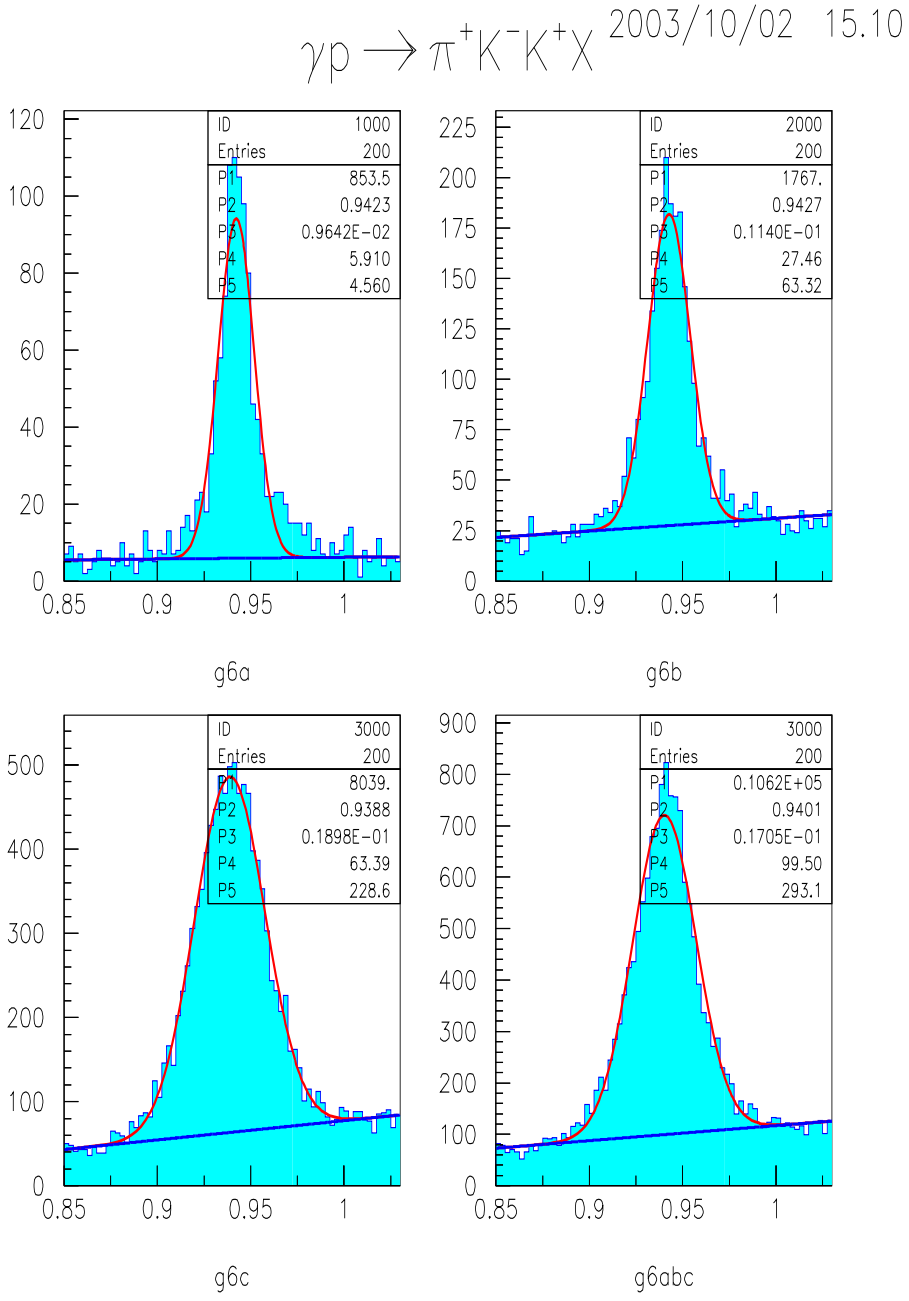

Figure 74: Missing mass distribution in the reaction $\gamma p \to \pi^+ K^- K^+ X$. The peak is the neutron. The four panels (clockwise) are for the *Run* a, b, c and combined spectrum.

angular cuts of the nK^+ invariant mass distribution for the reaction $\gamma p \to \pi^+ K^- K^+ n$ for the combined statistics of all three data sets. The signal becomes more significant when the value of the lower limit of $cos\theta^*$ is increased until the low acceptance in the most forward region of the CLAS spectrometer limits the statistics.

Also the nK^+ invariant mass spectra for the three data sets using different techniques is compared. The missing mass technique proved to be more or less equivalent to the invariant mass technique. It is important to note again that the neutron peaks in *Run a* and *Run b* are both shifted about 3 MeV/c^2 to the higher end, while the same is also true for the *Run c* events that passed the angular cuts. Ideally, a kinematic fitting can improve all the final particles' four vectors by using energy and momentum conservation. However, the lack of knowledge of the error matrix of the detector made it unrealistic to pursue this approach. Therefore the missing mass technique was used to extract the parameters of the possible $S = 1$ baryon resonance.

Comparison of data and simulation

The *Run c* data has a dominant background from meson production that decays to $K^+K^-\pi^+$. Therefore, the simulation that is used here was generated using phase space with a t slope of 3 (GeV/c^2)^2 from the beam to the $K^+K^-\pi^+$ system to match the distribution of the data. The experimental setup is different in *Run a* and *b*, where the target was in the center of CLAS. The Monte Carlo events for *Run a* and *Run b* were generated using $nK^+\bar{K}^{*0}$ 3-body phase space and $nK^+K^+\pi^+$ 4-body phase space. The final set of accepted simulated events are a mixture of these events and then weighted toward the data according to the $K^+K^-\pi^+$ effective mass spectrum.

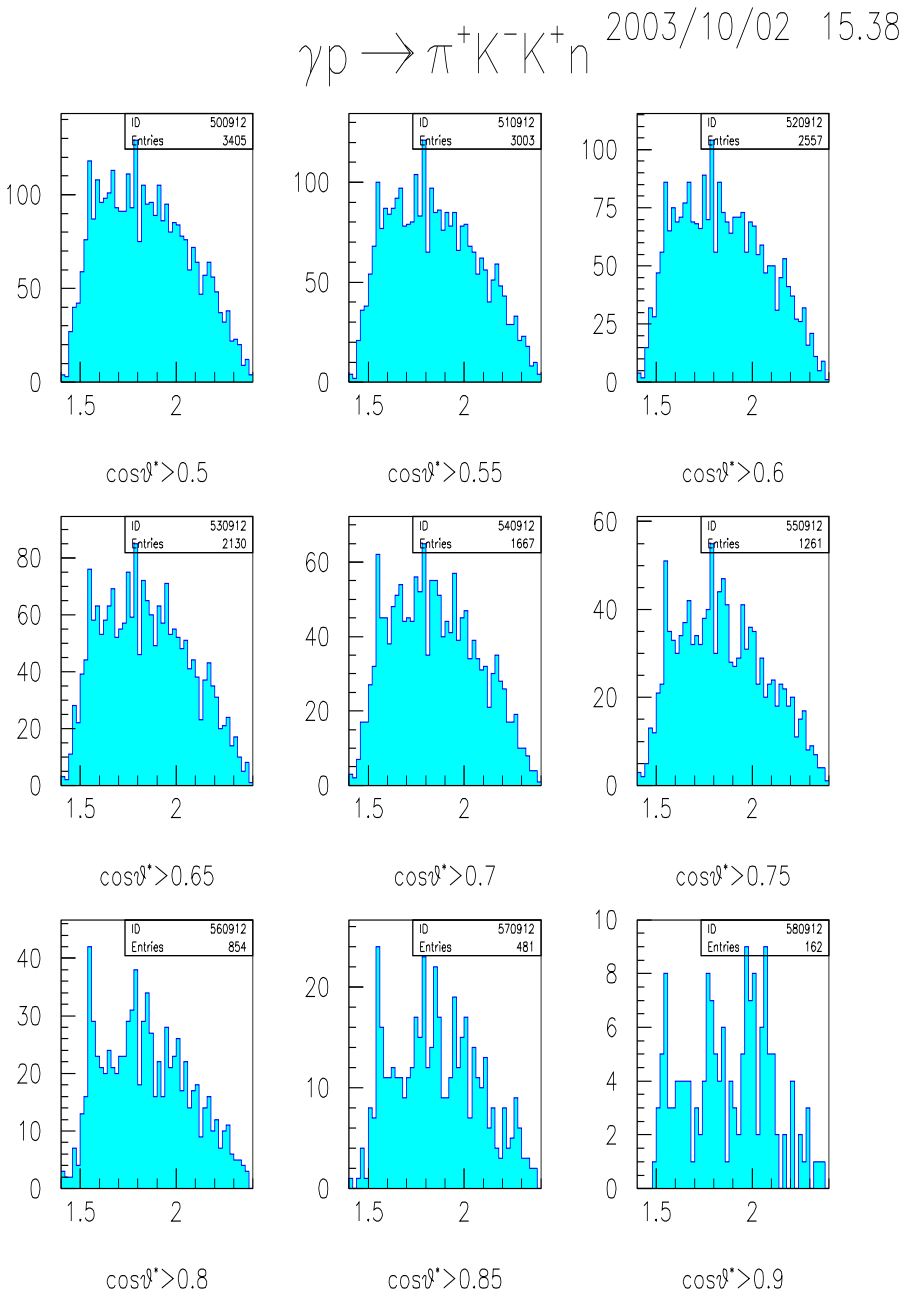

Figure 75: The nK^+ invariant mass distribution for the reaction $\gamma p \to \pi^+ K^- K^+ n$ for combined statistics g6a+b+c for different π^+ angular cut. $\theta^*_{\pi^+}$ is the angle between the
π^+ and photon beam in the center of mass system. There is no cut on the K^+ angle.

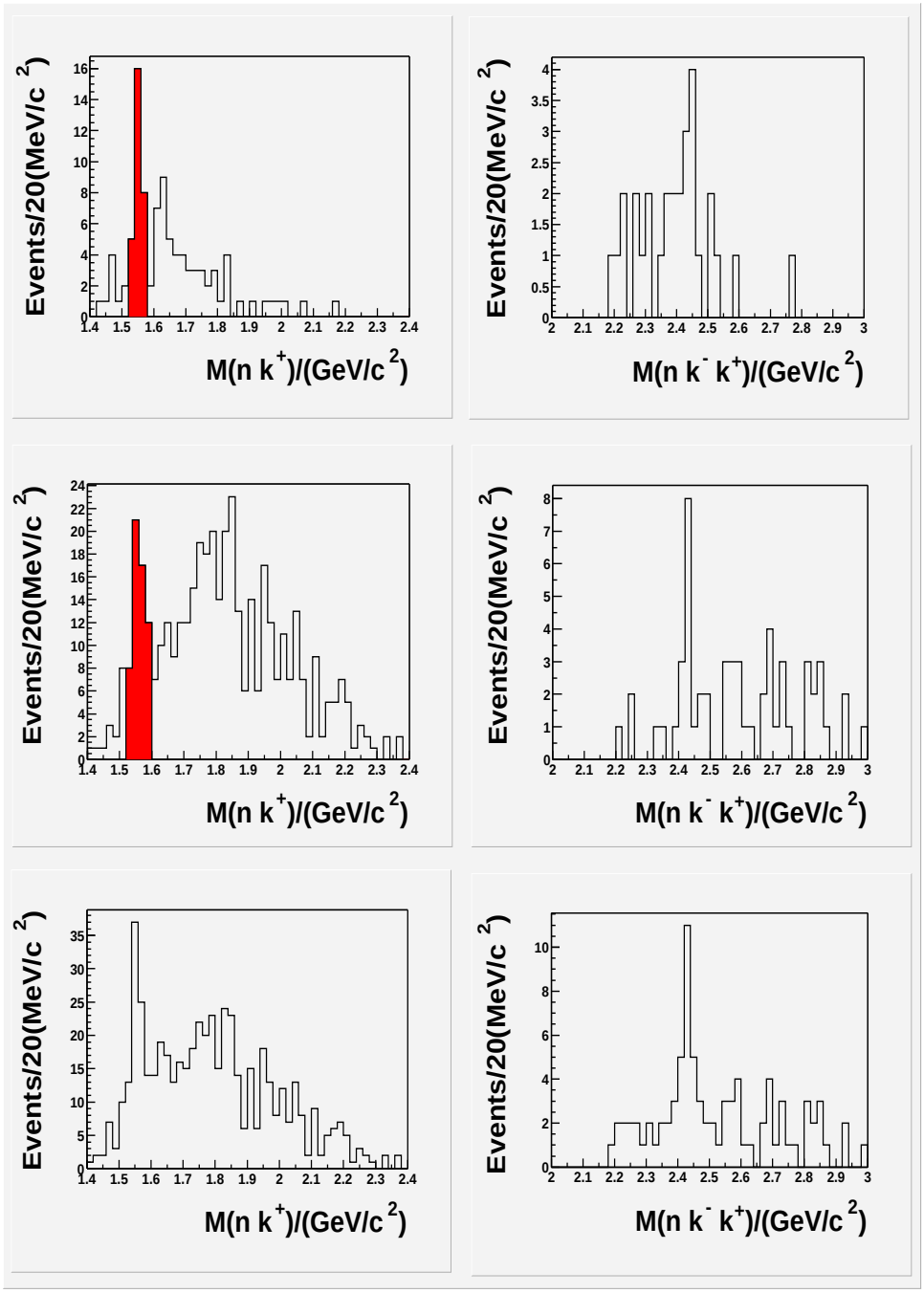

Figure 76: The left panels are the nK^+ invariant mass spectra calculated with missing mass technique. Red regions in the left panels are the events selected around the Θ^+ peak to plot nK^+K^- invariant mass spectra on the right panels. The top panels are from g6ab data, middle panels from g6c and the bottom panels are the sum of the top two. Events with $\pm$ 2σ around the missing mass neutron peak are selected. The missing mass technique is used to calculate the nK^+K^- invariant mass. Angle cuts applied for all the above plots are $cos\theta^*_{\pi^+} > 0.8$ and $cos\theta^*_{K^+} < 0.6$.

The same angular cuts on the simulated events are applied as for the data and found that such cuts do not generate a peak around 1.55 GeV in the nK^+ invariant mass spectrum (Fig. 79), nor does it generate a peak at 2.43 GeV in the nK^+K^- invariant mass spectrum when selecting the events around the Θ^+ mass.

For more detailed comparison, Fig. 77 shows a comparison between the data and the simulation of the nK^+ invariant mass distributions for the different data sets. Fig. 78 shows the comparison between the data and the simulation of the nK^+K^- invariant mass distributions for different data sets.

However, the phase space simulation does not describe the background well. Of course, this is not surprising as we know pure phase space really cannot sufficiently describe the physics background. The important conclusion that one can draw is that angular cuts do not generate narrow peaks in the simulation such as what was observed in the data. Ideally, assuming the background is dominated by meson production where a meson decays to $K^+K^-\pi^+$, the best way to estimate the background is to perform a partial wave analysis on the $K^+K^-\pi^+$ system. This will give a much better description for the background than the naive phase space simulation. The corresponding study is included in the following chapter where the partial wave analysis technique is described in detail.

Discussion of the possible production mechanism for Θ^+ off a proton target

As demonstrated before, selecting $\bar{K}^{*0}$ events does not enable us to see any signal around the Θ^+ region such has been previously reported. The data does seem to suggest the possible production of Θ^+ as a decay product of a heavy nucleon around

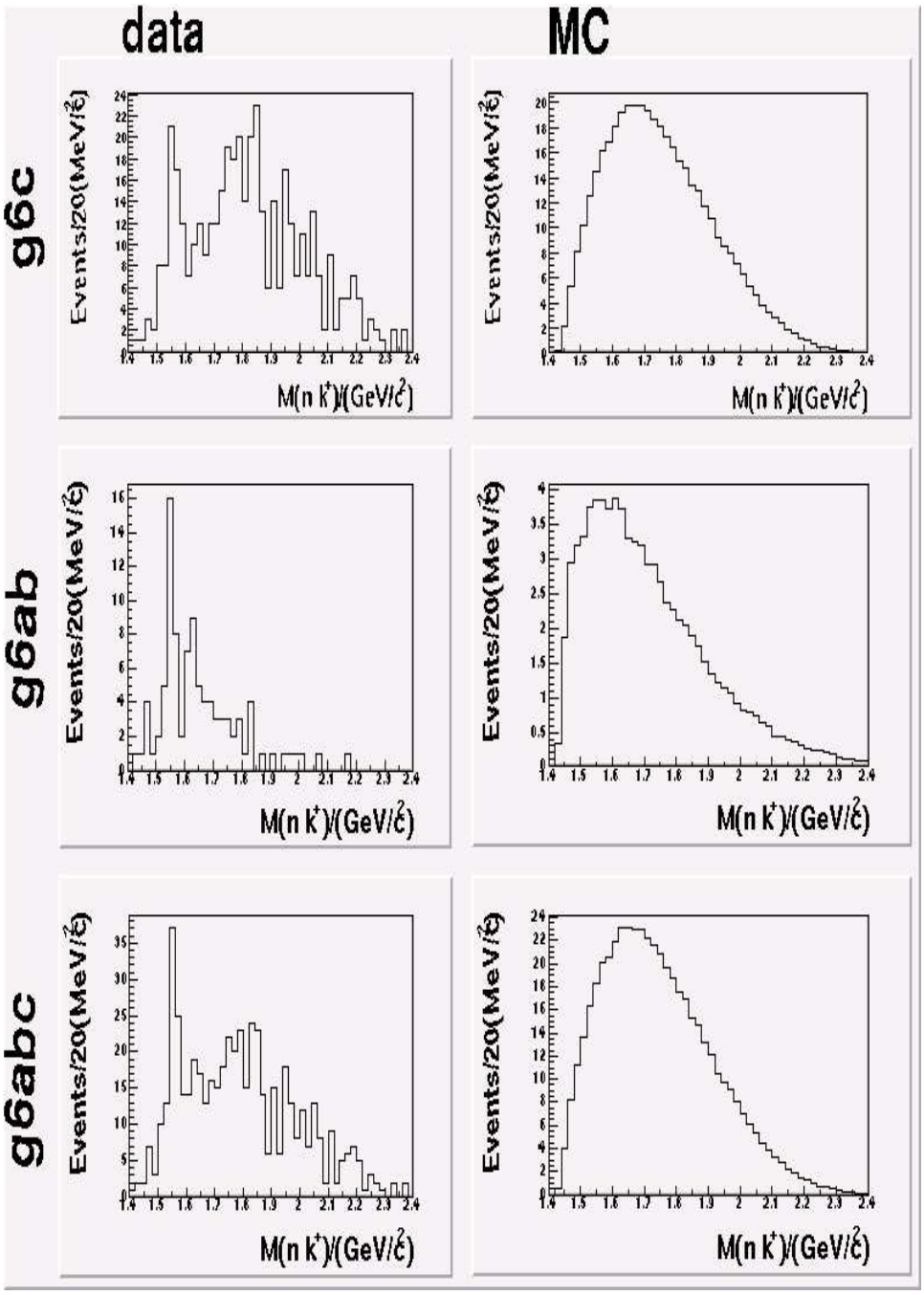

Figure 77: The left panels is the nK^+ invariant mass spectra calculated with the missing mass technique. The right panels are the simulated events of corresponding data sets. The simulation was normalized toward the total event number outside the Θ^+ peak. Angle cuts applied for all the plots are $cos\theta^*_{\pi^+} > 0.8$ and $cos\theta^*_{K^+} < 0.6$.

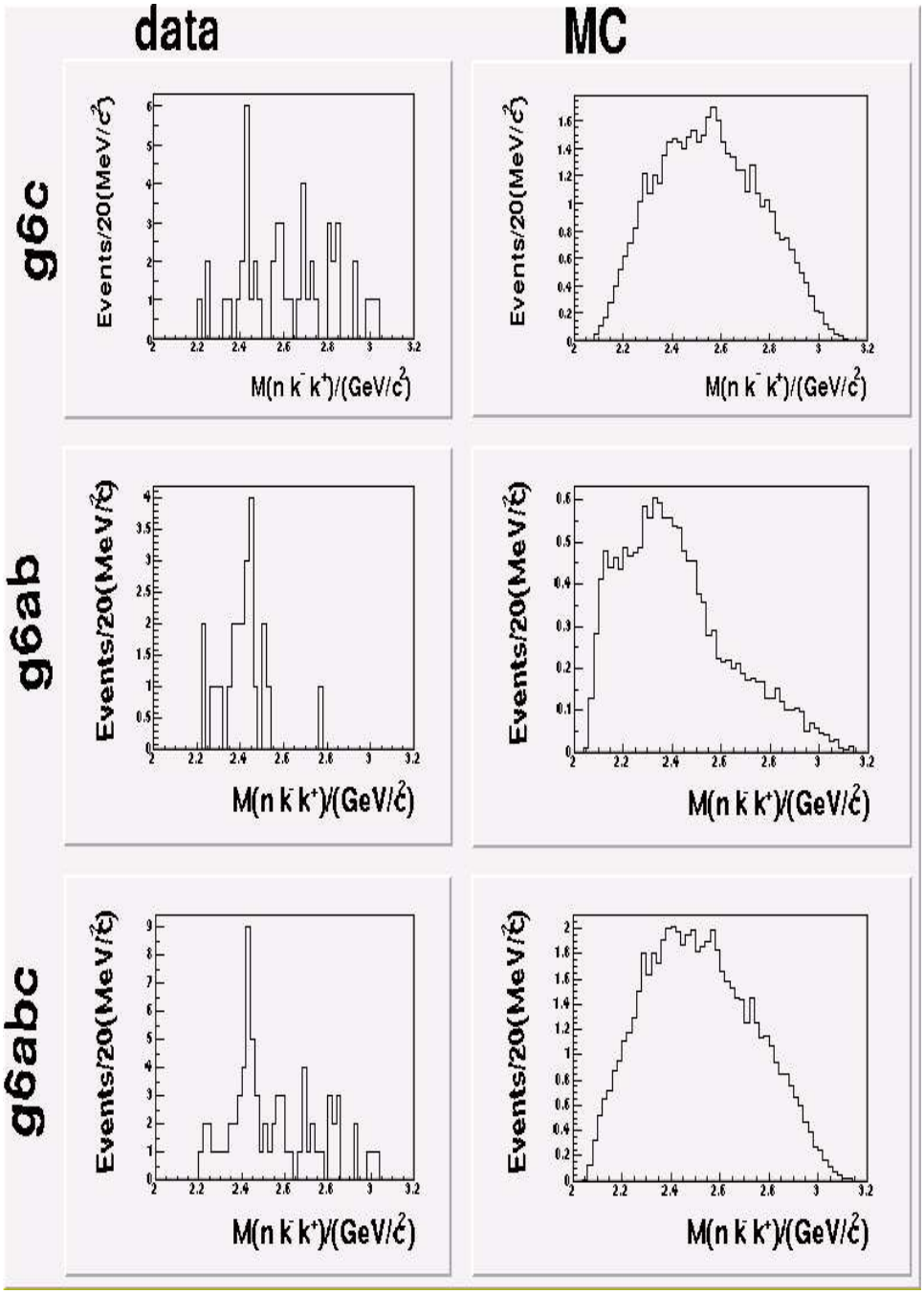

Figure 78: The left panels is the nK^+K^- invariant mass spectra calculated with missing mass technique. The right panels are the simulated events of corresponding data sets. The simulation was normalized toward the total event number outside the N^*/Δ^* peak. Angle cuts applied for all the plots are $cos\theta^*_{\pi^+} > 0.8$ and $cos\theta^*_{K^+} < 0.6$.

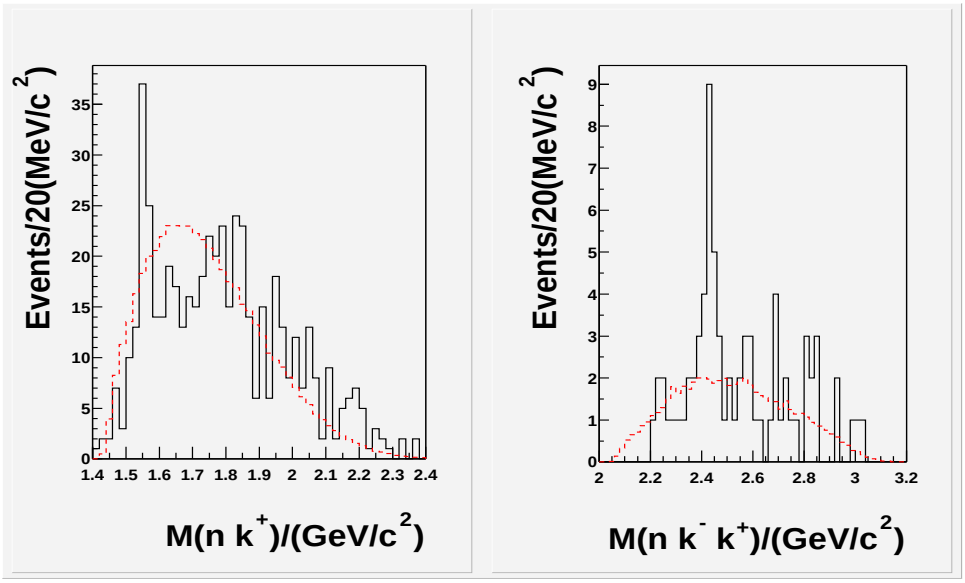

Figure 79: The left plot is the nK^+ invariant mass spectrum calculated with missing mass technique. The right plot is nK^+K^- invariant mass spectrum calculated with missing mass technique. The black solid lines are data from all three data sets and the red dashed lines are simulation. The simulation was normalized toward the total event number outside the Θ^+ peak and the N^*/Δ^* peak. Angle cuts applied for all the plots are $cos\theta^*_{\pi^+} > 0.8$ and $cos\theta^*_{K^+} < 0.6$.

2.43 GeV/c^2. All three data sets covering different photon energy ranges, have the same mass enhancement in both the nK^+ invariant mass spectrum at 1.55 GeV/c^2 as well as a mass enhancement in the nK^+K^- invariant mass spectrum at 2.4 GeV/c^2. Whether the Θ^+ is produced with a $\bar{K}^{*0}$ or not can be further investigated by checking the correlation of the signal with the $\bar{K}^{*0}$. As demonstrated in Fig. 81, the Θ^+ signal is clearly associated with the non-$\bar{K}^{*0}$ events, while the nK^+ invariant mass spectrum looks very much like the background, which peaks around 1.8 GeV/c^2. This is what one would expect if the Θ^+ is not produced in association with the $\bar{K}^{*0}$. The small excess of events around 1.55 GeV/c^2 in the top plot of Fig. 81 should be due to the non-$\bar{K}^{*0}$ events that fall under the $\bar{K}^{*0}$ peak. One may wonder why the Θ^+ is not observed in association with a $\bar{K}^{*0}$, for which the cross section has been calculated [64].

One possible explanation is offered by Reference [67]. As discussed in Chapter 1, the t-channel production of the Θ^+ such as the process shown the Fig. 17, would be forbidden if the Θ^+ has isospin 2. The isotensor Θ^+, on the other hand, can be a decay product of a heavy nucleon. For those events that fall near 1.55 GeV in the nK^+ invariant mass spectrum, the $|t'|$ distribution (Fig. 82) has an exponential shape, with $t' = t - t_{min}$, and t being the momentum transferred from the photon to the forward π^+. The hole at the very low end is a result of the small opening of the CLAS detector along the beam line. The small slope of the $|t'|$ distribution may indicate some other exchange particles than the pion, which might explain the absence of such an N^* or Δ^* resonance in the $p\pi$ elastic scattering experiments.

Although the excess of events in the nK^+K^- invariant mass spectra in all three data sets seems to be suggestive of a heavy nucleon state which decays into a Θ^+ and a K^-, the lack of statistics makes it difficult to make further conclusions on the exact nature of the production mechanism of the Θ^+.

Extracting the parameters of the Θ^+

The final nK^+ effective mass distribution (Fig. 83) for the combined three data sets was fitted by the sum of a Gaussian function and a background function obtained from the simulation as discussed previously. The fit parameters are: $N_{\Theta^+} = 41 \pm 10$, $M = 1555 \pm 1$ MeV/c^2, and $\Gamma = 26 \pm 7$ MeV/c^2 (FWHM), where the errors are statistical. The systematic mass scale uncertainty is estimated to be ± 10 MeV/c^2. This uncertainty is larger than our previously reported uncertainty [51] because of the different energy range and running conditions, and is mainly due to the momentum

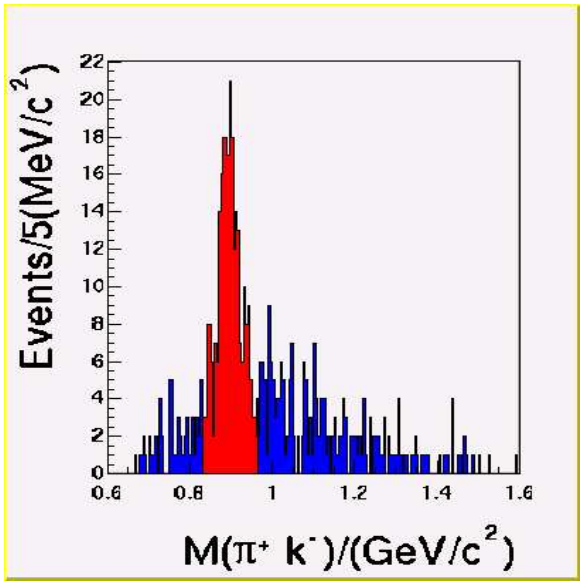

Figure 80: The $K^-\pi^+$ invariant mass spectrum for those events shown in Fig. 83. Angle cuts applied for all the plots are $cos\theta^*_{\pi^+} > 0.8$ and $cos\theta^*_{K^+} < 0.6$.

calibration of the CLAS detector and the photon beam energy calibration. The statistical significance for the fit in Fig. 83 over a 40 MeV/c^2 mass window is calculated as $N_P/\sqrt{N_B}$, where N_B is the number of counts in the background fit under the peak and N_P is the number of counts in the peak. The significance is estimated to be 7.8 $\pm$ 1.0 σ. The uncertainty of 1.0 σ is due to the different background functions that have been tried. When a simple polynomial background is used, the statistical significance is higher. Here the background function obtained from the simulation as discussed above is used. The peak position is sensitive to the choice of binning and the kinematic cuts used to extract the signal, which gives an uncertainty around 7 MeV^2. In conclusion, the possible Θ^+ mass is $1555\pm7\pm10$ MeV/c^2 with a statistical significance of 7.8 $\pm$ 1.0 σ.

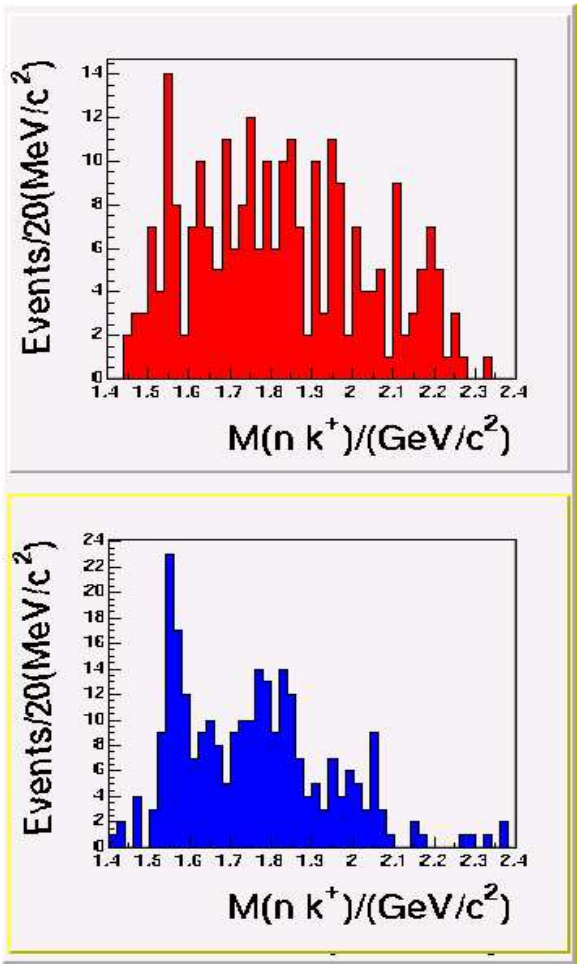

Figure 81: Top Red histogram: The nK^+ invariant mass spectra for the $\bar{K}^{*0}$ events shown in the red region in Fig. 80. Bottom blue histogram: The nK^+ invariant mass spectra for the events outside the $\bar{K}^{*0}$ peak shown in the blue region in Fig. 80. Angle cuts applied for all the plots are $cos\theta^*_{\pi^+} > 0.8$ and $cos\theta^*_{K^+} < 0.6$.

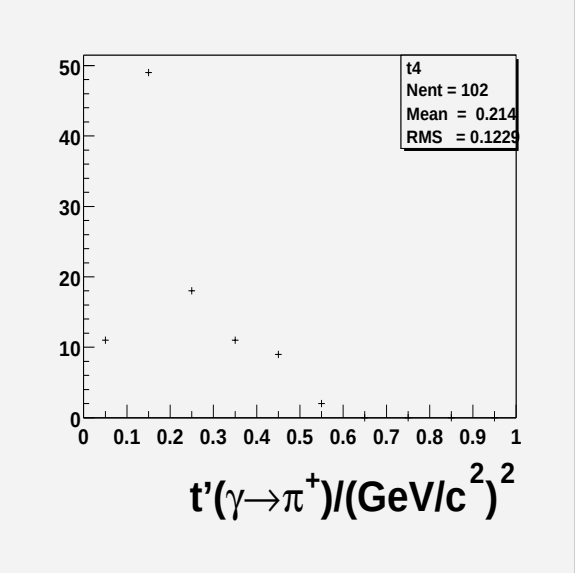

Figure 82: The plot shows the $|t'|$ distribution of g6a, g6b, g6c combined events, with $t' = t - t_{min}$ and t being the momentum transferred from photon to the forward going π^+. The events in this plot has the angle cuts of $cos\theta^*_{\pi^+} > 0.8$ and $cos\theta^*_{K^+} < 0.6$, and $m(nK^+)$ between 1.52-1.6 GeV.

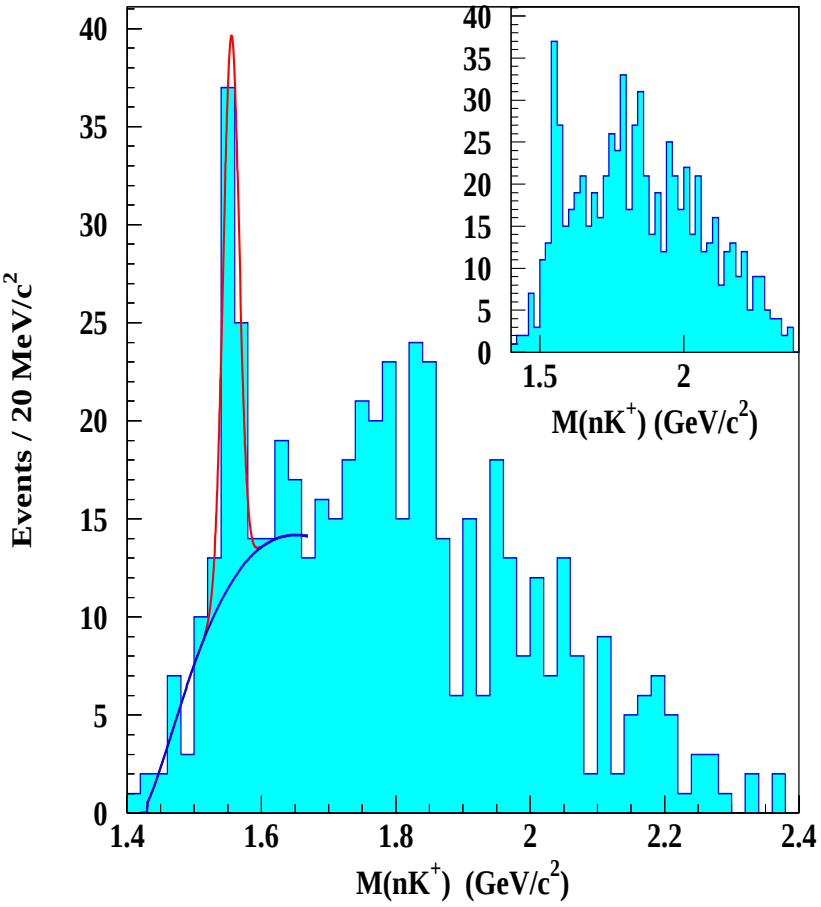

Figure 83: The nK^+ invariant mass spectrum in the reaction $\gamma p \to \pi^+ K^- K^+(n)$ with the cut $\cos\theta^*_{\pi^+} > 0.8$ and $\cos\theta^*_{K^+} < 0.6$. $\theta^*_{\pi^+}$ and $\theta^*_{K^+}$ are the angles between the π^+ and K^+ mesons and photon beam in the center-of-mass system. The background function used in the fit was obtained from the simulation. The inset shows the nK^+ invariant mass spectrum with only the $\cos\theta^*_{\pi^+} > 0.8$ cut.

CHAPTER V

PARTIAL WAVE ANALYSIS FORMALISM

In the case of a low statistics signal, it is always a worry that some particular background combination may cause artificial peaks. In the reaction $\gamma p \to \pi^+ K^- K^+(n)$, the dominant background is the production of mesons which sequentially decay to $\bar{K^{*0}} K^+$ or $(K^+K^-)\pi^+$, as well as the production of Δ's or N^*'s which decay to $n\pi^+$ in association with mesons decaying to K^+K^-. As discussed in the previous chapter, the kinematic cuts that were applied significantly suppressed these backgrounds, particularly the latter. However, one cannot rule out the possibility of some unusual angular combination of meson waves which could generate the Θ^+ peak that was observed. In this chapter, the procedure of partial wave analysis (PWA) to accurately describe the meson background in the Θ^+ production from the reaction of $\gamma p \to \pi^+ K^- K^+(n)$ will be described.

The formalism of PWA

Partial Wave Analysis is a technique used in hadron spectroscopy to extract information about the spin-parity and decay properties of those resonances that decay to the observed final state particles. It is also a powerful tool to give an almost model-independent description of meson backgrounds existing in the production of the Θ^+. The PWA method used in this thesis is developed from the BNL Partial Wave Analysis Programs by Cummings and Weygand [90, 91]. It is based on the

isobar model [1] for describing the production and decay of resonances [92]. The idea of PWA is to parameterize the intensity distribution in terms of variables that have physical meaning when interpreted as properties of intermediate states in a particular hadronic reaction. The formalism here is based on the work by Chung [93] and Chung and Trueman [94].

The intensity distribution decomposition

The differential cross section for the reaction shown in Fig. 84 can be written as:

$$\frac{d\sigma}{dtdWd\tau} \propto |\mathcal{M}|^2 pq \tag{22}$$

where $t = (p_1 - p_3)^2$ is the usual Mandelstam variable. p_1 and p_3 denote the momenta of the photon and X, W is the mass of X, p is the momentum of the isobar in the X rest frame (XRF), and q is the momentum of one of the decay products (i.e., the analyzer) of the isobar in its helicity frame (IRF).

$$\tau = \{\Omega, \Omega_h, w\} \tag{23}$$

denotes the kinematic variables that configure the final state. $\Omega = (\theta, \phi)$ are the polar and azimuthal angles of the isobar in the X rest frame (XRF), $\Omega_h = (\theta_h, \phi_h)$ are the angles for one of the isobar decay products in the isobar rest frame (IRF), and w is the mass of the isobar. In this analysis, the Gottfried-Jackson (GJ) frame, which is the rest frame of the resonance X^+ that decays to $K^+K^-\pi^+$, is chosen as the reference framewith the z axis along the beam direction and the y axis normal to the production plane.

[1] The isobar model regards the n-body final state as the result of a series of sequential decays (usually two body) through intermediate states know as the isobars.

The invariant amplitude $\mathcal{M}$ is a matrix element of the transition operator, $\hat{T}_{fi}$, which transforms the initial state $|i\rangle$ into the final state $|f\rangle$,

$$\mathcal{M} = \langle f|\hat{T}_{fi}|i\rangle \tag{24}$$

The isobar model assumes that $\hat{T}_{fi}$ is a product of a production operator $\hat{T}_{mi}$ and a decay operator $\hat{T}_{mi}$ so that the transition amplitude maybe be written as:

$$\mathcal{M} = \sum_{m}\langle f|\hat{T}_{fm}|m\rangle\langle m|\hat{T}_{mi}|i\rangle \tag{25}$$

where $|m\rangle$ represents a set of basis states with properties obeying the conservation laws in strong interaction . Therefore, the intensity distribution is a sum of amplitudes squared appropriately to account for interference:

$$I(\tau) = \sum_{\alpha}\{|\sum_{\beta}\psi_{\alpha\beta}(\tau)|^2\} \tag{26}$$

can now be written as

$$I(\tau) = \sum_{\alpha}\{|\sum_{\beta}V_{\alpha\beta}A_{\alpha\beta}(\tau)|^2\} \tag{27}$$

The subscripts α and β are the parameters that describe the partial wave decomposition. α specifies properties of the intermediate states that do not interfere, such as the spin states of the incoming or outgoing particles with β represents properties that do interfere, such as the spin states of broad resonances produced as intermediate states in a sequential decay.

The amplitudes can be written either in the helicity basis or the reflectivity basis [94]. In this analysis, the latter was chosen. In the reflectivity basis, the sum over amplitudes splits into non-interfering sets of fully interfering amplitudes, or

$\alpha = \{\epsilon, k\}$, as parity conservation in the production precess is imposed in a canonical way. Both the production and decay amplitudes depend on ϵ, while the decay amplitude does not depend on k, which denotes the spin configuration of the amplitudes. The intensity distribution then becomes

$$I(\tau) = \sum_{\epsilon,k} \{ | \sum_{\beta} V^{\epsilon}_{k\beta} A^{\epsilon}_{\beta}(\tau) |^2 \} \tag{28}$$

The decay amplitudes $A^{\epsilon}_{\beta}(\tau)$ can be calculated for each event. It can be factored into two functions, separating the dependence on the isobar mass w and momentum from that of the angles,

$$A^{\epsilon}_{\beta}(\tau) = E^{JLs*}_{M}(\Omega_{GJ}, \Omega_h) Q^{\nu}_{Ls}(w) \tag{29}$$

The functions E^{JLs}_{M} form a complete orthonormal set spanning the space of the four angles Ω_{GJ} and Ω_h:

$$E^{JLs*}_{M}(\Omega_{GJ}, \Omega_h) = \tilde{L}\tilde{s} \sum_{\lambda} {D^{J}_{M\lambda}}^{*}(\phi_{GJ}, \theta_{GJ}, \phi_h) d^{s}_{\lambda 0}(\theta_h) \langle L0s\lambda | J\lambda \rangle \tag{30}$$

where $\tilde{m} \equiv \sqrt{2m+1}$, $\langle L0s\lambda|J\lambda\rangle$ are Clebsch-Gordan coefficients and $D^{J}_{M\lambda} d^{s}_{\lambda 0}$ are the usual $D(d)$ functions (for example, see Rose [96]), with L, s, J being the orbital angular momentum between the isobar and the bachelor particle, spin of the isobar and total spin of the resonance, respectively. λ is the helicity of the isobar and is summed over $-s$ to s.

The mass and momentum dependence is given by:

$$Q^{\nu}_{Ls}(w) = F_L(p) F_s(q) \Delta_{\nu}(w) \tag{31}$$

where the functions F are the Blatt-Weisskopf centrifugal-barrier factors as given by Von Hippel and Quigg [97],

$$\begin{aligned} F_0(p) &= 1 \\ F_1(p) &= \sqrt{\frac{2z}{z+1}} \\ F_2(p) &= \sqrt{\frac{13z^2}{(z+1)^2+9z}} \end{aligned} \tag{32}$$

where $z = (p/p_r)^2$ and $p_r = 0.1973$ GeV/c^2 corresponds to a radius of 1 fm.

The mass dependence for the isobar is contained in $\Delta_\nu(w)$ which has the standard Breit-Wigner form for the isobar ν,

$$\Delta_\nu(w) = \frac{w_0\Gamma_0}{w_0^2 - w^2 - iw_0\Gamma_\nu(w)} \tag{33}$$

with

$$\Gamma_\nu(w) = \Gamma_0 \frac{w_0}{w}\frac{q}{q_0}\frac{F_s^2(q)}{F_s^2(q_0)} \tag{34}$$

where w_0 and Γ_0 are the mass and width of the isobar and $q_0 = q(w_0)$ so that $\Gamma_\nu = \Gamma_0$ and $\Delta_\nu(w_0) = 1$. Note that the w dependence of the width is assumed to be given by the two-body phase-space factor q/w with the decay amplitude given by $F_s(q)$. More detailed information on the decay amplitude calculation can be found in reference [93].

The production amplitude $V_{k\beta}^{\epsilon}$ is unknown. By varying the value of $V_{k\beta}^{\epsilon}$ the predicted intensity distribution above is matched as closely as possible by the observed intensity as a function of all kinematic variables. This is done through an extended maximum likelihood fit, which will be described in the following subsection.

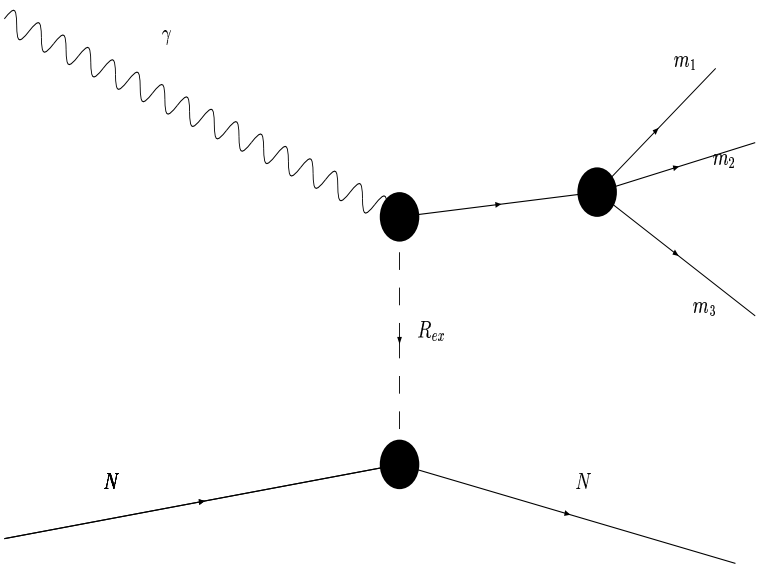

Figure 84: Diagram representing the amplitude $\psi_{\alpha\beta}(\tau)$. The intermediate state X is produced by the exchange of a Reggion R_{ex} between the photon beam and the nucleon target.

The Extended Maximum Likelihood Fit

The likelihood function is defined as a product of probabilities:

$$\mathcal{L} = [\frac{\bar{n}^n}{n!}e^{-\bar{n}}] \prod_i^n [\frac{I(\tau_i)}{\int I(\tau)\eta(\tau)d\tau}] \tag{35}$$

where $I(\tau_i)$ is the intensity distribution as seen in Eq. 27, $\frac{\bar{n}^n}{n!}e^{-\bar{n}}$ is the Poisson probability of observing n events. The integral function $\int I(\tau)\eta(\tau)d\tau$ contains the acceptance, $\eta(\tau)$, and is referred to as the accepted normalization integral.

The function which is actually maximized in the likelihood fit is

$$ln\mathcal{L} = \sum_i^n [ln \sum_{k,\epsilon,\beta,\beta'} V_{k\beta}^{\epsilon} V_{k\beta'}^{\epsilon *} A_{\beta}^{\epsilon}(\tau_i) A_{\beta'}^{\epsilon *}(\tau_i)] - n[\sum_{k,\epsilon,\beta,\beta'} V_{k\beta}^{\epsilon} V_{k\beta'}^{\epsilon *} \psi_{\beta\beta'}^{\epsilon x}] \tag{36}$$

The first sum is over data events, where the term being summed over is simply the intensity $I(\tau_i)$ for each event. The second term contains the accepted normalization integrals $\psi_{\beta\beta'}^{\epsilon x}$ where the superscript x means accepted. This integral is readily evaluated numerically by a Monte-Carlo (MC) method.

$$\psi^{\epsilon x}_{\beta\beta'} = \frac{1}{M_x}\sum_{i}^{M_x} A^{\epsilon}_{\beta}(\tau_i)A^{\epsilon *}_{\beta'}(\tau_i) \tag{37}$$

The sum is performed over a simulated Monte-Carlo data set of M_x events.

Monte Carlo Simulation

The Monte Carlo (MC) events were generated using a phase space generator (*ppgen*). The raw Monte Carlo events were put through a GEANT-based detector simulation of CLAS called GSIM. To match the MC distributions with the data, as well as to reduce computing time, the MC events were generated with an exponential t dependence of the $K^+K^-\pi^+$ system. The slope used was $b = 3.0$ $(\mathrm{GeV/c^2})^{-2}$ to match the data. Events were generated in 20 MeV/c^2 $K^+K^-\pi^+$ mass bins with 400,00 events per bin. The fits were performed in 80 MeV/c^2 $K^+K^-\pi^+$ mass bins due to the low statistics.

Partial Wave parameterization

.

$\alpha = \{J^P M^{\epsilon} Lisobar\}$ is used to denote the partial waves describing the decay of a resonance into $K^+K^-\pi^+$ final state, with

- J: total spin of resonance R
- P: parity of R
- M: spin projection along the beam axis
- ϵ: reflectivity of R

- *isobar*: isobar used to describe the sequential decay of R
- L: orbital angular momentum between the isobar and the bachelor particle (K^+ or π^+).

As discussed in Appendix A, the $K^+K^-\pi^+$ system is not an eigenstate of G-parity or C-parity. Therefore, the partial wave analysis of the 3-body meson system will only determine its spin and parity, the isospin being 1 because the system is charged.

The total spin, J, can be determined following the angular momentum addition rules, knowing the spin of the isobar and bachelor particles,

$$\vec{J} = \vec{J}_{isobar} + \vec{J}_{bachelor} + \vec{L} \tag{38}$$

The parity, P, can be determined by

$$P = P_{isobar} \cdot P_{bachelor} \cdot (-)^L \tag{39}$$

The data shows a strong $\bar{K}^{*0}$ resonance (Fig. 57) correlated with the meson production. Experimentally it has been established that the $\pi_2(1670)$ decays to $f_2(1275)\pi$ as well as KK^*; therefore the $\bar{K}^{*0}(892)$, the $f_2(1275)$, and the $\bar{K}^{*0}(1430)$ are included as isobars. Both positive and negative reflectivities are allowed. Note that the production amplitudes can be different for different reflectivities.

Ideally, an infinite number of partial waves should be included in order to perform a complete analysis. However, due to the limited statistics, combined with educated assumptions, the value of orbital angular momentum, L, is limited to the lowest allowed values. The centrifugal barrier raised by high L, and the limited phase space would suppress higher L's. The value of J is also limited to less than 4, since one does not expect to see mesons with high spin in the $1 - 2$ GeV/c^2 region [98].

The PWA results

Additional cuts for PWA

In addition to the cuts used for the event selection listed in Table 3, two PWA-only related cuts are applied as listed in Table 6. The first is the t' cut on the momentum transferred to the $K^+K^-\pi^+$ system. The second cut attempts to reduce the $\Delta(1232)$ background.

The four momentum transfer, $|t'|$, is defined as [99]

$$t' = t - t_{min} \tag{40}$$

where

$$t = (P^{\mu}_{target} - P^{\mu}_{recoil})^2 \tag{41}$$

and t_{min} is the value of t when the scattering angle is 0. In the reaction of $\gamma p \to Rp$, $R \to K^+K^-\pi^+$, t_{min} is given by:

$$t_{min} = W_R^2 - 2E_\gamma E_R + 2p_\gamma p_R \tag{42}$$

where W_R is the $K^+K^-\pi^+$ mass. In the peripheral meson production, the t'-dependence generally has the form [99]:

$$\frac{d\sigma}{dt'} = Ae^{-b|t'|} \tag{43}$$

Fig. 85 shows the $t'(\gamma \to (K^+K^-\pi^+))$ distribution with the shaded region showing the events selected for the PWA.

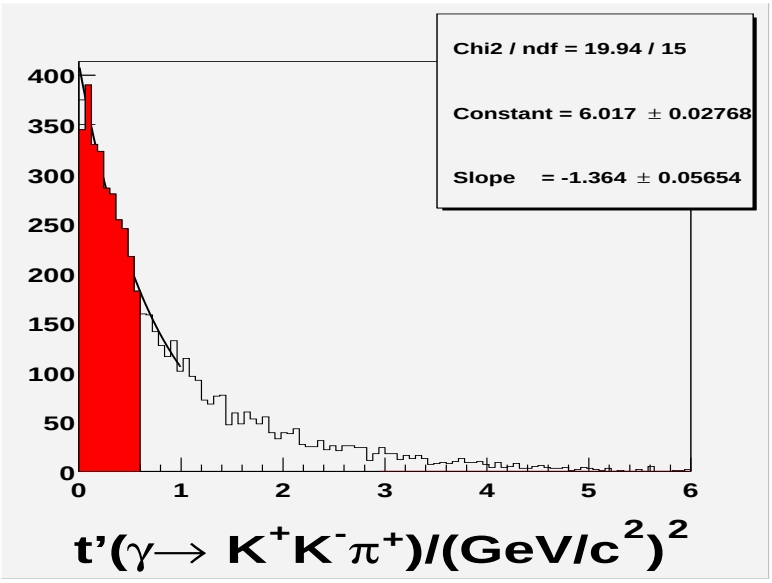

Figure 85: The distribution of $t'(\gamma \to K^+K^-\pi^+)$. The red shaded region are the selected events for partial wave analysis with $t' < 0.6$ (GeV/c^2)^2. This plot requires $\theta_{\pi^+}^{Lab} < 30^o$.

A $\Delta(1232)$ or N^* can be produced through a t-channel process at the baryon vertex as illustrated in Fig. 56 *b*. $\Delta(1232)$'s are found to be correlated with π^+'s that have large polar angles in the laboratory frame. By eliminating those pions, the baryon background from the $\Delta(1232)$ can be reduced (Fig. 86).

Table 6: Event selection for the PWA of the $K^+K^-\pi^+$ meson system in the reaction of $\gamma p \to nK^+K^-\pi^+$ in addition to the cuts illustrated in Table 3

Selection Criteria	**Cuts applied**	Events Survived
π^+ Lab angle	$\theta_{Lab}(\pi^+) \leq 30^o$	6,277
Momentum transferred	$t'(\gamma \to K^+K^-\pi^+) \leq 0.6(\mathrm{GeV}/c^2)^2$	3,136

Wave set

As discussed previously, in principle, an infinite set of partial waves are needed to form a complete basis. However, the statistics is low with only $3K$ events. A fairly

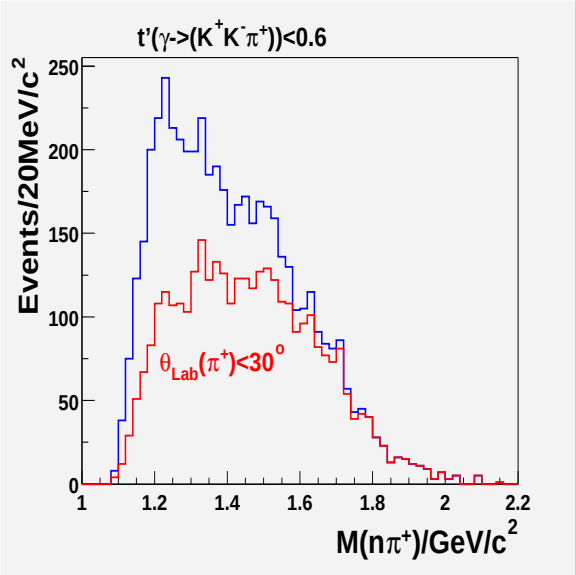

Figure 86: The effect of cutting out pions with large laboratory angles: $n\pi^+$ invariant mass spectra with and without $\theta_{Lab}(\pi^+) \geq 30^o$ cut Blue: without angle cut Red: $\theta_{Lab}(\pi^+) > 30^o$

large set of partial waves was used at the beginning and the smaller waves that had low intensity and large error bars were dropped. Waves that distort the agreement between the data and the fit predicted distributions are also dropped. The goal is to obtain a minimal set of partial waves that can describe the data.

An isotropic background wave was generated as well by assigning a real constant to each event as the background amplitude, assuming that it does not interfere with the foreground meson waves. Table 7 lists the foreground partial waves used in the final fit. The choice of waves are based on both the knowledge of established resonances from previous experiments and theoretical predictions. A total of 22 waves are used in the final fit.

Table 7: Foreground Partial Waves used in the final PWA fit. The wave is identified by $J^P M^\epsilon L$ and Isobars

J^P	M^ϵ	**L**	Isobars	bachelors
0^-	0^+	1	$\bar{K}^{*0}(892)$	K^+
0^-	0^+	0	$K^{*0}(1430)$	K^+
1^-	0^-	1	$K^{*0}(892)$	K^+
1^-	1^-	1	$\bar{K}^{*0}(892)$	K^+
1^+	0^+	1	$K^{*0}(892)$	K^+
1^+	0^+	2	$\bar{K}^{*0}(892)$	K^+
1^+	1^+	1	$K^{*0}(892)$	K^+
1^+	1^+	2	$\bar{K}^{*0}(892)$	K^+
1^+	1^-	1	$K^{*0}(892)$	K^+
1^+	1^-	2	$K^{*0}(892)$	K^+
2^-	1^+	0	$f_2(1270)$	π^+
2^-	1^-	0	$f_2(1270)$	π^+
2^-	1^+	0	$f_2(1270)$	π^+
2^-	1^-	0	$f_2(1270)$	π^+
2^-	1^+	1	$K^{*0}(892)$	K^+
2^-	1^+	3	$K^{*0}(892)$	K^+
2^-	1^-	1	$K^{*0}(892)$	K^+
2^-	1^-	3	$K^{*0}(892)$	K^+
2^-	2^+	1	$K^{*0}(892)$	K^+
2^-	2^+	3	$K^{*0}(892)$	K^+
2^-	2^-	1	$K^{*0}(892)$	K^+
2^-	2^-	3	$K^{*0}(892)$	K^+

Checking the PWA fit quality

The quality of the fits are checked by comparing the various distributions of the data with the prediction of the fits. As shown in Eq. 27, the production amplitudes, $V_{k\beta}^{\epsilon}$, are determined by the fits. Eq. 27 is then used as a weighting function to give each accepted MC event a weight, and the events are propriately normalized. These weighted events are then used as a set of events, which may be used to describe the data, to plot various angular and invariant mass distributions called "fit predicted distributions". The agreement between the fit predicted distributions and the real data distributions should tell us the goodness of the fit.

Fig. 87 shows the comparison of angular distributions of K^+ and π^+ in the G-J frame, and Fig. 88 shows comparisons of various invariant mass spectra. The comparison of the angular distributions of the K^+ and the π^+ in the center-of-mass frame is shown in Fig. 89. The shape of the ϕ angle distribution in the G-J frame for the K^+ and the π^+ were generated by the CLAS acceptance. As we can see, most plots shows excellent agreement between the data and the prediction. The biggest discrepancy comes in the $n\pi^+$ invariant mass spectrum (Fig. 88, bottom left). This is an indication that there is still some baryon background from Δ production in association with the K^+K^- system, and only an isotropic non-interfering background wave was used for the fit. Overall, the quality of the fit is good and the set of weighted accepted MC events describe the data very well.

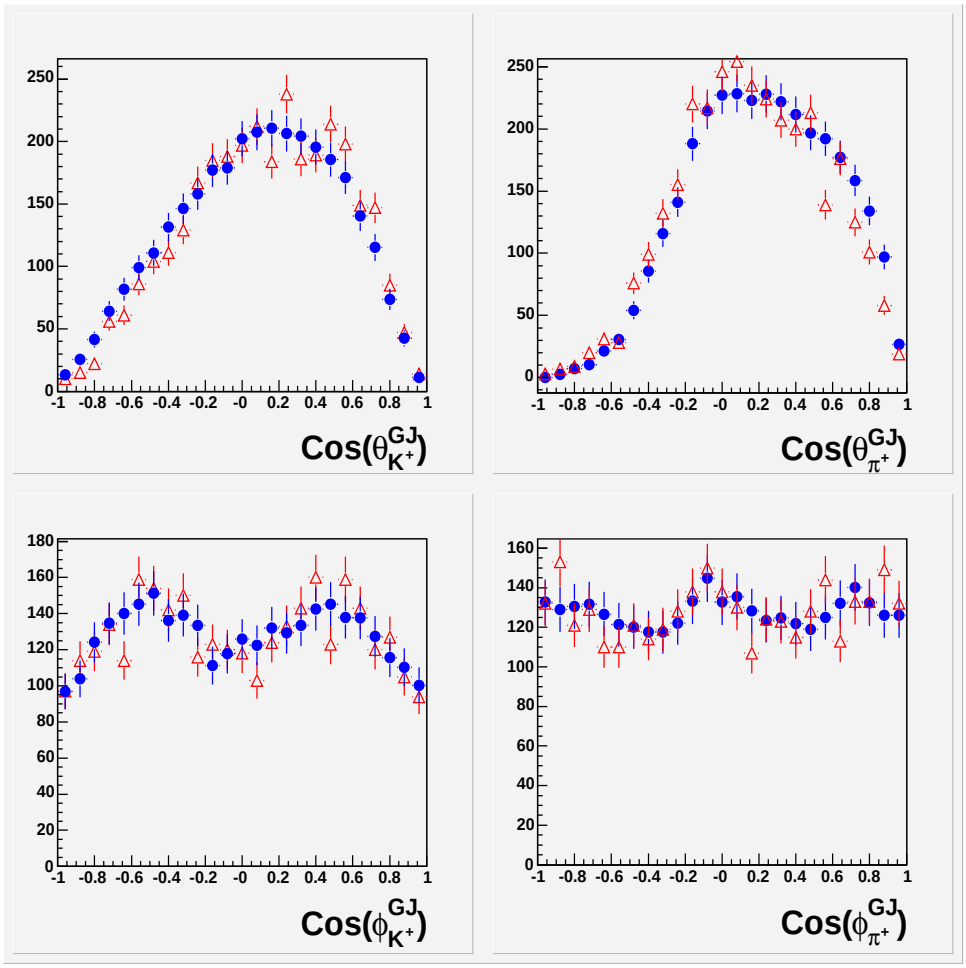

Figure 87: PWA prediction of the G-J angle for K^+ and π^+ compared with data. Red triangle marker is the real data, while blue circles are the prediction of the PWA results. The error bars are only statistical. Top panels are K^+ G-J angles, and bottom panels are π^+ G-J angles.

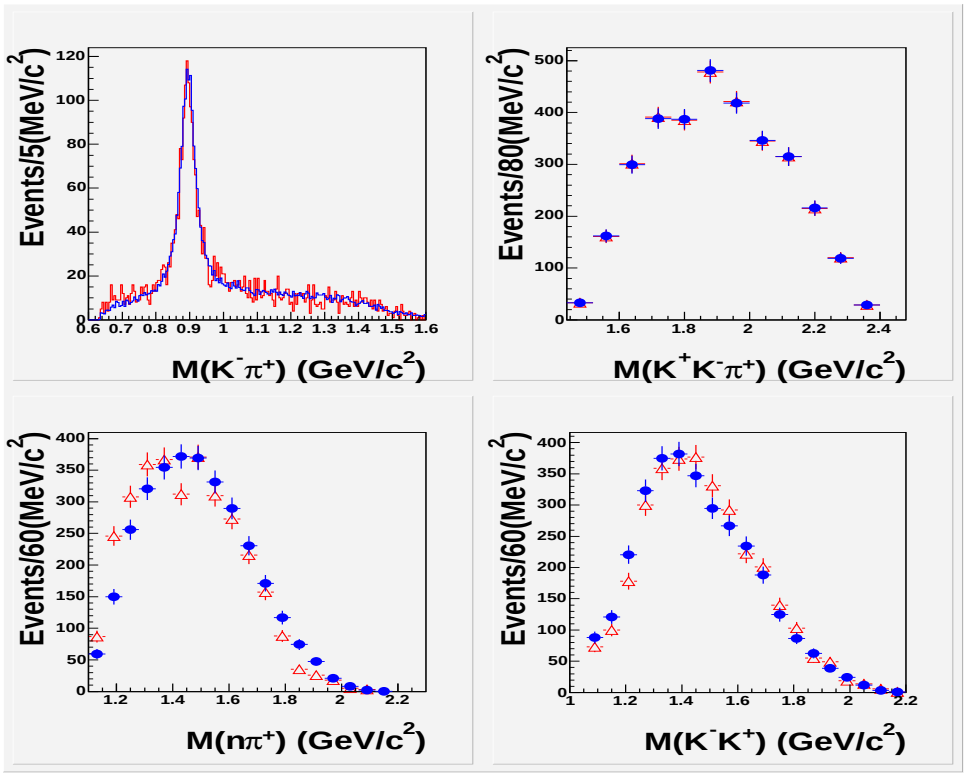

Figure 88: PWA prediction of the invariant masses. Top left: $K^-\pi^+$ invariant mass spectra; Top Right:$K^+K^-\pi^+$ invariant mass spectra; Bottom Left:$n\pi^+$ invariant mass spectra; Bottom Right:nK^+ invariant mass spectra; Red histograms are the real data, while blue histograms are the prediction of the PWA results. The error bars are only statistical.

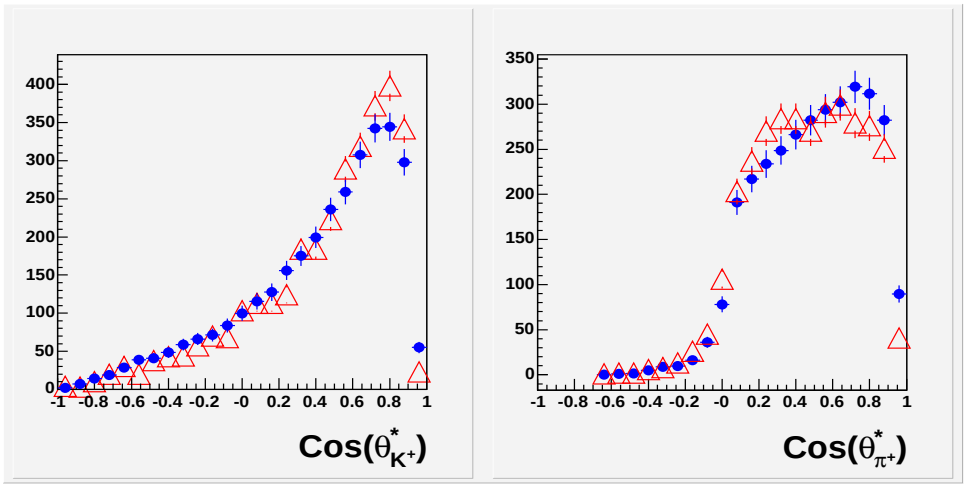

Figure 89: PWA prediction of the CM angle for K^+ and π^+. Red triangle marker is the real data, while blue circles are the prediction of the PWA results. The error bars are only statistical.

Intensity distributions

The partial wave intensities are shown in Fig. 90. The bottom left plot shows the sum of all foreground waves. Two peaks are clearly seen around 1720 MeV/c^2 and 1880 MeV/c^2, respectively. A peak is clearly seen around 1640 MeV/c^2 in the $J^P = 2^-$ intensities in both $K^+\bar{K}^{*0}$ and $f_2(1270)\pi^+$ waves. This is probably the production of the $\pi_2(1670)$ which is known to decay to both the $K\bar{K}^*$ and the $f_2(1270)\pi$. However, the $J^P = 2^-$ $K^+\bar{K}^{*0}$ intensity also shows enhancement around 1880 MeV/c^2. Evidence of a higher mass 2^- state has been reported by several experiments [95, 100, 101, 102, 103]. It is important to note that, experimentally, the $\pi_2(1670)$ couples most strongly to $f_2(1275)\pi$ ($\approx$ 56%), with weaker couplings to $K^*K(\approx$ 4.2%). Since the $f_2(1275)$ has a branching ratio of about 5% decaying into $K\bar{K}$, the two channels of $\pi_2(1670)$ decaying into $K^+K^-\pi^+$ via $K^+\bar{K}^{*0}$ and $f_2(1275)\pi^+$ should be comparable ($\approx 3:2$). This is consistent with what was seen in the 1700 MeV/c^2 region in the 2^- intensities. On the other hand, the other possible 2^{-+} state, the $\pi_2(1800)$, is predicted to have a farily large branching ratio decaying into $K^+K^-\pi^+$ via $K^*K(\approx$ 13% as opposed to only 1% via $f_2(1275)\pi$ decaying into $K^+K^-\pi^+$ [108]. Table 8 lists the partial widths of the $1D$ excitation and hybrid $\pi_2(1800)$ states using the $^3P_0$ model [104, 105, 106, 107]. If the 2^- intensity enhancement around 1880 MeV/c^2 is identified with the $\pi_2(1800)$ state, it is most likely a radial excitation of the $\pi_2(1670)$, even though the mass is relatiely low, instead of a hybrid meson.

The other strong foreground wave is the $J^P = 1^+$ wave around 1700 MeV/c^2. This could be identified with the $1^+1^{++}a_1(1640)$ which still needs confirmation. Reference

Table 8: Partial widths of 1D and hybrid $\pi_2(1800)$ states from Reference [108].

	$\rho\pi$	$\omega\rho$	$\rho_R\pi$	$b_1\pi$	$f_0\pi$	$f_1\pi$	$f_2\pi$	$K^*\bar{K}$	total
$\pi_{2(1D)}(1800)$	162	69	0	0	1	5	86	49	372
$\pi_{2(H)}(1800)$	8	0	5	15	1	0	50	1	80

[100] did not see any resonant activity in the partial wave analysis of $K^+K^-\pi^+$ system produced by a pion beam, although some enhancement was seen around 1700 MeV/c^2 in the 1^+ wave intensity. However, it is important to note that they only used 1^+P and S wave in their analysis. The VES collaboration reported a possible 1^{++} state at the same mass region in the $\pi^-\pi^-\pi^+$ partial wave analysis [109]. In the same experiment this thesis is based on, a possible 1^{++} was also observed around the same mass region [110]. For $M = 0$ partial waves, only one reflectvity exists.

The spin projection along the beam axis, M, is limited by $M < 3$, assuming that in peripheral meson photo-production the helicity change at the baryon vertex does not lead to $M > 2$ for the meson resonances.

The $J^P = 0^- K^+\bar{K}^{*0}$ intensity distribution does not have a lot of strength. Reference [109] also did not observe the decay of $\pi(1800)$ into $K^+\bar{K}^{*0}$. It is interesting to point out that the possible hybrid state $\pi(1800)$ was predicted to have a lower branching ratio decaying into $K^+\bar{K}^{*0}$ than the $q\bar{q}$ $\pi(1800)$. The $0^-K^+\bar{K}^{*0}(1430)$, on the other hand, shows some complicated behavior around 1960 MeV/c^2. It is not clear whether this is a fluctuation or evidence of a resonance. A $J^{PC} = 0^{-+}$ state was identified with the $\pi(1800)$ decaying into $K^-\bar{K}^*(1430)$ by the VES collaboration in the reaction $\pi^-A \to K^+K^-\pi^-A$ [111], but the mass was lower (at 1790 MeV/c^2)

There is no clear evidence of the production of $\rho(1700)$ in the $J^P + 1^-$ wave.

However, the $J^P = 1^- K^+ \bar{K}^{*0}$ intensity shows enhancement around 1900 MeV/c^2. A vector partner of the $\pi(1800)$ is expected at 1900 MeV/c^2 [108]. However, no candidates of such a state are present. Reference [108] predicts a 5% branching ratio of the decay of $J^{PC} = 1^{--}$ $\rho(1900)$ into $K\bar{K}^*$. Due to the low statistics, it is not possible to make any definite statement on the nature of the $J^P = 1^-$ partial wave.

Using PWA results for background estimate

Once a set of meson partial waves that describes the data is obtained, it can be used to check whether kinematic cuts used for the Θ^+ analysis can produce a peak in the nK^+ invariant mass spectrum, as seen in the previous chapter. Note that the additional cuts needed for the PWA on $t'(\gamma \to K^+K^-\pi^+) < 0.6$ (GeV/c^2)^2 and $\theta_{\pi^+}^{Lab} < 30^o$ leaves us only one third of the total events that are used for the Θ^+ search. The same kinematic cuts, such as those cuts used for the K^+ and π^+ center-of-mass angles are applied in the nK^+ and nK^+K^- invariant mass spectra. As shown in Fig. 91, those cuts should not generate a sharp peak in either spectrum. Furthermore, by varying the K^+ angle cut or replacing the π^+ angle cut with a cut on momentum transferred from the beam to the π^+ (Fig. 92), it is clear that the predicted nK^+ invariant mass distribution agrees with the data very well except in the region where the possible Θ^+ signal is observed.

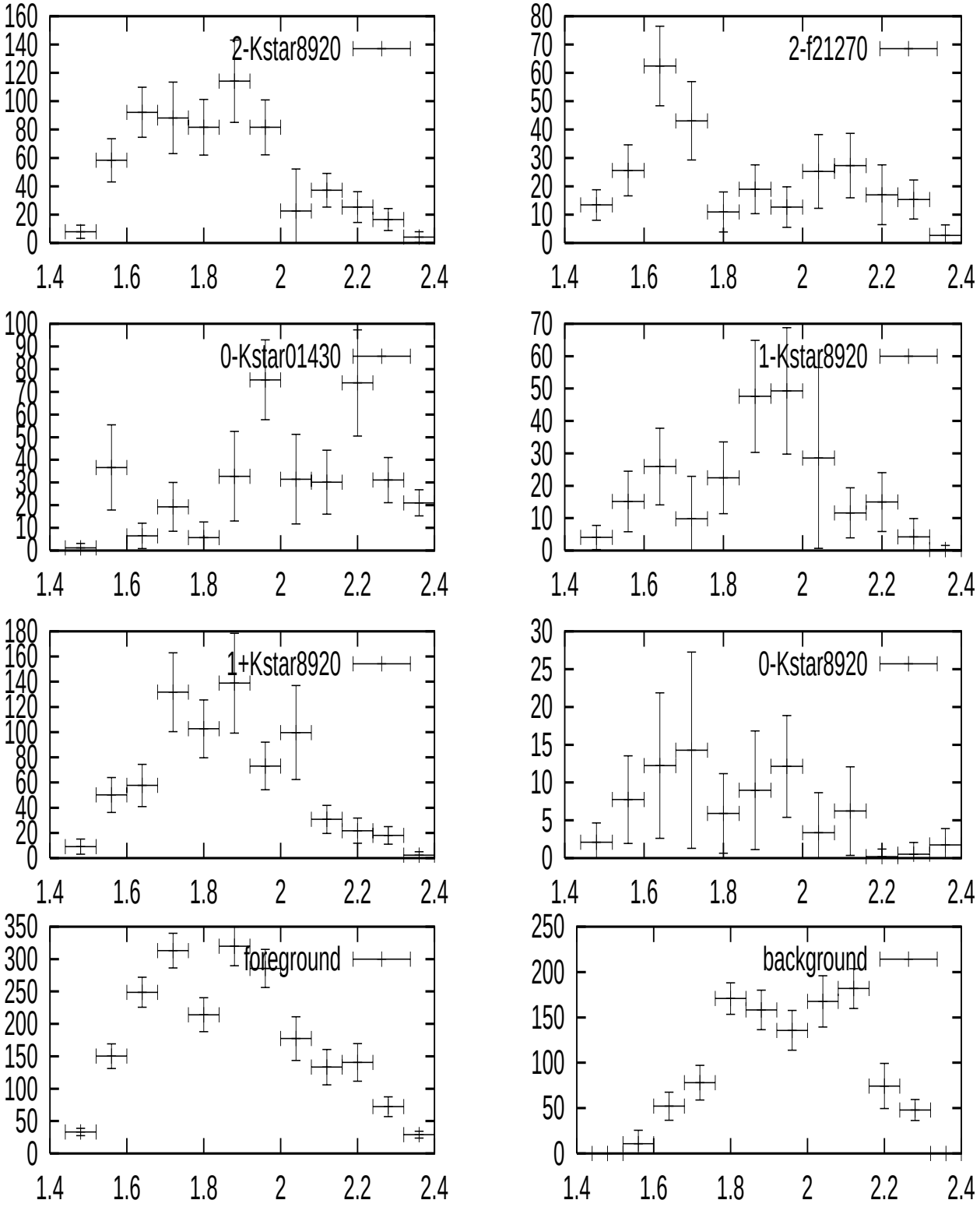

Figure 90: PWA results intensity distribution: Left panels from top to bottom:$2^-\bar{K}^{*0}$, $0^-K^{*0}(1430)$, $1^+\bar{K}^{*0}$ and total intensities. Right panel from top to bottom: $2^-f_2(1270)$, $1^-\bar{K}^{*0}$, $0^-\bar{K}^{*0}$ and isotropic background.

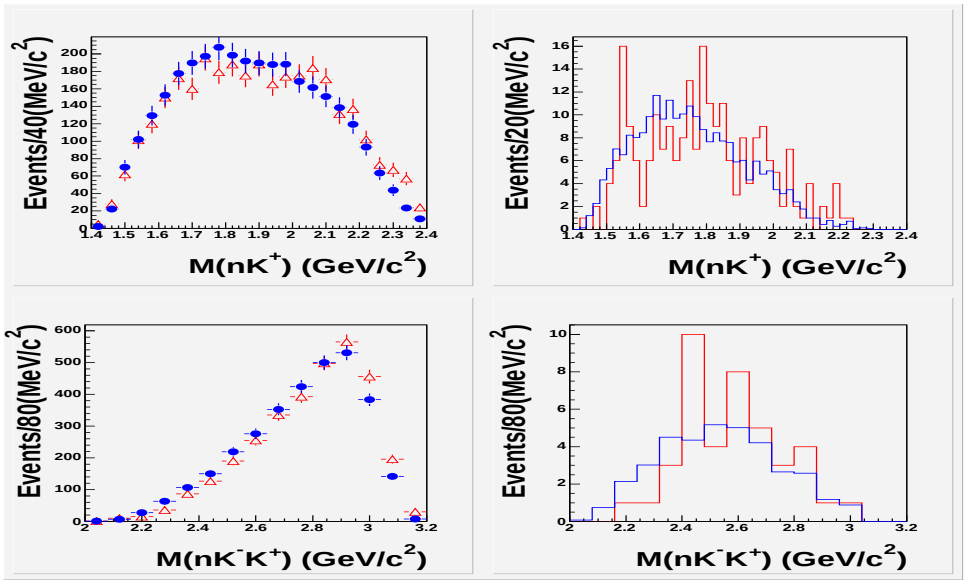

Figure 91: PWA predictions of the invariant mass spectra of nK^+ and nK^+K^- Left panels are invariant mass spectra for all events used for PWA, right panels are events with the angular cuts of with $cos(\theta^*_{\pi^+}) > 0.8$ and $cos(\theta^*_{K^+}) < 0.6$; Red histogram is the real data, while blue histogram is the prediction of the PWA results. The prediction is normalized to the data outside the Θ^+ region ($1.52 < M(nK^+) < 1.6$ GeV/c^2 for the nK^+ invariant mass spectrum, and it is normalized to the data outside the Δ^*/N^* region ($2.4 < M(nK^+K^-) < 2.56$ GeV/c^2 for the nK^+K^- invariant mass spectrum.

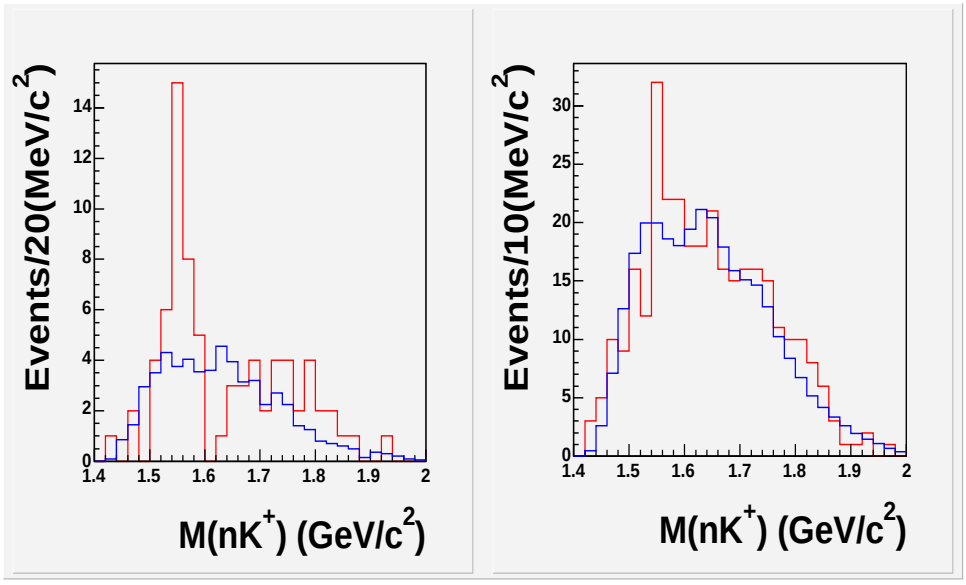

Figure 92: PWA prediction of the invariant mass spectra compared with data. Left: with the angular cuts of with $cos(\theta^*_{\pi^+}) > 0.8$ and $cos(\theta^*_{K^+}) < 0$. Right: with angular cut of $cos(\theta^*_{K^+}) < 0$ and $t'(\gamma \to \pi^+ < 1$ GeV/c^2. Red histogram is the real data, while blue histogram is the prediction of the PWA results. The prediction is normalized to the data outside the Θ^+ region ($1.52 < M(nK^+) < 1.6$ GeV/c^2.

CHAPTER VI

CONCLUSION AND DISCUSSION

In summary, the reaction $\gamma p \to \pi^+ K^- K^+ n$ has been analyzed to search for the Θ^+ particle. The tagged photon beam has an energy range of 3.0-5.47 GeV. A narrow $S = +1$ baryon signal was observed with a mass of $1555 \pm 7(\text{stat}) \pm 10(\text{sys})$ MeV/c^2 and a narrow width consistent with the CLAS resolution (FWHM=26 MeV/c^2). The statistical significance of the peak is 7.8 ± 1.0 σ. The state is consistent with the Θ^+ predicted by a chiral soliton model [42] for a 5-quark baryon state. Its mass and width is consistent within experimental resolution with a previous observation of the Θ^+ by the CLAS collaboration [51].

In addition, a partial wave analysis on the three body ($K^+ K^- \pi^+$) meson background has also been performed. The result shows that meson reflection is unlikely to contribute significantly to the Θ^+ signal that was observed. The $\pi_2(1670)$ was observed decaying into $K^+ K^- \pi^+$ in both the $K^+ \bar{K}^{*0}$ and $f_2(1275)\pi^+$ modes. There is an indication of a higher mass $J^P = 2^-$ state decaying into $K^+ \bar{K}^{*0}$ at 1880 MeV/c^2. There is also an enhancement in the $J^P = 1^+$ intensity distribution around 1700 MeV/c^2, which agrees with previous experiments and the analysis of three-π neutral channel in this experiment. However, due to the low statistics, it is not possible to further determine the resonant nature of these partial waves via phase motion.

The data seems to suggest the possible production of Θ^+ through an intermediate

heavy nucleon. Such a mechanism has recently received corroborative evidence from the NA49 analysis of $\Theta^+ \to pK^0_S$ in $p-p$ collisions [113]. If confirmed, this could have significant implication for the isospin of the pentaquark state Θ^+ or its excited partner.

Our analysis seems to confirm the existence of the $S = +1$ baryon state consistent with the theoretical predictions as well as the other experimental results. However, most of these results, including this thesis, suffer from limited statistics. Although the probability of statistical fluctuations creating a signal is low, it cannot be totally ruled out. The BES Collaboration also did not observe the Θ^+ in the reactions $\Psi(2S) \to \Theta\bar{\Theta} \to K^0_S p K^- \bar{n} + K^0_S n K^+ \bar{p}$ and $J/\Psi \to \Theta\bar{\Theta} \to K^0_S p K^- \bar{n} + K^0_S n K^+ \bar{p}$, which seems to suggest that if the Θ^+ does exist, there is much to learn about the dynamics of the production mechanisms.

Table 9: Existing evidence for $S = +1$ exotic baryons

Experiment	reaction	mass (MeV/c^2)	width (MeV/c^2)	Statistical significance
Spring8	$\gamma n \to K^+K^-n$	1540± 10	<25	4.6 σ
CLAS	$\gamma n \to K^+K^-n$	1542± 2± 5	21	5.2±0.6 σ
DIANA	$K^+Xe \to \Theta^+Xe'$	1539± 2	<9	4.4 σ
CLAS	$\gamma p \to K^+K^-\pi^+n$	1555± 7± 10	<26	7.8± 1.0 σ
SAPHIR	$\gamma p \to K^+K^0_s n$	1540± 4± 2	<25	4.8 σ
HERMES	$\gamma d \to pK^-K^0_s n$	1528±2.6±2.1	19±5±2	4-6 σ
SVD	$pA \to pK^0_s X$	1526± 3± 3	<24	5.6 σ
COSY	$pp \to \Sigma^+ pK^0$	1530± 5	<18±4	4-6 σ

Furthermore, although there have been multiple reports on the observation of a possible $S = +1$ baryon state, the masses are nevertheless scattered in a range of

30 MeV/c^2. This is quite significant considering the predicted narrow width (see Table 9). Are we seeing the same state? One possible scenario is that there are actually two $S = +1$ baryon states, with the low mass state being the ground state of the Θ^+ ($J = 1/2$) and the high mass state being the $J = 3/2$ Θ^* excited partner. Dudek and Close argue for this scenario [114]. The second scenario is the possibility of a cluster of pentaquark states with isospin $I = 0, 1, 2$ lying close to each other (1.55 ± 0.15 GeV/c^2) as QCD sum rules calculations by S. Zhu suggest [115], although there is an apparent lack of evidence for a Θ^{++} [112, 108].

As Close recently pointed out at Hadron2003 [116], the eventual establishment of the $S = +1$ exotic baryon state could lead to a fundamental change to the constituent quark model. However, the jury is still out, and future large statistics experiment will most likely cast the final vote [61].

APPENDIX A

THE ANALYSIS OF $K^+K^-\pi^+$ SYSTEM

Background

S.U.Chung has given a complete description of the analysis of non-strange X^0 and X^+ which decay into the final state $K\bar{K}\pi$ [117]. Based on his note, I came up with the following note dealing with an X^+ that would decay into a $(K\bar{K}\pi)^+$ final state for experiment $E01\_017$ at JLab, also the CLAS collaboration.

Consider the production of a non-strange meson state X in the reaction

$$\gamma p \to X^+ n \tag{44}$$

which then decays into

$$X^+ \to (K\bar{K}\pi)^+ \tag{45}$$

In the following note, we examine the complete list of all possible decay modes and work out I, C and G-parities for each distinct final state.

It is important to review the properties of K's and π's under charge conjugation and G parity. For π's, we have

$$\mathbf{C}\begin{pmatrix}\pi^+\\ \pi^0\\ \pi^-\end{pmatrix} = \begin{pmatrix}-\pi^-\\ +\pi^0\\ -\pi^+\end{pmatrix}, \mathbf{G}\begin{pmatrix}\pi^+\\ \pi^0\\ \pi^-\end{pmatrix} = \begin{pmatrix}-\pi^-\\ -\pi^0\\ -\pi^+\end{pmatrix}$$

For K's, we have

$$\mathbf{C}\begin{pmatrix}K^+\\ K^0\end{pmatrix} = \begin{pmatrix}+K^-\\ -\bar{K}^0\end{pmatrix}, \mathbf{G}\begin{pmatrix}K^+\\ K^0\end{pmatrix} = \begin{pmatrix}-\bar{K}^0\\ -K^-\end{pmatrix}$$

and

$$\mathbf{C}\begin{pmatrix} \bar{K}^0 \\ K^- \end{pmatrix} = \begin{pmatrix} -K^0 \\ +K^+ \end{pmatrix}, \mathbf{G}\begin{pmatrix} \bar{K}^0 \\ K^- \end{pmatrix} = \begin{pmatrix} +K^+ \\ +K^0 \end{pmatrix}$$

We assume that the state X^+ produced in the reactoin $\gamma p \to X^+ n$ is in an eigenstate of $I^G J^{PC}$, which should be shared by the final state $K\bar{K}\pi$ if they are conserved in the decay.

$\underline{X^+ \text{ decays via } \bar{K}^{*0}}$

A $\bar{K}^{*0}$ decays into a $K\pi$ system. For $\bar{K}^{*0}$'s with S (strangeness) $= 1$, expanding them in isospin space, we have

$$\begin{aligned} K^{*+} &= \sqrt{\frac{2}{3}}\pi^+ K^0 - \sqrt{\frac{1}{3}}\pi^0 K^+ \\ K^{*0} &= \sqrt{\frac{1}{3}}\pi^0 K^0 - \sqrt{\frac{2}{3}}\pi^- K^+ \end{aligned} \tag{46}$$

For S=-1, we have

$$\begin{aligned} K^{*-} &= \sqrt{\frac{1}{3}}\pi^0 K^- - \sqrt{\frac{2}{3}}\pi^- \bar{K}^0 \\ \bar{K}^{*0} &= \sqrt{\frac{2}{3}}\pi^+ K^- - \sqrt{\frac{1}{3}}\pi^0 \bar{K}^0 \end{aligned} \tag{47}$$

Using the properties of K's and π's in the previous section, we can easily derive:

$$\mathbf{C}\begin{pmatrix} K^{*+} \\ K^{*0} \end{pmatrix} = \begin{pmatrix} -K^{*-} \\ +\bar{K}^{*0} \end{pmatrix}, \mathbf{G}\begin{pmatrix} K^{*+} \\ K^{*0} \end{pmatrix} = \begin{pmatrix} \bar{K}^{*0} \\ K^{*-} \end{pmatrix}$$

and

$$\mathbf{C}\begin{pmatrix} \bar{K}^{*0} \\ K^{*-} \end{pmatrix} = \begin{pmatrix} +K^{*0} \\ -K^{*+} \end{pmatrix}, \mathbf{G}\begin{pmatrix} \bar{K}^{*0} \\ K^{*-} \end{pmatrix} = \begin{pmatrix} +K^{*+} \\ -K^{*0} \end{pmatrix}$$

We can easily construct an G-Parity eigenstate of $(K\bar{K}^*)^+$ as follows:

$$\begin{aligned} A(g) &= \sqrt{\frac{1}{2}}(\bar{K}^{*0}K^+) + gK^{*+}\bar{K}^0) \\ &= \sqrt{\frac{1}{6}}[-(\pi^0\bar{K}^0)K^+) - g(\pi^0K^+\bar{K}^0)] + \sqrt{\frac{1}{3}}[(\pi^+K^-)K^+) + g(\pi^+K^0\bar{K}^0)] \end{aligned} \tag{49}$$

It's easy to demonstrate that

$$GA(g) = gA(g) \tag{50}$$

where $g = \pm 1$ is the G-parity eigenvalue of the $(K\bar{K}^*)^+$ state.

At this point, it is important to note that $\bar{K}^{*0}K^+$ is not a G-parity eigenstate. To determine the I^GJ^{PC} quantum numbers for X^+ which decays to $K^+K^-\pi^+$, it is not enough to just look at the $\bar{K}^{*0}K^+$ channel. This is different from a neutral $K^+K^-\pi^+$ system, which can be constructed as a C-parity and G-parity eigenstate depending on the orbital momentum between the two K's being even or odd. For details, see Reference [117].

Complete Decay Amplitudes for X^+

To determine the complete decay amplitude for the state X^+, we shall include the decay via isobars such as a's and f's. Here a's refer to $a_0(980)$,$a_2(1320)$, and other $I^G = 1^-$ objects, and f's include $f_0(980)$,$f_2(1270)$, and other $I^G = 0^+$ states. Assuming $I = 1$ and noting $G(\pi^+) = -1$ for the state X^+ which decays to $K^+K^-\pi^+$, the complete amplitude for $G = +1$ can be written as:

$$A^+ = c^+ A^+(\bar{K}^{*0}) + d^+ A(a) \tag{51}$$

where A stands for amplitude, $+$ stands for positive G-parity of the X^+ state, and the particle inside the parenthesis refers to the intermediate decay isobar.

For $G = -1$, this can be written as

$$A^- = c^- A^-(\bar{K}^{*0}) + d^- A(f) \tag{52}$$

We will first work out A^+, and A^- will be similar.

$$A(a) = \sqrt{\frac{1}{2}}[\pi^0 a^+ - \pi^+ a^0] \tag{53}$$

and a's have the expansion

$$\begin{aligned} a^0 &= \frac{1}{2}[K^+K^- + K^0\bar{K}^0 + \bar{K}^0K^0 + K^-K^+] \\ a^- &= \sqrt{\frac{1}{2}}[K^0K^- + K^-K^0] \\ a^+ &= \sqrt{\frac{1}{2}}[K^+\bar{K}^0 + \bar{K}^0K^+] \end{aligned} \tag{54}$$

One then easily finds

$$\begin{aligned} A(a) = &\frac{1}{2}[\pi^0(K^+\bar{K}^0)_a + \pi^0(\bar{K}^0K^+)_a] \\ &-\frac{1}{2\sqrt{2}}[\pi^+(K^+K^-)_a + \pi^+(K^0\bar{K}^0)_a + \pi^+(\bar{K}^0K^0)_a + \pi^+(K^-K^+)_a] \end{aligned} \tag{56}$$

It's easy to verify that $GA(a) = +A(a)$ for a decay of $X^- \to \pi + a$.

Similarly, f's has the expansion

$$f^0 = \frac{1}{2}[K^+K^- - K^0\bar{K}^0 - \bar{K}^0K^0 + K^-K^+] \tag{57}$$

Again, using the properties of K under the G-parity operation described in the first section of this appendix, we can demonstrate that $Gf = +f$.

Now we have the amplitude for $X^- \to \pi^+ + f$:

$$A(f) = \frac{1}{2}[\pi^+(K^+K^-)_f - \pi^+(K^0\bar{K}^0)_f - \pi^+(\bar{K}^0K^0)_f + \pi^+(K^-K^+)_f] \tag{58}$$

and $GA(f) = -A(f)$.

We can now derive the complete decay amplitude for all decay modes of $X^+ \to (K\bar{K}\pi)^+$. For the final state $K^+K^-\pi^+$, we have

$$\begin{aligned} A(K^+K^-\pi^+) = \sqrt{\frac{1}{3}}c^+[(\pi^+K^-)^*K^+]^+ + c^-[(\pi^+K^-)^*K^+]^- \\ -(\frac{1}{2\sqrt{2}})d^+[\pi^+(K^+K^-)_a + \pi^+(K^-K^+)_a] \\ +(\frac{1}{2})d^-[\pi^+(K^+K^-)_f + \pi^+(K^-K^+)_f] \end{aligned} \tag{59}$$

In Table A some of the possible decay modes for $X^+ \to (K\bar{K}\pi)^+$ are listed.

It is essential to point out that the final state $(\pi^+K^-)^*K^+$ is not an eigenstate of G-parity. However, the components from X^+ decay via a's and f's which possess different G-parity eigenvalues will enable one to determine the G-parity of the $(\pi^+K^-K^+)$ system.

Table 10: Predicted Decay Modes for $X^+ \to (K\bar{K}\pi)^+$

I^G	J^{PC}	X^+	**Decay Mode**	**L of decay**
1^+	1^{--}	$\rho(1700)$	$\bar{K}^{*0}(892)K$	1
1^-	1^{++}	$a_1(1700)$	$\bar{K}^{*0}(892)K$	1
1^-	2^{-+}	$\pi(1670)$	$\bar{K}^{*0}(892)K$	1
1^-	2^{-+}	$\pi(1670)$	$f_2(1270)\pi$	2
1^-	0^{-+}	$\pi(1800)$	$\bar{K}^{*0}(892)K$	1
1^-	0^{-+}	$\pi(1800)$	$f_0(980)\pi$	0
1^-	0^{-+}	$\pi(1800)$	$\bar{K}^{*0}(1430)K$	0
1^-	2^{-+}	$\pi_2(1800)$	$\bar{K}^{*0}(892)K$	0
1^+	3^{--}	$\rho(1690)$	$a_2(1320)\pi$	2

APPENDIX B

THE REFLECTIVITY BASIS

It is a common practice to use the spin density matrix ρ in studying resonance production with the rest frames of the resonance chosen by Gottfried-Jackson (GJ) convention. In the reaction of $\gamma p \to Rn$, the reflection operator Π_y is related to parity by a rotation through π about the y axis:

$$\Pi_y = Pe^{-i\pi J_y} \tag{60}$$

Knowing that the helicity states satisfy Eq. 63, which is independent of the chosen reference frame so long as $\vec{p}$ is in the $x-z$ plane, it is easy to obtain $\Pi_y^2 = (-)^{2J}$,

$$\Pi_y|\vec{p}, a, \lambda\rangle = \eta(-)^{J-\lambda}|\vec{p}, a, -\lambda\rangle \tag{61}$$

where a is J^η, and $J(\eta)$ is the spin (parity) of the state. For the state R in its rest frame (GJ), the eigenstates of Π_y are given by

$$|\epsilon, a, m\rangle = [|am\rangle + \epsilon\eta(-)^{J-m}|a-m\rangle]\theta(m) \tag{62}$$

with $\theta(m)$ defined as

$$\theta(m) = \begin{cases} \frac{1}{\sqrt{2}} & m > 0 \\ \frac{1}{2} & m = 0 \\ 0 & m < 0 \end{cases}$$

It is easy to verify that

$$\Pi_y|\epsilon, a, m\rangle = \epsilon(-)^{2J}|\epsilon, a, m\rangle \tag{63}$$

$\Pi_y^2 = (-)^{2J}$ requires that $\epsilon^2 = (-)^{2J}$ and orthogonality of the eigenstate defined by Eq. 62 requires that $\epsilon\epsilon^* = 1$, so

$$\epsilon = \begin{cases} \pm 1 \text{ for bosons} \\ \\ \pm i \text{ for fermions} \end{cases}$$

Notice that for bosons there is only one reflectivity eigenstate for $m = 0$, with the eigenvalue of reflectivity being $\epsilon = \eta(-)^J$.

The spin density matrix, denoted by ${}^{\epsilon}\rho$, is diagonal in reflectivity if parity is conserved [94]. Specifically, in the language of partial wave analysis, the production amplitude can be written as

$${}^{\epsilon}V_{am}^{k} = \langle \epsilon a m, \vec{p_n}\lambda_n | T^J | \vec{p_\gamma}\lambda_\gamma, \vec{p_p}\lambda_p \rangle \tag{64}$$

where k denotes $\lambda_{\gamma,\lambda_p,\lambda_n}$ as the helicities. Using Eq.63 and noting that T^J is reflection invariant in strong interactions, i.e., $T^J = \Pi_y^{-1} T^J \Pi_y$, we can obtain

$${}^{\epsilon}V_{am}^{-k} = \epsilon^* \eta_\gamma \eta_p \eta_n (-)^{J_\gamma - \lambda_\gamma + J_p - \lambda_p + J_n - \lambda_n} \epsilon V_{am}^{k} \tag{65}$$

which can easily be reduced by using $\epsilon\epsilon^* = 1$ to

$${}^{\epsilon}V_{am}^{-k} = -\epsilon(-)^{\lambda_\gamma + \lambda_p + \lambda_n} V_{am}^{k} \tag{66}$$

The spin density matrix ${}^{\epsilon}\rho$ now can be written as

$${}^{\epsilon}\rho = \begin{pmatrix} {}^{+}\rho & 0 \\ \\ 0 & {}^{-}\rho \end{pmatrix}$$

It is important to remember that states of different reflectivities do not interfere with each other.

REFERENCES

[1] V. E. Barnes *et al.*, *Phys. Rev. Lett.* **12**,204 (1964);

[2] V. E. Barnes *et al.*, *Phys. Lett.* **12**,134 (1964);

[3] G. S. Abrams *et al.*, *Phys. Rev. Lett.* **13**, 670 (1964);

[4] Murray Gell-Mann, *Phys.Rev.***125** 1067 (1962);

[5] Murray Gell-Mann, *Phys.Lett.***8** 214 (1964);

[6] W. D. Walker *Phys.Rev.***98** 1407 (1955);

[7] J. D. Sorrels, R. B. Leighton and C. C. Anderson *Phys.Rev.***100** 1457 (1955);

[8] Murray Gell-Mann, *Nuovo Cim. Suppl.***4** 848 (1956);

[9] G. ZWEIG, CERN-8182-TH-401 (1964);

[10] G. ZWEIG, CERN-8419-TH-412 (1964);

[11] H. L. Anderson, E. Fermi, E. A. Long and D. E. Nagle, *Phys.Rev.* **85** 936,1952;

[12] M. Y. Han and Yoichiro Nambu *Phys.Rev.* **B139** 1006,1965;

[13] O. W. Greenberg and D. Zwanziger*Phys. Rev.* **150** 1177, (1966);

[14] D. J. Gross and F. Wilczek, *Phys. Rev.* **D8**, 3633 (1973);

[15] J. J. Aubert *et al.*, *Phys. Rev. Lett.* **33** 1404(1974);

[16] J. E. Augustin *et al.*, *Phys. Rev. Lett.* **33** 1406, (1974);

[17] S.W. Herb *et al.*, *Phys. Rev. Lett.* **39** 252, (1977);

[18] F. Abe *et al.*, *Phys. Rev. Lett.* **74** 2626, (1995);

[19] S. Abachi *et al.*, *Phys. Rev. Lett.* **74** 2632, (1995);

[20] T. Barnes *Exotic Mesons, Theory and Experiment*, arxiv:hep-ph/0007269, v1 (2000);

[21] C. Bernard *et al.*, *Phys. Rev.* **D56**, 7039 (1997);

[22] M. Chanowitz and S. Sharpe, *Nucl. Phys.* **B222**, 211 (1983);

[23] A. Chodos *et al.*, *Phys. Rev.* **D9**, 3471 (1974);

[24] S. Chung,*Spin Formalisms*, CERN Report (1971);

[25] F. Viron, *Phys. Rev. Lett.* **53**,2207 (1983);

[26] S. Zhu, *The Masses and Decay Widths of the Heavy Hybrid Mesons*, arxiv:hep-ph/9812405, v3 (1999)

[27] S. Zhu, *Phys. Rev.* **D60** , 097502 (1999)

[28] G. S. Bali *et al.*, *Phys. Rev.* **D56**, 2566 (1997)

[29] N. Isgur, R. Kokoski, and J. Paton,*Phys. Rev. Lett.* **54**,869 (1984);

[30] P. Lacock *et al.*, UKQCD COllaboration,*Phys. Lett.***B401**, 308 (1997);

[31] T. Barnes *et al.*, *Phys. Rev.* **D52**, 5242 (1995);

[32] G. S. Bali *et al.*, *Phys. Rev.* **D62**, 054503 (2000);

[33] D. R. Thompson *et al.*, BNL852 Collaboration,*Phys. Rev. Lett.* **79**, 1630 (1997);

[34] G. M. Beladidze *et al.*, *Phys. Lett.* **B314**, 276 (1993);

[35] A. Abele *et al.*, Crystal Barrel COllaboration, *Phys. Lett.*, **B423**, 175 (1998);

[36] G.S.Adams *et al.*, BNL852 Collaboration, *Phys. Rev. Lett.*, **81**, 5760 (1997);

[37] E. Ivanov *et al.*, *Phys. Lett.*, **86**, 3977 (2001);

[38] Y. Khokhlov, *Nucl. Phys.* **A663**, 596 (2000);

[39] H. J. Lipkin, *Phys.Lett.* **B219**, 99,(1989);

[40] D. Strottman, *Phys. Rev.* **D20**, 748 (1979);

[41] M. Jezabeck and M. Praszalowicz, *World Scientific* 112 (1987);

[42] D. Diakonov, V. Petrov, and M. Polyakov, *Z. Phys.* **A359** 305 (1997);

[43] T. H. Skyrme, *Proc. Soc. Lond.* **A260**, 1975 (1961);

[44] T. H. Skyrme, *Nucl. Phys.* **31**, 556 (1962);

[45] E. Witten, *Nucl. Phys.* **B223**, 433 (1983);

[46] E. Witten, *Nucl. Phys.* **B223**, 422 (1983);

[47] E. Guadagnini, *Nucl. Phys.* **B236**, 35 (1984);

[48] D. Diakonov, V. Petrov *Baryons as solitons*, preprint LNPI-967(1984), published in: *Elementary particles*, Moscow, Energoatomizdat vol.2, p.50(in Russian), (1985) ;

[49] R. L. Jaffe and F. Wilczek, *Phys. Rev. Lett.* **91**, 232003 (2003);

[50] T. Nakano *et al.*, *Phys. Rev. Lett.* **91**, 012002 (2003);

[51] S. Stepanyan *et al.*, *Phys. Rev. Lett.* **91**, 252001 (2003);

[52] V. Kubarovsky and S. Stepanyan, talk presented at the Conference on the Intersections of Particle and Nuclear Physics (CIPANP2003), New York, NY, USA, May 19-24, arXiv:hep-ex/0307088, (2003);

[53] J. Barth *et al.*, *Phys. Lett.* **B572**, 127 (2003);

[54] V. Barmin *et al.* , *Phys. Atom. Nucl.* **66**, 1715 (2003);

[55] A. E. Asratyan, A. G. Dolgolenko and M. A. Kubantsev, arXiv:hep-ex/0309042 (2003);

[56] A. Airapetian *et al.*, arXiv:hep-ex/0312044 (2003);

[57] A. Aleev *et al.*, arXiv:hep-ex/0401024 (2004);

[58] M. Abdel-Bary *et al.*, arXiv:hep-ex/0403011 (2004);

[59] C. Alt *et al.*, NA49 Collaboration, arXiv:hep-ex/0310014 (2003);

[60] H.G.Fischer, S. Wenig, arXiv:hep-ex/0401014 (2003);

[61] Jefferson Lab PAC25 (2004);

[62] A. Berthon *et al.*, *Nulcear Physics* **B63**, 54(1973);

[63] W. Liu, C. M. Ko, *Phys. Review* **C68**, 045203 (2003);

[64] W. Liu, C. M. Ko, and V. Kubarovsky, arXiv:nucl-th/0310087 (2003);

[65] S. Janssen, J. Ryckebusch, D. Debruyne, and T. Van Cauteren *Phys. Rev.* **C65** 015201 (2002);

[66] W. Liu, C. M. Ko, arXiv:nucl-th/0309023 (2003);

[67] S. Capstick, P. R. Page and W. Roberts,*Phys. Lett.* **B570**, 185 (2003);

[68] Y. Oh, H. Kim and S. H. Lee,arXiv:hep-ph/0310019 (2003);

[69] M. V. Polyakov and A. Rathke,arXiv:hep-ph/0303138 (2003);

[70] P. R. Page, arXiv:hep-ph/0310200 (2003);

[71] B. M. Dunham, Jeffrson Lab, A status Report, JLAB-ACC 96-01, Jefferson Laboratory, 12000 Jefferson Avenue, Newport News, VA 23606 (1996);

[72] J. Dobaczewski, H. Flocard and J. Treiner,*Nucl. Phys.* **A422**, 103 (1984);

[73] B.A. Mecking *et al.*, *Nucl. Instrum. Methods* **A503**, 513 (2003);

[74] D. S. Carman *et al.*, *The Region One Drift Chamber for the CLAS Spectrometer*, *Nucl. Instrum. Methods* **A419**, 315 (1998);

[75] M. D. Mestayer *et al.*, *Construction update and drift velocity calibration for the CLAS drift chamber system Nucl. Instrum. Methods* **A367**, 316 (1995);

[76] M. D. Mestayer *et al.*, CLAS drift chamber system *Nucl. Instrum. Methods* **A449**, 81 (2000);

[77] L. M. Qin *et al.*, *Prototype studies and design consideration for the CLAS Region 2 drift chambers Nucl. Instrum. Methods* **A411**, 265 (1998);

[78] G. Adams *et al.*, *Nucl. Instrum. Methods* **A465**, 414 (2001);

[79] E. S. Smith *et al.*, *Nucl. Instrum. Methods* **A432**, 265 (1999);

[80] M. Amarian *et al.*, *Nucl. Instrum. Methods* **A460**, 239 (2001);

[81] D. Sober *et al.*, *Nucl. Instrum. Methods* **A440**, 263 (2000);

[82] S. Taylor *et al.*, *Nucl. Instrum. Methods* **A462**, 484(2001);

[83] C. W. Salgado*et al.*, *Photon Trigger, CLAS Internal Technical Note*, (2001);

[84] M. Battaglieri*et al.*, *First Level Trigger Optimisation in Vector Meson Photoproduction*, CLAS-NOTE 97-006 (1997);

[85] M. Battaglieri*et al.*, *Level One Trigger Monitor*, CLAS-NOTE 00-002 (2000);

[86] E. Anciant *et al.*, *Tagger HIt Reconstruction Software and Tagger Calibration Overview*, CLAS-NOTE 99-004; (1999);

[87] J. Li, *The New Tagger Calibration Program*, CLAS-NOTE 03-004, (2003);

[88] D. Lawrence and M. D. Mestayer, *CLAS Drift Chambers Calibrations: Software and Procedures.* CLAS-NOTE 99-018, (1999);

[89] E. S. Smith *et al.*, *Calibration of the CLAS TOF System, CLAS-NOxcTE 99-011*, (1999);

[90] J. P. Cummings and D. P. Weygand,*The New BNL Partial Wave Analysis Programs ,BNL Report* **BNL-64637**, (1997);

[91] J. P. Cummings and D. P. Weygand,*An Object-Oriented Approach to Partial Wave, submitted to BNL Report NIM A* , arXiv:hep-ph/0309052 v1, (2003);

[92] D. J. Herndon *et al.*, *Phys. Rev.* **D11**, 3165 (1975);

[93] S. Chung,*Formulas for partial-wave anlaysis*, BNL-note (1988);

[94] S. Chung, T. Trueman, *Positivity conditions on the spin density matrix: A simple parametrization*, *Phys. Rev.* **D11 (3)**, 633, (1975);

[95] C. Daum *et al.*, *Phys. Lett.* **B89** 285, (1980);

[96] M. E. Rose, *Elementary Theory of Angular Momentum.* John Wiley Sons, New York, (1957);

[97] F. Von Hippel and C. Quigg *Phys. Rev.* **D5**, 624, (1972);

[98] K. Hagiwara *et al.*, *Phys. Rev.* **D66** 010001, (2002);

[99] Martin L. Perl, *High Energy Hadron Physics* JOhn Wiley Sons, Inc. (1974);

[100] I. D. Leedom *et al.*, *Phys. Rev.* **D27** 1426, (1983);

[101] M. Lu, *Exotic mesons in the $\omega^+\pi^-\pi^0$ system produced in π^-p interations at 18 GeV/c* Ph.D. Thesis Dissertation, Rensselaer Polytechnic Institute(2003);

[102] D. Antreasyan *et al.*, *Z. Phys.* **C48** 561, (1990);

[103] H. J. Behrend *et al.*, *Z. Phys.* **C46** 583, (1990);

[104] G. Busetto and L. Oliver, *Z. Phys.* **C20** 247 (1983);

[105] R. Kokoski and N. Isgur,*Phys. Rev.* **D35** 907 (1987);

[106] P. Geiger and E. S. Swanson,*Phys. Rev.* **D50** 6855 (1994);

[107] H. G. Blundell and S. Godfrey,*Phys. Rev.* **D53** 3700 (1996);

[108] T. Barnes, F. E. CLose and P. R. Page, *Higher Quarkonia*, arXiv:hep-ph/9609339 (1996);

[109] D. V. Amelin *et al.*, *Phys. Lett.* **B356** 595, (1995);

[110] J. Li, *Search for exotic mesons in $\pi^+\pi^-\pi^0$ decay* Ph.D. Thesis Dissertation, Rensselaer Polytechnic Institute(2003);

[111] E. B. Berdnikov *et al.*, *Phys. Lett.* **B337** 219, (1994);

[112] V. Kubarovsky, L. Guo and D. Weygand *et al.*, *Phys. Rev. Lett.* **92**, 032001, (2004)

[113] D. Barna and F. Sikler, NA49 Note 294 (2003);

[114] J. Dudek and Franck Close, *The $J = \frac{3}{2}\Theta^*$ partner to the $\Theta(1540)$ baryon*, arXiv:hep-ph/0311258, v2, (2004);

[115] S. Zhu, *Understanding Pentaquark States in QCD*, arXiv:hep-ph/0307345, (2003);

[116] F. E. Close, *The End of the Constituent Quark Model?* Talk given at Hadron 03: 10th International Conference on Hadron Spectroscopy, Aschaffenburg, Germany, 31 Aug - 6 Sep 2003. arxiv:hep-ph/0311087, (2003)

[117] S. Chung, *Analysis of $K\bar{K}\pi$ systems, Version I* , BNL preprint, BNL-QGS-98-901(1998);